THEORY OF TOPOLOGICAL INSULATORS AND ITS APPLICATIONS

A Dissertation

Submitted to the Faculty

of

Purdue University

by

Parijat Sengupta

In Partial Fulfillment of the

Requirements for the Degree

of

Doctor of Philosophy

May 2014

Purdue University

West Lafayette, Indiana

ACKNOWLEDGMENTS

I would like to record my gratitude to my advisor, Prof. Gerhard Klimeck, for introducing me to a variety of topics in my PhD. I have benefited immeasurably from my experience in his group and the insights he provided for this work and continuous support of my PhD. He acquainted and advised me on the most current science topics that impact engineering inventions and instilled an awareness of computational techniques required to tackle real-world problems in the semiconductor industry. Personally, I will remain forever grateful to him. He nurtured and mentored me for over five years and scrupulously scrutinized everything (the many evenings spent over a figure in a presentation or wording of a manuscript bear testimony). Above all, by repeatedly challenging me, he inculcated academic honesty.

The Late Prof. Gabriele Guiliani taught me condensed matter physics through his classes. More importantly, he showed how to phrase and frame a physical scenario. I had trouble answering many of his questions but I truly learned to probe deeper in to the vast ocean of theoretical condensed matter physics. Thank you for having spent so much time with me outside of the class and entertaining my myriad questions, specially on spin-orbit coupling and its diverse manifestations in solids.

Prof. Erica Carlson was kind enough to patiently listen to my questions on condensed matter physics even in a graduate class which primarily focused on advanced electromagnetic theory. Through her answers she constantly demonstrated the underlying unity of physics. I also thank her for letting me walk in to her office without prior appointments and also being a part of my PhD committee.

I thank Prof. Mark Lundstrom for kindly agreeing to serve on my PhD committee. I gained a wealth of knowledge by attending his courses on advanced MOS transistors. His incredible insight about current MOS-devices and future trends have helped me shaped my work. Thank you!

Prof. Zhihong Chen gladly accepted to supervise my PhD work. My conversations with her have focused on the experimental aspects of topological insulators and graphene. Thank you for helping me along the way and your valuable suggestions on how to proceed with spin transport modeling in topological insulators.

I want to thank Prof. Tillmann Kubis who has spent countless hours advising, instructing and keeping me on track. He patiently taught me to do focused research, write more effective journal papers, and prepare compelling conference presentations. He has unhesitatingly shared with me his own PhD study materials and several journal/monograph contributions useful to my graduate work.

Semiconductor modeling work needs a lot of computer time, in this regard, I have been very adequately supported by Prof. Michael Povolotskyi and Dr.Jim Fonseca. Thank you for keeping up with my odd requests about code compilation and help remove the hurdles I confront on the numerical/computational aspect of my PhD.

A large number of people outside of Purdue have supported me. Prof. Taylor Hughes, a condensed matter theorist at the physics department of UIUC, spent several hours on Skype explaining me the intriguing field of topological insulators. I wouldn't have made much headway in to this completely new field of condensed matter physics without his assistance. I acknowledge his invaluable help and express my highest gratitude to him.

Prof. Xiaoliang Qi, professor in theoretical condensed matter physics at Stanford University, explained to me the origin of many newly predicted and experimentally observed phenomena in topological insulators including the topological field theory of time reversal invariant insulators.

Profs. Ewelina Hankiewicz and Laurens Molenkamp, condensed matter physicists at University of Würzburg, Germany, greatly aided my understanding of 2D and 3D topological insulators and the role of spin currents. Dr. Vasudha Shivamoggi from UIUC (now with Northrop Grumman) answered all my questions on Berry phase calculations and provided useful notes on topology and differential geometry.

I have been fortunate to be associated with wonderful peers in the Klimeck group. In particular, my fellow PhD student and friend Yaohua Tan, has supported me enormously. He has often been the person, I have sought out for a primary discussion on a difficult topic. I thank him for his collaboration and teaching me a lot of rigorous and sophisticated mathematics and physics.

For many interesting discussions about physics, current semiconductor device research and graduate work (including the ubiquitous stress), I must thank my very good friends Abhijeet Paul and Saumitra Mehrotra and later the Williamsburg group. We have spent many happy hours together and has made my life at West Lafayette more agreeable. Genuine gratitude also to Hannah Williams for the many dinners she prepared for me.

Sunhee Lee hand-taught me C/C++ programming in a real-world scientific environment, writing highly parallel code and numerous tips about memory management. My first collaborator Hoon Ryu during my early days at Purdue. I learnt much from him.

Zhengping Jiang, Daniel Meija, Daniel Lemus, and Yu He have helped me significantly with software, code compilation, and debugging/analyzing the large volume of data that I produce. Thank you for your friendship and patience with a difficult co-worker!

My life at Purdue has been considerably eased due to the great amount of administrative assistance I have received from Vicki Johnson, Amanda Buckles, Megan Rush, and Cheryl Haines. Thank you for caring for my flight and accommodation details as I travelled to conferences all across United States.

Finally, I started the doctoral program at Purdue university believing that I would learn things and facts hitherto unknown and incomprehensible to me. As I near the finish-line, in retrospect, the cherished part of my PhD days has not just been the learning. I indeed, learnt much, but more fulfilling has been the many unforeseen things I have experienced and shared with everyone who has contributed to my

overall well-being. This has been a journey very long and occasionally arduous but overwhelmingly rewarding!.

Thank you all.

TABLE OF CONTENTS

Page

Page

LIST OF TABLES

LIST OF FIGURES

Figure Page

Figure Page

ABBREVIATIONS

BHZ	Bernevig-Hughes-Zhang
TI	Topological Insulator
SS	Surface states
E_g	Energy band gap
μ	Fermi-level
TB	Tight Binding
WAL	Weak anti-localization
soc	spin-orbit-coupling
SC	Superconductor
QH	Quantum Hall Effect
QSH	Quantum Spin Hall Effect
QAH	Quantum Anomalous Hall Effect
SIA	Structural Inversion Asymmetry
BdG	Bogoliubov-deGennes

ABSTRACT

Sengupta, Parijat Ph.D., Purdue University, May 2014. Theory of topological insulators and its applications. Major Professor: Gerhard Klimeck.

An important pursuit in semiconductor physics is to discover new materials to sustain the continuous progress and improvements in the current electronic devices. Traditionally, three material types are in use: 1) Metals 2) Semiconductors 3) Insulators. All the three material types are classified according to the energy gap between conduction and valence bands derived from band theory of solids. Recent theoretical predictions and confirmed by experimental observations have provided evidence that there exists materials which behave as insulators in the bulk but possess gapless conducting states on the surface. These new class of materials are called topological insulators (TI). In this work, the electronic structure of TIs would be explained specifically answering the two important questions: 1) What distinguishes a topological insulator from a normal insulator? 2) Why topology is related to the study of insulators?

This thesis examines HgTe and Bi_2Te_3 as 2D and 3D TIs respectively. Design principles for utilizing HgTe based 2D TIs as a switch and tuning the critical width is explained. Further the surface states, which are the counterpart of the edge states in a 3D TI depend on thickness of the film, orientation, inequivalent surface termination, spin-momentum locking etc. Using a four-band k.p model, some of these features are investigated. Further, peculiarities in the electronic structure of TIs do not allow a classical methods of band structure calculation possible. A new approach which does not distinguish between electrons and holes will be presented that efficiently computes the self-consistent band structure of TIs.

Almost all known topological insulators are a direct outcome of strong spin-orbit coupling. As a break of this trend, wurtzite based nitrides are shown to possess 2D topological insulator states. The strong internal polarization of wurtzite crystal is used to invert the bands and create a 2D TI.

As an application of TIs, the current-voltage characteristics of a Bi_2Te_3 transistor that utilize the highly mobile surface states is simulated. The characteristics show that in addition to high mobility, it also offers a low-power option for designing a transistor in a fast switching environment. Additionally, a comparison between the I-V characteristics of silicon and graphene ultra-thin bodies further demonstrate the low-power utility of such devices. Difficulties with a transistor that operate exclusively with TI surface states are also highlighted.

In the last part of the work, topological insulator nanostructures are considered. In particular, TI nanowires and nanoribbons which distinctly exhibit various manifestations of well established phenomenon in condensed matter physics such as AB and SdH oscillations, WAL, Kondo effect etc. are studied. The influence of an external magnetic field on surface states is also discussed. Finally, the proximity effect of superconductors that induce a bandgap opening in a TI-SC heterostructure is computed with a modified form of the BdG Hamiltonian.

1. A PRIMER ON TOPOLOGICAL INSULATORS

1.1 Introduction

An important pursuit in semiconductor physics is to discover new materials to sustain the continuous progress and improvements in current electronic devices. Traditionally, three material types are in use: 1) Metals 2) Semiconductors, which are insulators but can be made conducting under suitable conditions such as doping and temperature and 3) Insulators. All the three material types are classified according to the energy gap between conduction and valence bands derived from band theory of solids. Recent theoretical predictions and confirmed by experimental observations have provided evidence that there exists materials which behave as insulators in the bulk but possess gap-less conducting states on the surface. These states, in a time-reversal invariant system are protected against perturbation and non-magnetic disorder. Such materials are now known as topological insulators (TI) [1, 2].

Another way of viewing topological insulators is through the concept of *order* so widely-prevalent in modern condensed-matter physics. Traditionally, our understanding of phases of matter such as solids, liquids has been based on the associated symmetries of the system. This idea is clearly seen in the phase transition of liquid atoms with rotational and translational symmetry into a crystal with discrete symmetries (e.g. translational, discrete rotational, inversion, etc.). More complex phases describable by the paradigm of symmetry breaking include ferro-magnets (rotational-symmetry breaking) and superconductors (broken-gauge symmetry). Despite the considerable success enjoyed by the Landau-Ginzburg theory of spontaneous-symmetry breaking, several notable exceptions exist that elude such as a description. Historically, the integer quantum hall effect (QHE) discovered in 1980 by Klaus Von Klitzing while examining the behaviour of electrons confined in two dimensions and subjected

to a strong perpendicular magnetic field and an in-plane electric field is regarded as the first deviation from the symmetry-breaking theory. In this particular experiment, the measured Hall conductance turned out to be in exact quantized fundamental units of e^2/h.

$$\sigma = \nu e^2/h \tag{1.1}$$

where ν assumes any integer value. Klaus von Klitzing also discovered that the two-dimensionally confined electron gas possesses a Hall resistance (Fig. 1.1) that shows a plateau like structure. This is remarkable not only because it deviates significantly from a classical linear Hall resistivity plot, the quantization described by Eq. 1.1 is independent of microscopic details,type of material used and purity of the sample. Impurities and other imperfections do not change the Hall resistivity behaviour. A complete quantum mechanical analysis of this problem as given by Macdonald is included in the appendix .

The 2DEG of a Si-MOSFET used in the QHE experiment when exposed to a strong magnetic field creates Landau levels with discrete energies forcing the electrons to move in a cyclotron orbit. The electrons executing harmonic oscillator motion are separated by energy levels $E_n = (n + 1/2)\hbar\omega$ that allow for the system to be an insulator when the Fermi energy is placed within the energy gap. Thus far, the quantum Hall sample is a true bulk insulator unless the chemical potential is aligned with one of the Landau levels. However, the experimental observation of the quantized nature of Hall conductivity is seemingly at odds with this picture. The resolution of this problem can be achieved by edges of the sample that host electronic states propagating in a chiral manner. The quest to understand this remarkably precise Hall quantization has spawned the theoretical developments that is at the heart of current world-wide focus on topological insulators. One of the primary accomplishments has been the recognition that the plateaus (which give the quantized conductance)have topological significance and cannot be explained with the bulk electronic structure. It can be explained in terms of topological invariants known as Chern numbers [4, 5].

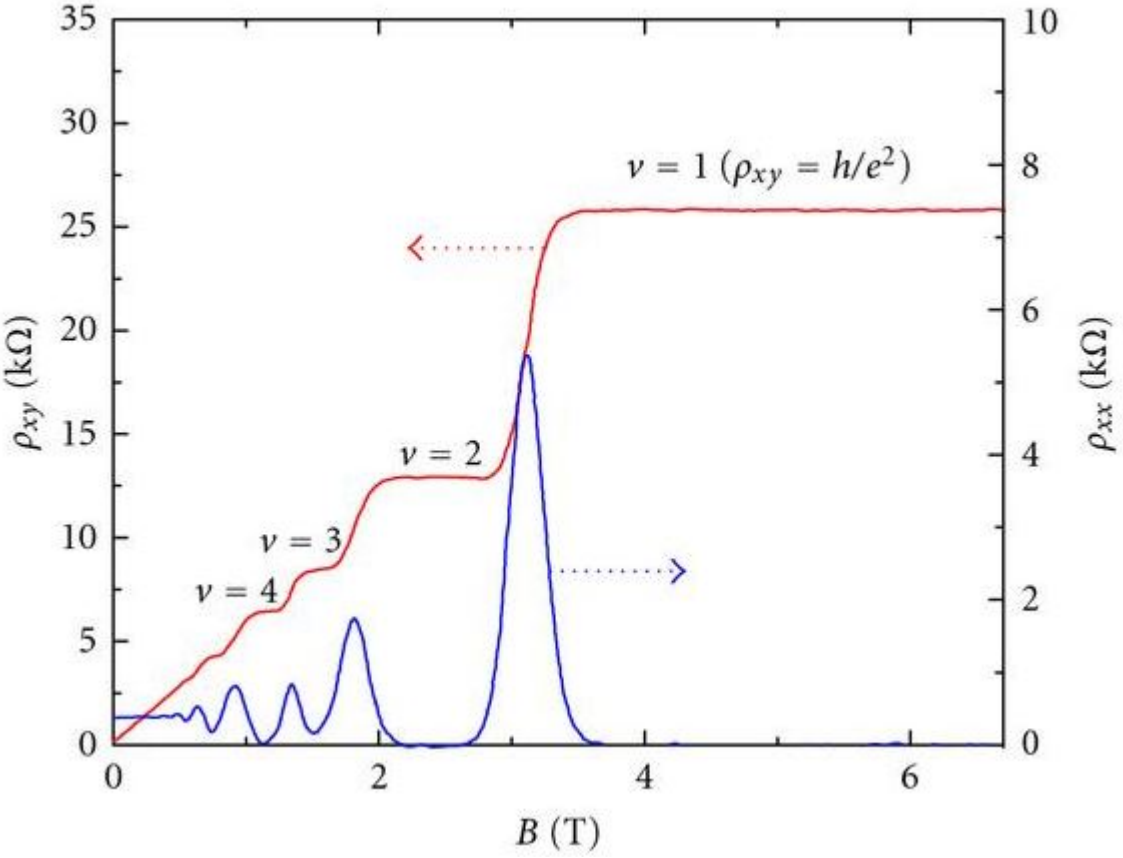

Fig. 1.1. Quantum Hall effect in a InGaAs-based heterostructure measured at 30mK [3]. The diagonal component of resistivity shows regions of zero resistance corresponding to each QHE plateau. The Hall resistivity is quantized in units of h/e^2 divided by an integer.

An integer quantum Hall phase is protected from being deformed into a phase with different topology in the same way a torus is protected from being deformed into a sphere [6, 7]. The only time such a change is possible is through a phase transition where the gap in the energy spectrum closes in a critical fashion. The Quantum Hall effect will not be elaborated in greater detail here; the interested reader can refer to extensive original literature available [8–11].

The QHE edge states are now easily understood in terms of the Laughlin picture [12] and composite fermions [13], but it is the realization that such edge states can be present in absence of a time reversal breaking magnetic field has led to the new field of topological insulators. The key difference from quantum hall systems is the absence of a magnetic field and production of double-degenerate edge states -one for each spin- as opposed to single current carrying state in the Quantum Hall effect (Fig. 1.2). In the following sections, a simple model will be presented which captures the essence of topological insulators in an otherwise insulating sample. Further details of topological insulators and their subtleties will be presented in the succeeding chapters.

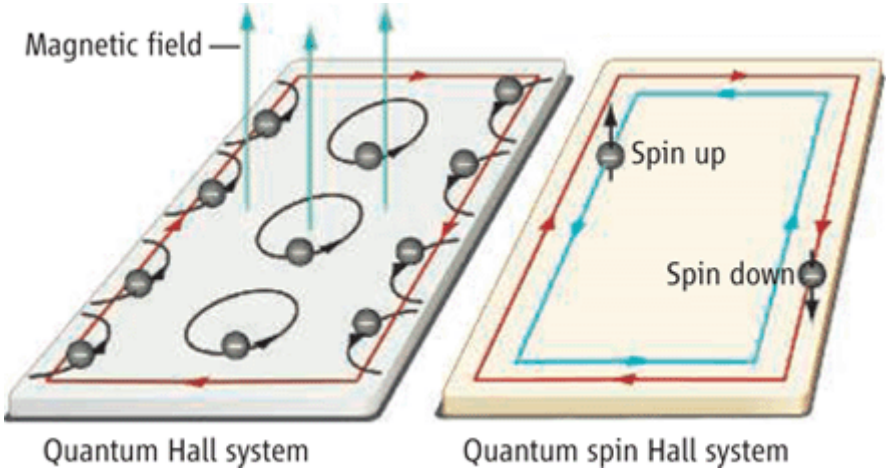

Fig. 1.2. A quantum Hall system contains a chiral state propagating along the edge of the sample, where backscattering is prohibited. The red colour around the edge of the box denotes a single channel for electrons to move forward. In a quantum spin Hall system the edge states are helical, and back scattering remains forbidden with an odd number of right or left-moving channels at each part of the sample. In contrast to the quantum hall phenomenon, the quantum spin hall system has two channels around the edge. The two channels are marked by red and blue. Each channel supports the movement of electron with a unique spin projection. This figure has been taken from Ref. [14]

Until the prediction and experimental discovery of topological insulators, the quantum hall effect was the only known realization of topological state in existence. Compared to the rich variety of traditional broken-symmetry states beginning from the ubiquitous solid-liquid and gaseous phases to superconductivity, one is led to the obvious question: should there not be other topological states remaining to be discovered? In particular, the quantum hall insulator requires a large magnetic field for its existence. A natural question to ask is whether a magnetic field, which breaks time-reversal symmetry, is a necessary condition to obtain a topological state. The first answer to this question was provided by the independent theoretical prediction by Kane and Mele [15, 16] and Bernevig and Zhang [17] of a new state of matter; the 2D time-reversal invariant topological insulator or quantum spin Hall (QSH) insulator. This state displays robust quantized properties but does not require a time-reversal symmetry breaking magnetic field for its observation. The remarkable proposal of Kane and Mele is based on the spin-orbit interaction of graphene and is mathematically

1.2 Quantum spin Hall state and 3D topological insulators

The quantum spin Hall state and quantum Hall effect differ fundamentally. Though they both exhibit chiral edge states, the presence of time reversal symmetry in QSH significantly alters the overall behaviour. In this model (Fig. 1.3), there are two edge states propagating in opposite directions with opposite spin. Because of time reversal invariance, an electron with spin-up traveling anti-clockwise must have a counterpart in spin-down electron traveling clockwise. Roughly speaking, the QSH state can be viewed as two copies of the quantum Hall state with opposite Hall conductances, opposite spin and magnetic field. Such an arrangement can originate from spin-orbit coupling which creates a momentum-dependent $\overrightarrow{B}$ field. In a pair of remarkable papers that appeared in Physical Review Letters in 2005, Kane and Mele motivated by the earlier work of Haldane [18] on the so-called quantum anomalous

Hall (QAH) effect proposed the QSH to exist in graphene. This proposal turned out to be practically unrealizable because of graphene's low spin-orbit coupling. Soon after, Bernevig, Hughes, and Zhang put forward a more realistic set-up with HgTe and CdTe quantum wells [17]. They predicted that the HgTe-based quantum well heterostructure can host pair of counter-propagating edge states which are related to each other through time-reversal symmetry. The prediction was verified by the Molenkamp group at University of Wuerzburg, Germany in 2007 [19].

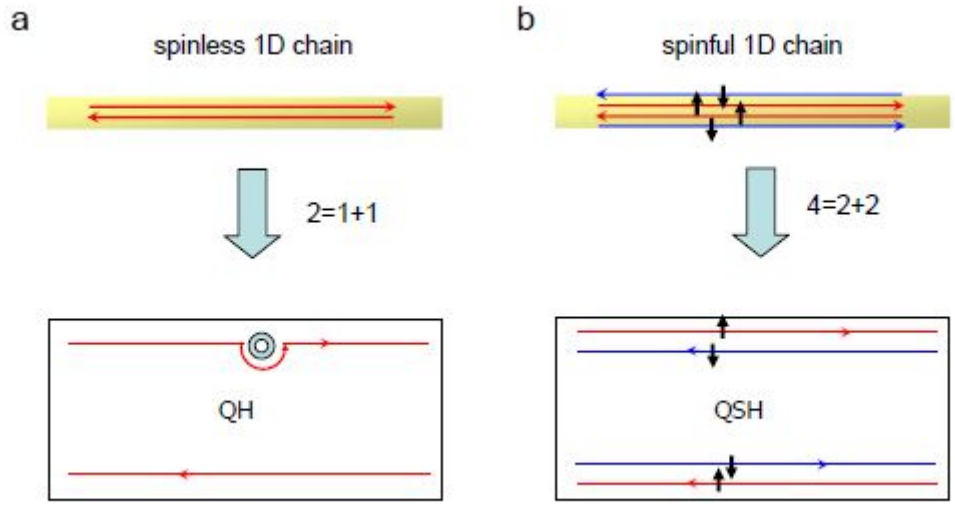

Fig. 1.3. A quantum Hall system (a) has a left and right moving set of electrons along the two edges of the quantum Hall bar. A QSH (b) on the other hand has a left and right moving set of electrons on each edge. Both edges now have two group of electrons moving in opposite directions but with anti-parallel spin. This figure is from Ref. [20]

It is now natural to enquire if there exists a 3D version of the QSH state. In 2008, a 3D system ($Bi_{0.9}Sb_{0.1}$) which guarantees the presence of surface states was discovered through ARPES experiments [21]. It was found that the states have a linear dispersion, close the bandgap on the surface and retain a gapped spectrum in the bulk. Several theoretical predictions [22, 23] preceded this experiment and they were all related to the spin-orbit coupling of the material. Following the initial

discovery several other compounds that possess a bandgap closing surface state were discovered. Prominent examples of such compounds are Bi_2Te_3, Bi_2Se_3, and Sb_2Te_3. In brief, the 3D topological insulator has a tunable parameter (the intrinsic spin-orbit coupling) that enables transition from a topologically non-trivial to trivial insulator. When the topological insulator has an interface with a trivial insulator a band gap closing state is present on the surface.

1.3 Effective Hamiltonians

ARPES experiemnts [24, 25] have shown that several 3D topological insulators have surface states that consist of a single Dirac cone (Fig. 1.4) at the Γ point. Similarly, a Dirac dispersion also governs the edge states of a 2D topological insulator (QSH system). For the two cases, an effective energy Hamiltonian can be written in the simplest form. A QSH edge state (Eq. 1.2) is given as

$$H = \hbar v_f \sigma_x k_y \tag{1.2}$$

while a 3D TI surface state is characterised by Eq. 1.3

$$H = \hbar v_f \left(\sigma_x k_y - \sigma_y k_x\right) \tag{1.3}$$

3D TIs allow momentum to be in any in-plane directions while 2D TIs are confined to one-dimensional $\overrightarrow{k}$ space.

The Hamiltonian of Eq. 1.3 can be diagonalized to obtain the eigen vectors and eigen states as

$$E = \hbar v_f |\overrightarrow{k}| \tag{1.4}$$

and

$$|\psi_k\rangle = \frac{1}{\sqrt{2}}(\pm i e^{-i\theta}|\uparrow\rangle + |\downarrow\rangle) \tag{1.5}$$

It is easy to see from Eq. 1.5 that the spin-momentum relationship is uniquely determined. The spin is always perpendicular to the momentum vector due to additional

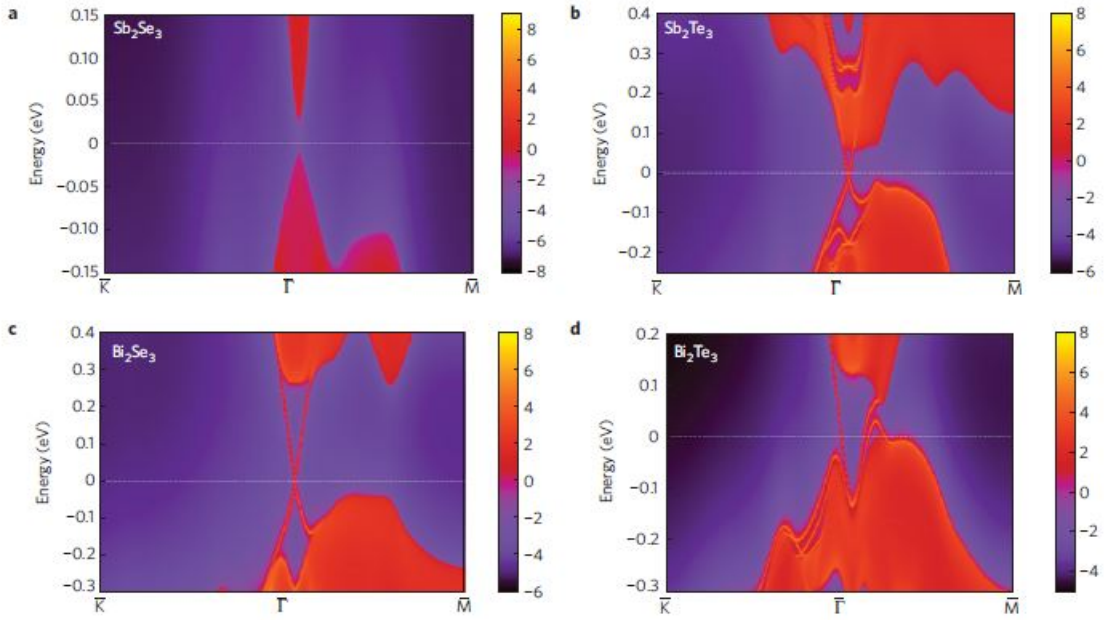

Fig. 1.4. Dispersion relationship for Sb_2Se_3 (a), Sb_2Te_3 (b), Bi_2Se_3 (c) and Bi_2Te_3 (d) on the [111] surface. All the tellurides and selenides except for Sb_2Se_3 have a linearly dispersing surface state at the Γ point. Figure taken from [25]

i prefactor in the eigen vector. Every momentum direction is locked to one spin direction. The spin-momentum locking gives the helical character to the surface states of a topological insulator.

This concludes a simple introduction to the paradigm of topological states as a way of classifying phases of matter. The 2D and 3D variants of topological insulators that exist, the materials that have been experimentally verified to possess such characteristics were introduced. Additionally, their relationship to the quantum Hall system which is a precursor to the current research on topological insulators was examined. In Chapter 2, the reason behind existence of edge states in a QSH system and surface states in a 3D topological insulator from a electronic structure perspective will be thoroughly addressed.

2. ELECTRONIC BAND STRUCTURE OF TOPOLOGICAL INSULATORS

2.1 Introduction

In condensed matter physics, electronic structure theory [26] allows a description of the energy bands electrons occupy in a crystalline solid. It helps to explain the macroscopic properties of materials such as electrical and thermal conductivity, optical absorption etc. Generally, calculating the complete energy profile is an intractable problem because an electron at any instant is subjected to interaction with the nucleus and the surrounding electron cloud. Several approaches have been adopted, notably the assumption that a single-particle picture instead of a many-particle formalism can reproduce the essential details correctly. This chapter introduces the tight-binding and k.p semi-empirical approaches to obtain the energy dispersion relationship for topological insulators. Using results determined by these two methods and also examining the electronic Hamiltonian, key properties of topological insulators will be pointed out.

As mentioned in Chapter 1, Kane and Mele proposed graphene a monolayer of carbon atoms as a possible candidate for the observing protected edge states without an external magnetic field. Unfortunately, this proposal turned out to be unrealistic because the spin-orbit gap in graphene is extremely small. This effect was also independently proposed in semiconductors in the presence of strain gradients, but this proposal also turned out to be hard to realize experimentally. Soon afterwards, Bernevig, Hughes, and Zhang initiated the search for the QSH state in semiconductors with an inverted band structure, and predicted a quantum phase transition in type-III HgTe/CdTe quantum well between a trivial insulator phase and a quantum spin hall phase (QSH) governed by the thickness of the well. The QSH state was observed

experimentally observed in 2007 by König at the University of Wüzburg, Germany. The HgTe/CdTe well structure is described in detail in the next chapter. Simple mathematical arguments are presented in this section which lead us to the desired form of the Hamiltonian for topological insulators.

The Lorentz force, which drives the quantum hall state and is the immediate theoretical precursor to QSH and 3D-topological insulators, attributes a $\vec{A} \cdot \vec{P}$ term in the Hamiltonian. In terms of the symmetric gauge the vector potential $\vec{A}$ can be written as:

$$\vec{A} = \vec{B}/2(y, -x, 0) \tag{2.1}$$

where $\vec{B}$ is the applied external magnetic field. which then gives a Hamiltonian of the form [17]

$$H \propto (xp_y - yp_x) \tag{2.2}$$

Therefore, Bernevig et. al. argued, the goal is to look for another force in nature which produces a similar Hamiltonian. The obvious candidate is the spin-orbit coupling force. Its Hamiltonian is of the form

$$H_{spin-orbit} = \vec{E} \times \vec{P} \cdot \sigma \tag{2.3}$$

where σ is the Pauli spin matrix. Instead of an external $\vec{B}$ field, an external $\vec{E}$ field is used which preserves time reversal symmetry. If one considers a $\vec{E}$ field of the form E($\vec{x}$+ $\vec{y}$), the corresponding Hamiltonian becomes:

$$H_{spin-orbit} = \vec{E}\sigma_z(xp_y - yp_x) \tag{2.4}$$

The form of $\vec{E}$ considered is assumed to be confined in a two dimensional plane (along with the particle momentum), therefore only the z component of the spin enters the Hamiltonian.

Equation 2.4 is exactly identical to the representative equation (eq. 1.3) shown in Chapter 1. This therefore points that spin-orbit coupling may be an essential requirement in obtaining topological insulator states.

2.2 Band inversion in topological insulators

The necessary condition for a compound to behave as a topological insulator is an odd number of band inversions [27] between the conduction and valence bands. This band inversion (explained in more detail in the next section) can be brought about by primarily by spin-orbit coupling which exerts a significant influence in compounds with heavy elements. An illustration of band inversion is shown in Fig. 2.1 and Fig. 2.2. An energy gap which emerges at the points the conduction and valence bands cross each other is called band anti-crossing. When such an inversion happens an odd number of times in the complete Brillouin zone, a topological insulator is formed. This must be though differentiated (Fig. 2.3) from the well-known Rashba spin-orbit splitting. The Rashba effect is related to the conduction and valence bands and can be smoothly deformed in to the bulk bands which is equivalent to a fully gapped structure.

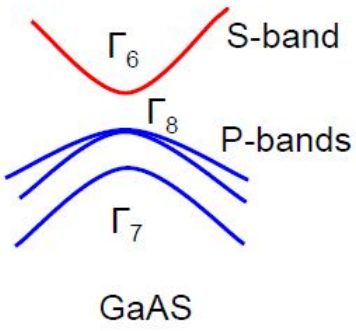

Fig. 2.1. Band dispersion of GaAs at the Γ point.

2.3 Bulk boundary correspondence

This deep connection between the bulk and boundary which manifests itself in the form of robust surface states can be intuitively understood in the following way. If we have a smooth interface between two materials with opposite signs of the bulk band-gap, (strictly speaking these are called as belonging to two different topological

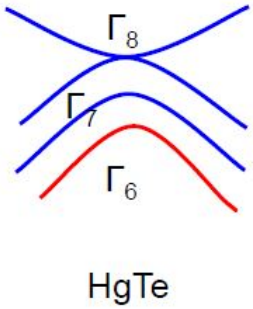

Fig. 2.2. Band dispersion of HgTe at the Γ point. The lowest point of the conduction band is below the top of the valence band. This is opposite to normal sequence of bands, for example, in GaAs. Such an ordered system of bands is called band inversion.

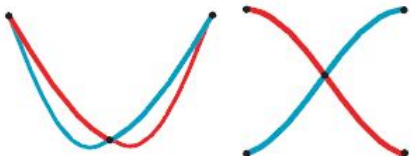

Fig. 2.3. Schematic surface states of a Rashba split system (left) and a topological insulator. The point of intersection of bands is a time reversal invariant (TRIM) point which Kramers degenarate. Fig is from Ref. [28].

classes) the band structure changes slowly as a function of position across the interface. The energy gap has therefore to vanish somewhere along the way, otherwise the two materials would belong to the same topological class. It then follows that there exists mid-gap surface states bound to the interface. The surface of a crystal can be viewed as an interface with vacuum which is considered to be a normal ordered material.

A better way of representing vacuum is to consider the surface of the topological insulator. The surface is a thin slice of the bulk material which is tightly confined. Due to confinement effects, electrons are pushed above the holes. As a consequence, the ordering of bands at the surface changes from an inverted to normal material.

This is purely a confinement effect and no other physics enters the picture. But the bulk, at certain points is still inverted. An interface is therefore created between a normal and inverted material. This leads to the formation of mid-gap states. In the following section the idea of Time-Reversal-Invariant-Momenta (TRIM) points will be introduced. TRIM points are important because the mid-gap surface state is always formed at one of these points and there must be an odd number of crossings of the surface bands and Fermi-level between two TRIM points. An even numbered crossing will destroy the surface state and make the system fully gapped. It is easy to visualize though why an odd number of crossings is necessary to have a surface state bearing in mind the basic notion that such a state joins the conduction and valence band together.

2.4 The TRIM points and the Z_2 invariant

In the bulk of a three dimensional material, time-reversal symmetry holds.This means that eqn(2.5) is true.

$$E\left(\vec{k},\uparrow\right) = E\left(-\vec{k},\downarrow\right) \tag{2.5}$$

Additionally, if inversion symmetry holds the following relation is also true.

$$E\left(\vec{k},\uparrow\right) = E\left(-\vec{k},\uparrow\right) \tag{2.6}$$

If both equation(2.5) and equation(2.6) are simultaneously satisfied, bands are spin degenerate at the same $\vec{k}$ point.

$$E\left(\vec{k},\uparrow\right) = E\left(\vec{k},\downarrow\right) \tag{2.7}$$

In general, inversion symmetry is satisfied at special points in the Brillouin zone. These high symmetry points satisfy eqn(2.7). For reasons explained below they are known as Time Reversal Invariant Momenta (TRIM) points. When the surface bands close the gap, the conduction and valence bands meet at a certain point on the surface (in k-space). Now each conduction and valence band has two components

corresponding to the spin projections. The two components would meet at one of the TRIM points for both conduction and valence bands. But since these points are stable when time symmetry is maintained, the crossing of bands at TRIM points is robust and impervious to non-magnetic perturbations. Presence of a magnetic field would destroy the time symmetry and a gap would open up compared to the zero band-gap system. On a surface which is two dimensional there are four such TRIM points: $(\pi, 0), (\pi, \pi), (0, \pi), (0, 0)$. There is another important property of topological insulator: The surface bands intersect the fermi-level an odd number of times between two TRIM points. A trivial insulator has an even number of crossings. This has led to the classification now known as the Z_2 number.

The two cases between a trivial and topological insulator can be distinguished by defining an index

$$N_k = m \quad mod \quad 2 \tag{2.8}$$

where N_k is the number of Kramers pair of edge states that cross the Fermi energy. The expression for the index given in eqn(2.8) simply means $m + 2p$, where p is any integer. If N_k is even, then $m = 0$, whereas $m = 1$ corresponds to N_k is odd. Since there are only two possible values of m, m is termed as being a Z_2 invariant. Z_2 is the group with two elements, namely 1 and 0 and hence is the simplest non-trivial group.

2.5 Topological insulator family of compounds

2.5.1 2D topological insulators: The HgTe family

HgTe is a 3D topological insulator which will be described in the next section. Here 2D topological insulators which host an edge state and found in the HgTe/CdTe quantum well heterostructure will be briefly explained. A full description is Chapter 3 of this thesis. In 2006, Bernevig, Hughes, and Zhang predicted that HgTe quantum wells would be 2D topological insulators. The HgTe quantum well is sandwiched between two CdTe barriers. CdTe has a band structure near Γ point similar to

GaAs sketched in Fig. 2.1. The conduction and valence bands in CdTe are separated by a large band gap of around 1.6 eV. Mercury being a heavier compound has a larger Darwin component [29, 30] that in conjunction with spin-orbit coupling shifts the p-type valence bands above the s-type conduction band at Γ point. The cubic symmetry of HgTe ensures that the p-type bands are degenerate at the Γ point. HgTe is therefore a zero band-gap semiconductor [31, 32] with inverted band structure.

HgTe opens a bandgap when the cubic symmetry is broken by destroying the crystal periodicity. An easy way of accomplishing this is reduction in dimensionality. An HgTe quantum well is a 2D periodic structure and has a finite bandgap at the Γ point. At a quantum well thickness smaller than the critical value, HgTe has a finite positive bandgap like CdTe and possesses no edge states. When the well thickness is increased, the structure reverts back to an inverted band order and exhibits edge states.

While an eight-band k.p Hamiltonian describes the full set of six valence (including spin split-off) and two conduction bands and their mutual interaction through the off-diagonal terms, it is sufficient to focus on bands that exclusively take part in the inversion process [33, 34]. This interaction of bands is governed by the coupling of conduction and valence states, represented through a linear term as shown in (6.3).

$$H(k) = \epsilon(k) + \begin{pmatrix} M_0 + M_2k^2 & A(k_x + ik_y) & 0 & 0 \\ A(k_x - ik_y) & -M_0 + M_2k^2 & 0 & 0 \\ 0 & 0 & M_0 + M_2k^2 & A(-k_x + ik_y) \\ 0 & 0 & A(-k_x - ik_y) & -M_0 + M_2k^2 \end{pmatrix} \quad (2.9)$$

where

$$\epsilon(k) = (C_0 + C_2k^2)I_{4\times4} \quad (2.10)$$

describes band bending. $2M_0$ = -E_{g0} corresponds to energy gap between bands and is negative in the inverted order bands.

This Hamiltonian is written in the basis of the lowest quantum well subbands $|E+\rangle$, $|H+\rangle$, $|E-\rangle$, and $|H-\rangle$. Here, ± stands for the two Kramers partners. The

sign of the gap parameter M determines if it is a trivial insulator ($M > 0$) or a topological insulator ($M < 0$). Experimentally, M is tuned by changing the quantum well width.

It must be mentioned here that the well know GaSb/InAs broken gap heterostructure is also a 2D topological insulator [35,36]. The band inversion in this system is not due to spin-orbit coupling but an odd arrangement of conduction and valence band edges. The conduction band edge of InAs (Fig. 2.4) at the Γ point falls energetically below the valence band edge of GaSb. This class of 2D topological insulators will not be pursued further in this thesis.

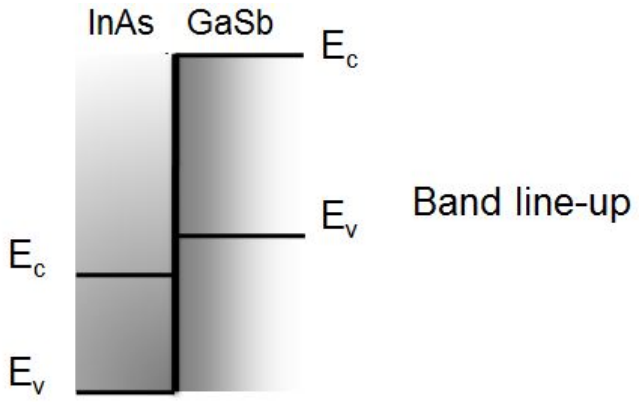

Fig. 2.4. Conduction and valence band edge for GaSb and InAs. The conduction band edge of InAs lies below the valence band edge of GaSb creating an inverted band order. Topological edge states have been observed in GaSb/InAs quantum wells [37].

2.5.2 Three dimensional topological insulators

3D topological insulators were predicted immediately after the theoretical prediction of quantum spin hall effect in 2006. Several key papers [38, 39] pointed to the possible existence of surface states. Bi_xSb_{1-x} was the first predicted 3D topological insulator which was subsequently observed by the Hasan group at Princeton through ARPES experiments [21, 40, 41]. The 3D topological insulators can be grouped in

to three categories. They are s-p, p-p, and d-f. Of these three groups, the second group of p-p type will be discussed more extensively in this thesis. The genesis of this nomenclature lies in the inversion of orbitals involved in the bulk band structure.

2.5.3 s-p type

HgTe is the primary example of s-p type 3D topological insulator. The Γ_6 state in HgTe are below the Γ_8 state thus making it an inverted material. The non-trivial topological behaviour of HgTe was first worked out Bernevig, Hughes, and Zhang and topological invariants were computed by Fu and Kane [42].The important point is that s and p orbitals at the Γ point have opposite parity values. The occupied s state is Γ_7^- while p states form Γ_7^+ and Γ_8^+. Closely related to HgTe, the half-Heusler group of compounds [43, 44] are topological insulator materials [45, 46]. They are of the form XYZ where Y and Z form a zinc-blende structure. X and Y are rare earth or transistion metals and Z is a main group element. Few other compounds of the s-p type topological insulator class are KHgSb [47, 48], Na_3Bi [49], and $CsPbCl_3$ [50].

2.5.4 p-p type

The simplest examples of p-p type topological insulators are Bi_2Se_3, Bi_2Te_3, and Sb_2Te_3. They consist of a single Dirac cone as their surface states. Of these three compounds, Bi_2Se_3 has been widely studied because of an energy-gap of 0.3 eV which is larger than the energy scale at room temperature. As an illustration of the crystal structure of these compounds, Bi_2Te_3 is chosen as an example. The undoped Bi_2Te_3 is a narrow band-gap semi-conductor with a rhombohedral crystal structure. The unit cell contains five atoms, with quintuple layers ordered as Te(1)-Bi-Te(2)-Bi-Te(1). As shown in Fig.2.5, the crystal has a layered structure stacked along z direction with five atoms in one unit cell. The five atoms can be grouped as two Bi atoms and three Te atoms. The Bi atoms are equivalent. Further, the three Te atoms include two equivalent Te atoms (Te1) and an in-equivalent Te2 atom. The Te2 atom is the

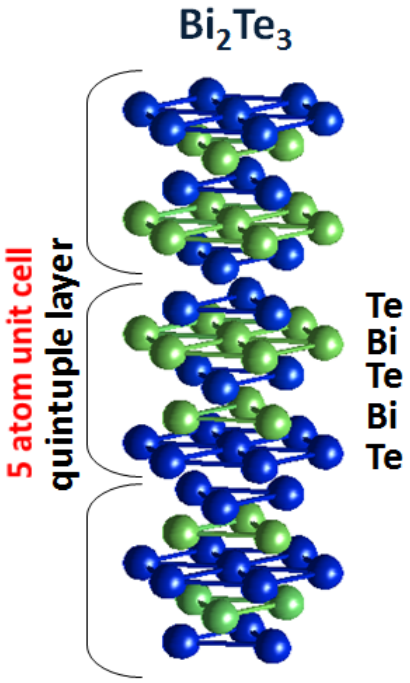

Fig. 2.5. Model sketch of Bi_2Te_3 crystal structure. The unit cell contains five atoms ordered as Te(1)-Bi-Te(2)-Bi-Te(1).

centre of inversion for this unit cell. Each atomic layer forms a triangle lattice, which has three possible positions, denoted as A, B and C, as shown in Fig.2.6. Along the z direction, the triangle layers are stacked in the order A-B-C-A-B-C. For example, in one quintuple layer, the Te1 atoms occupy the A node; in the next quintuple layer, the Te1 atoms do not occupy node A but will be located at nodes B or C. A complete description of the electronic structure of these compounds by taking Bi_2Se_3 as an example is available in literature [51]. It suffices to state here that the strong spin-orbit-coupling in Bi_2Se_3 leads to band inversion at the Γ point. The orbitals involved in this band formation are of p-type.

2.6 Tight-binding model for p-p type 3D topological insulators

The quintuple layer crystal structure is imported to a twenty band tight binding model for 3D TIs. All parameters for these calculations were obtained from a orthog-

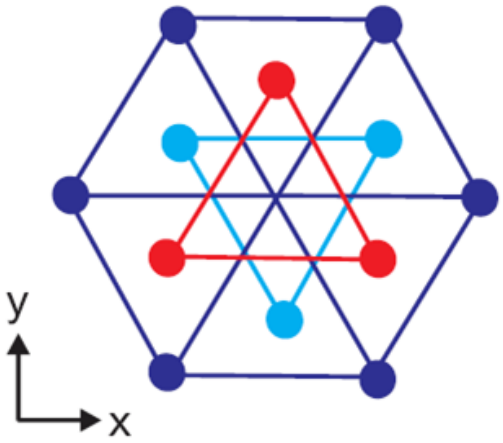

Fig. 2.6. The in-plane triangle lattice has three positions A,B,and C marked by different colours.

onal tight-binding model with $sp^3d^5s^*$ orbitals, nearest-neighbour interactions, and spin-orbit coupling [52]. Dispersion relationships (Fig. 2.7) obtained from the tight binding model was spin resolved along the quantized growth axis to identify spin polarization of the bands. For a strong topological insulator behaviour, it is mandatory to have strong spin-polarized surface bands. A MATLAB script used to obtain the spin-polarization of bands is included in Appendix.

Surface states are usually modeled analytically by a simple Hamiltonian (Eq. 2.11) of the form

$$H_{SS} = v_f \left(\overrightarrow{k} \times \overrightarrow{\sigma} \right) \tag{2.11}$$

This equation correctly reproduces the linear dispersion, spin-polarization, and the geometric Berry phase of π [54]. It has been experimentally observed [55] though and explained with a phenomenological k.p theory [53] that the Fermi surface of Bi_2Te_3 is not a circular contour but a warped structure at energies away from the Dirac point. The same behaviour (Fig. 2.8) is also reproduced with the twenty-band tight binding model. It is important to note here that additional cubic terms of the form given in

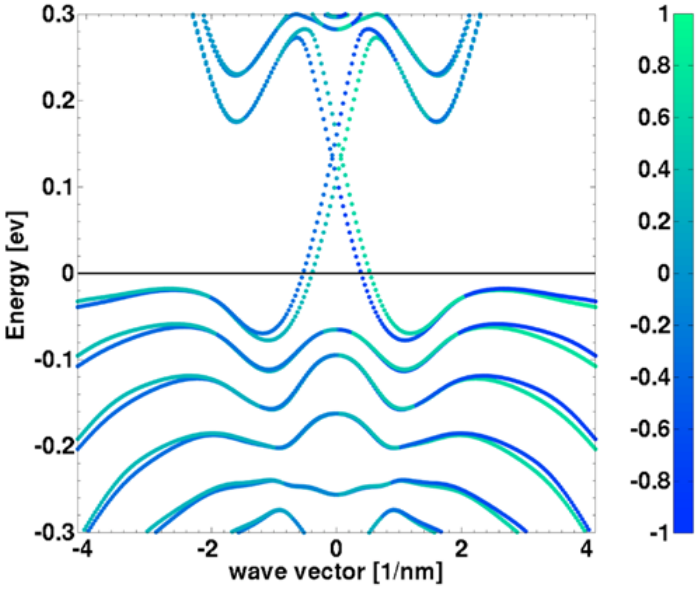

Fig. 2.7. The surface states of a topological insulator computed with the twenty-band tight binding method. The conduction and valence bands are connected together by a cone of states at the Γ point. The meeting of the conduction and valence bands is usually a linear dispersion also known as a Dirac cone. The colour bar indicates the spin-polarization of the bands. The surface state bands are completely spin polarized.

Eq. 2.12 are not needed. The full symmetry of the Hamiltonian is captured in the tight-binding model.

$$H = \hbar v_f \left(\sigma_x k_y - \sigma_y k_x\right) + \frac{\lambda}{2}\left(k_+^3 + k_-^3\right) \tag{2.12}$$

The k^3 correction preserves time reversal and the C_{3v} point-group symmetry and breaks the isotropic surface state Hamiltonian.

A simplified k.p Hamiltonian using the method of invariants can also be constructed (Eq. 9.1) in terms of the four lowest low-lying states $|P1_z^+ \uparrow\rangle$, $|P2_z^- \uparrow\rangle$, $|P1_z^+ \downarrow\rangle$, and $|P2_z^- \downarrow\rangle$. Additional warping effects [53] that involve the k^3 term are omitted in this low-energy effective Hamiltonian. A fuller description of this Hamiltonian is given in Chapter 7 (Topological nanostructures).

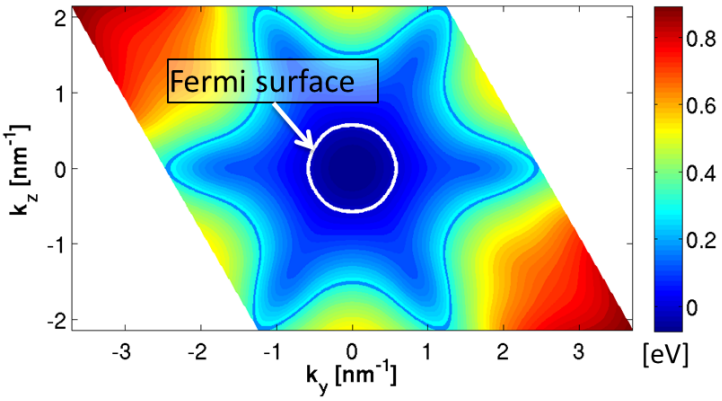

Fig. 2.8. The warping of the constant energy contour in to a snow-flake structure at energies away from the Dirac-point. This figure has been produced with a twenty-band tight binding model and matches well with the experimental data reported in literature (Fig. 2.9).

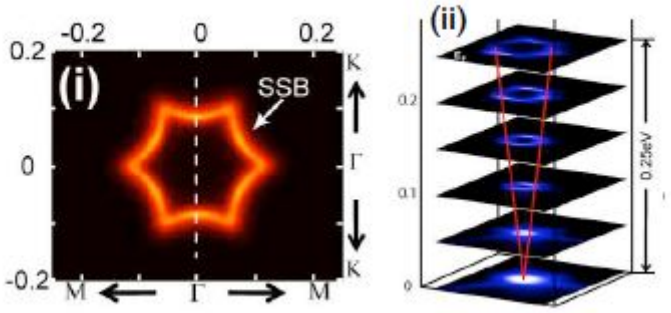

Fig. 2.9. Snow-flake like Fermi surface of the surface states on Sn-doped Bi_2Te_3 observed in ARPES. The figure on the right shows a set of constant energy contours at different energies. Figure is from Ref. [53]

$$H(k) = \epsilon(k) + \begin{pmatrix} M & iA_1k_z & 0 & A_2k_- \\ 0 & -M & A_2k_- & 0 \\ 0 & A_2k_+ & M & -iA_1k_z \\ A_2k_+ & 0 & -iA_1k_z & -M \end{pmatrix} \tag{2.13}$$

where

$$\begin{aligned} \epsilon(k) &= (C + D_1k_z^2 + D_2\left(k_x^2 + k_y^2\right))I_{4\times4} \\ M &= M_0 - B_1k_z^2 - B_2\left(k_x^2 + k_y^2\right) \\ k_\pm &= k_x \pm ik_y \end{aligned} \tag{2.14}$$

This review of electronic structure of topological insulators introduced the idea of topologically non-trivial materials, band inversion, TRIM points, and the Z_2 invariant. Several topological insulators have been discovered but it is crucial to find more that have suitable properties. A large band-gap is essential, until now the largest band gap is 0.3 eV in Bi_2Se_3. Later chapters examine the problem of transport using these surface states.

3. DESIGN PRINCIPLES FOR HGTE BASED TOPOLOGICAL INSULATOR DEVICES

3.1 Introduction

In this chapter the topological insulator properties of CdTe/HgTe/CdTe quantum wells are theoretically studied. CdTe-HgTe-CdTe quantum wells which were the first predicted TIs are 2-D topological insulators (2D TI). Unlike their 3D counterpart, they possess bound states at the edge of the quantum well. The CdTe/HgTe/CdTe quantum well behaves as a topological insulator beyond a critical well width dimension. It is shown that if the barrier(CdTe) and well-region(HgTe) are altered by replacing them with the alloy $Cd_xHg_{1-x}Te$ of various stoichiometries, the critical width can be changed. The critical quantum well width is shown to depend on temperature, applied stress, growth directions and external electric fields. Specifically, the transition from an NI to a TI through external adiabatic parameters, adjustable lattice constants, or modulation of the electron-hole band coupling is the underlying theme. Based on these results, a novel device concept is proposed that allows to switch between a normal semiconducting and topological insulator state through application of moderate external electric fields.

3.2 The 8-band k.p method for HgTe/CdTe quantum well heterostructure

An HgTe quantum well flanked by CdTe barriers has been shown to have edge states with topological insulator properties. TI behaviour is possible because CdTe is a normal insulator and is placed in contact with an inverted insulator HgTe. A representative sketch of the device is shown in Fig.3.1. CdTe is a wide band gap

semiconductor (E_g = 1.606 eV) with positive energy gap (NI) and a small lattice mismatch of 0.5% with HgTe. CdTe, because of similar lattice constants is chosen as the barrier for the HgTe well region though in principle any normal ordered material would suffice. The normal valence and conduction band are reversed in their energetic order in HgTe as indicated in Fig. 3.1 and explained in the next paragraph.

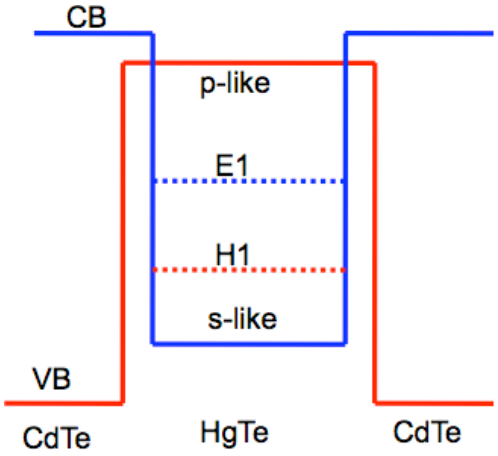

Fig. 3.1. Sketch of a CdTe/HgTe/CdTe quantum well heterostructure. The lowest conduction band (CB) state is labeled with E1 and the highest valence band (VB) state with H1.

The inversion of bands for the CdTe/HgTe/CdTe heterostructure is achieved through the HgTe component. Both CdTe and HgTe belong to the zinc blende (ZB) structure with T_d point group symmetry. The highest valence and lowest conduction band is made up of p and s orbitals respectively. A *normal* band order at Γ has lowest conduction band ($j = 1/2$) with Γ_6 symmetry above the top of the valence bands ($j = 3/2$) with Γ_8 symmetry. The Γ_6 state has s-type symmetry and the Γ_8 state has p-type symmetry. In a normal ordered material Γ_6 state is energetically higher than the Γ_8 state. This order is reversed in bulk HgTe at the Γ point due to the high spin-orbit coupling and a significant Darwin term contribution. [56] The strong spin orbit coupling pushes the valence bands upwards while the Darwin term shifts the s-type conduction band down. The Darwin term can only influence the s-type bands. [57] The combined effect of spin orbit coupling and Darwin term yields

an inverted band order at the Γpoint which flips the order of the high-symmetry Γ_6 and Γ_8 points for HgTe. [58]The energy gap at Γ which is defined as

$$E_g = E(\Gamma_6) - E(\Gamma_8), \tag{3.1}$$

therefore turns out to be negative for HgTe. The *normal* and *inverted* band structures of CdTe and HgTe are illustrated in Fig. 3.2(a) and Fig. 3.2(b) respectively. Throughout it is assumed that local impurities at surfaces and interfaces do not alter the fundamental ordering of bands. This assumption is valid as long as impurities only perturb the bandstructure but do not dominate it.

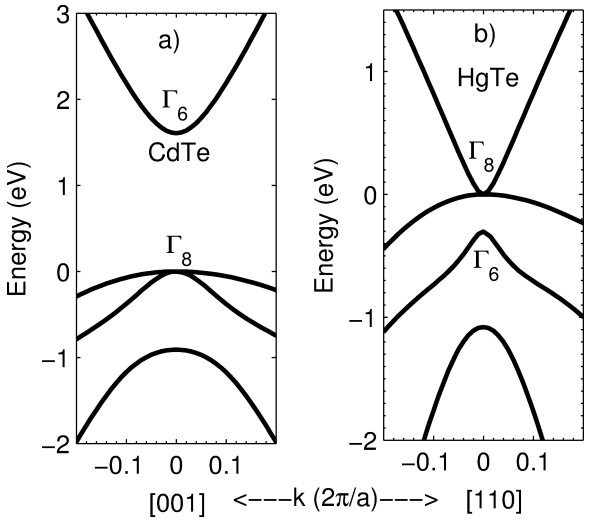

Fig. 3.2. Bulk band structure of CdTe (a) and HgTe(b). The ordering of the conduction and valence bands near the band gap at the Γ point in HgTe (Fig. 3.2b) is opposite to the one in CdTe (Fig. 3.2a). In HgTe, the hole state Γ_8 is above the electron state Γ_6.

The electronic properties of the ⟨001⟩ CdTe/HgTe/CdTe heterostructures are calculated within an 8-band k.p framework that includes a linear coupling between conduction and valence bands. [59, 60] Compared to other electronic models, this method combines the many band aspect of empirical pseudopotential or tight binding methods with the efficiency of envelope function approximations. In addition, the k.p method is particularly valid around the Γ point where the relevant physics of all

devices of this paper is determined. In contrast to most other empirical methods, parameters for the present CdTe/HgTe material system are well established for the k.p framework.

In the calculations presented, the z-axis is normal to the heterostructure and is also the confinement direction. The valence band edge E_v, Luttinger parameters, and other related material properties are collected in Table 3.1. The boundary conditions are imposed by setting the wave function to zero at the edge of the device. When the CdTe/HgTe/CdTe structure is grown along a different axis the $\langle 001 \rangle$ Hamiltonian is rotated accordingly. Strain is added to the electronic Hamiltonian using deformation potentials defined in the Bir-Pikus method. [61, 62] This method requires to add to the Hamiltonian

$$\{H_{\text{strain}}\}_{ij} = \sum_{\alpha,\beta=1}^{3} D_{ij}^{\alpha\beta} \varepsilon_{\alpha\beta}, \tag{3.2}$$

with the strain tensor $\varepsilon_{\alpha\beta}$ and the deformation potential operator $D_{ij}^{\alpha\beta}$. All non-vanishing electric fields in are considered to be applied along the confinement direction. Non-vanishing fields are included in the Hamiltonian as their corresponding electrostatic potentials which are solved with Dirichlet boundary conditions.

Table 3.1
8-band k.p parameters for CdTe and HgTe. E_v, E_g, P_{cv}, and V_{so} are in units of eV. The remaining Luttinger parameters are dimensionless constants and the effective mass is in units of the free electron mass.

Material	E_v	γ_1	γ_2	γ_3	m^*	E_g	P_{cv}	V_{so}
CdTe	-0.27	5.372	1.671	1.981	0.11	1.606	18.8	0.91
HgTe	0.0	-16.08	-10.6	-8.8	-0.031	-0.303	18.8	1.08

3.3 Results

Comparison with experiment: band gap and critical width: Experiments report that a CdTe/HgTe/CdTe quantum well heterostructure with a well width

under 6.3 nm exhibits a normal band order with positive E_g. [63,64]. The calculation of the present work confirms that the conduction states at Γ are indeed located above the valence states and the energy gap is positive (Fig. 3.4(a)). All band structure parameters used to reproduce the experimental observation were valid at 0 K. When the well width is exactly 6.3 nm, a Dirac system [65] is formed in the volume of the device (Fig. 3.3).

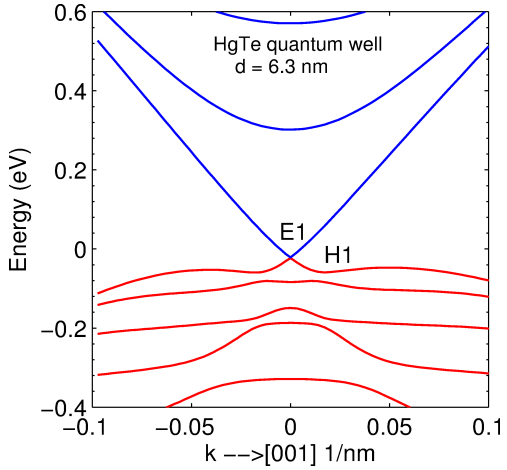

Fig. 3.3. Band structure of HgTe quantum well of thickness 6.3 nm. At this width, the lowest conduction band (E1) and highest valence band (H1) at the Γ point are equal.

Beyond this *critical well width* of 6.3 nm, the heterostructure has its bands fully inverted. The band profile has a reverse ordering of the s-type and p-type orbitals (Fig. 3.4(c)) and $E_g < 0$.

Accordingly, a nano-ribbon of width 100.0 nm formed by quantizing the quantum well in its in-plane direction has a positive band gap (as shown in Fig. 3.4b). Similarly, a nanoribbon of width 100.0 nm constructed out of an inverted quantum well possesses gap-less TI edge states. The band structure of this situation is illustrated in Fig. 3.4(d).

The corresponding absolute value of the squared edge-state wave functions is plotted in Fig. 3.5. The absolute value of the wave functions for the two edge states is

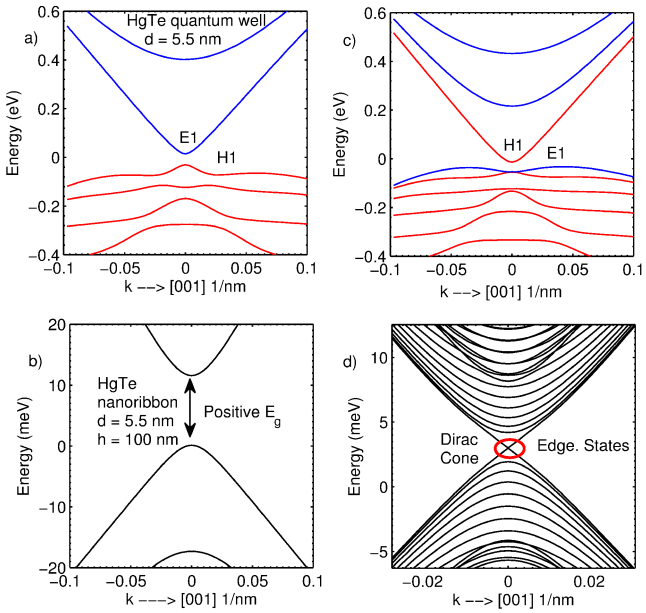

Fig. 3.4. Bandstructure of a HgTe quantum well of thickness 5.5 nm(a). A HgTe nano-ribbon formed out of this quantum well of thickness 5.5 nm and height of 100 nm shows a positive band gap. Fig. 3.4c shows the bandstructure of an inverted quantum well of thickness 10.0 nm. The corresponding quantum wire has a linearly dispersing (Dirac-cone) edge states (d).

maximum at the edge and gradually decay in to the bulk. This establishes that they belong exclusively to the edge states. In conclusion, the band-gap closing Dirac cone shown in Fig. 3.3 marks the transition from a positive band-gap to a negative one.

Band nature at finite momenta: The inversion of bands in the volume of the well is necessary for edge states with topological insulator behaviour. It is important to note however, that the process of inversion happens only at the Γ point. In the inverted dispersion plot (Fig. 3.4c), for momenta different from the Γ point, the band labeled with "H1" progresses from p to s-type. Similarly the band labeled with "E1" changes character from s to p. Both the bands, at a finite momentum acquire atomic orbital characteristics associated with a normally ordered set of bands. TI behavior is therefore restricted to a special set of momentum points where the band structure

is inverted. These set of points are collectively called the time-reversal-invariant-momentum (TRIM) points. [38]

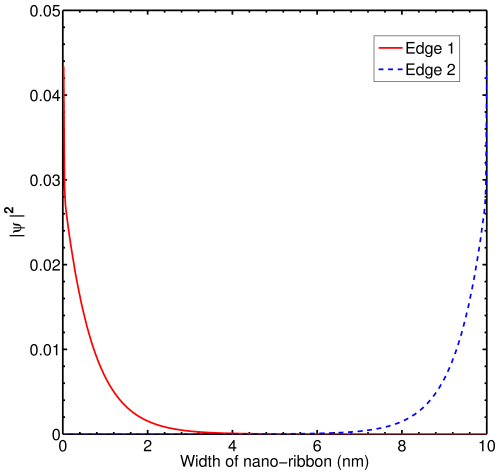

Fig. 3.5. Absolute value of the wave functions $|\psi|^2$ of the two edge-states of Fig. 3.4d.

Well thickness continuously tunes the TI properties: With increasing well width, the band gap decreases continuously until the HgTe well thickness reaches 6.3 nm (see Fig. 3.6). This is due to the diminishing confinement of the well's s and p-type bands. For well thicker than 6.3 nm, the confinement is small enough such that the inverted band ordering of HgTe is restored and the absolute value of the negative band gap is increasing (see Fig. 3.6).

At a HgTe well width of 8.2 nm, the s-type band drops even below the second confined p-type state. This re-ordering of bands with well thickness is summarized in Table 3.2 and illustrated in Fig. 3.6.

3.3.1 Stoichiometric and Temperature Control of Critical Width

In the previous sections, it has been shown that the effective band gap of the CdTe/HgTe/CdTe quantum well depends on the confinement and consequently on the band gap difference of the well and barrier materials. Both, alloying and temperature

Table 3.2
Orbital character of the top most valence band and lowest conduction band in CdTe-HgTe-CdTe heterostructure depending on the well width d_{QW}. The critical well width d_c is the equal to 6.3 nm.

HgTe Well thickness	Highest Val.Band	Lowest Cond.Band
$d_{QW} < d_C$	p-type	s-type
8.2 nm $> d_{QW} > d_C$	s-type	p-type
$d_{QW} > 8.2$nm	p-type	p-type

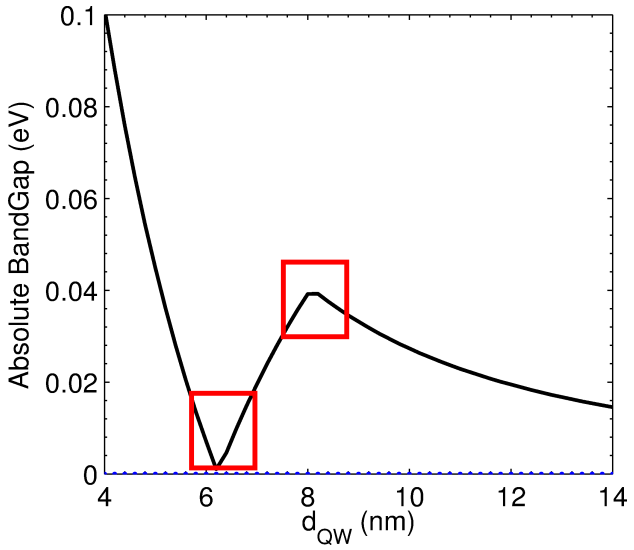

Fig. 3.6. Absolute value of the band gap of a CdTe/HgTe/CdTe quantum well as a function of the well width. Well widths larger than 6.3 nm produce inverted band structures and can be exploited for topological insulator devices.

are known to influence the effective band gap. The band gap of $Cd_xHg_{1-x}Te$ as a function of temperature [66] T and stoichiometry x is given by

$$E_g = -304 + \frac{0.63T^2}{11+T}(1-2x) + 1858x + 54x^2. \tag{3.3}$$

A plot for the band-gap variation for the $Cd_xHg_{1-x}Te$ alloy is given in Fig. 3.7.

When the quantum well material of the original CdTe/HgTe/CdTe structure is substituted by $Cd_xHg_{1-x}Te$ alloy, the critical width becomes temperature and x de-

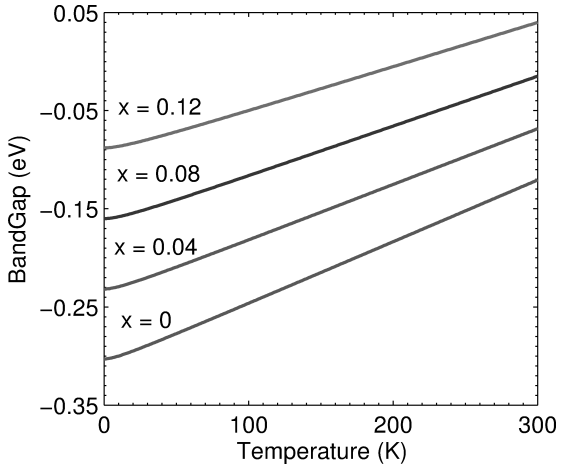

Fig. 3.7. Calculated band gap of bulk $Cd_xHg_{1-x}Te$ as a function of stoichiometry and temperature. At x=0, the bulk band gap of HgTe (-0.303 eV) is reproduced.

pendent. This is shown in Fig. 3.5 (a). Remarkably, all critical widths are equal or larger than the intrinsic critical width of 6.3 nm. Higher concentration of CdTe in the quantum well reduces the Darwin contribution from HgTe. Therefore, the band inversion requires a wider HgTe region.

Alternatively, replacing the barrier material with $Cd_xHg_{1-x}Te$ also allows tuning the confinement and consequently the critical width. It is shown in Fig. 3.7(b) that this replacement yields critical widths smaller then the intrinsic 6.3 nm if the temperature is allowed to attain values below 100 K. For a Cd molar concentration of $x = 0.68$ and $T = 0$ K, the critical width dropped to 4.4 nm. This is due to the enhanced Darwin contribution to the electronic properties with increased Hg content.

3.3.2 Critical widths under different growth conditions

Apart from alloy stoichiometry, the confinement also depends on the well and barrier masses. A way to tune these effective confinement masses is by growing the quantum well in different directions. The different masses then give different effective

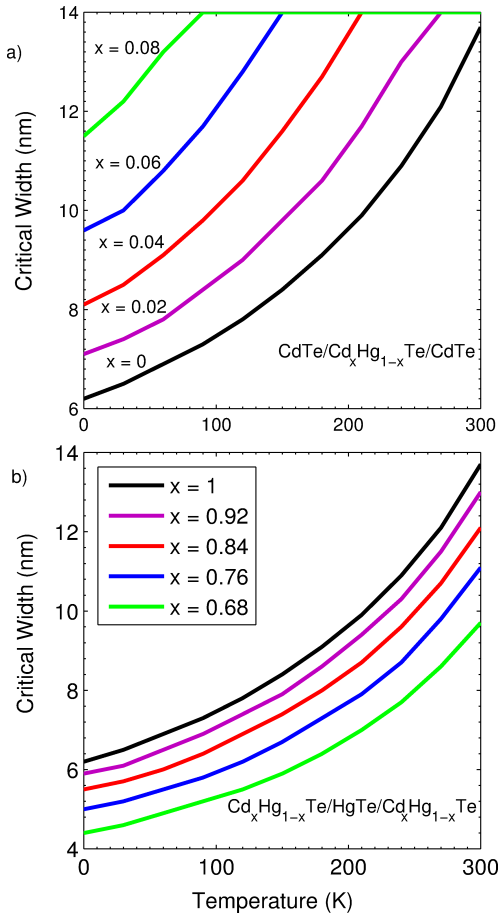

Fig. 3.8. Critical widths to get inverted band structures of $CdTe/Cd_{1-x}Hg_xTe/CdTe$ quantum wells (a) and $Cd_xHg_{1-x}Te/HgTe/Cd_xHg_{1-x}Te$ quantum wells (b) as a function of temperature and stoichiometry x.

well confinement and accordingly different critical widths. This dependence is illustrated in Fig. 3.9. It shows the critical width of the CdTe/HgTe/CdTe quantum well in a sequence of growth directions. The critical widths of the $\langle 111 \rangle$ and $\langle 110 \rangle$ growth directions are 5.52 nm and 5.72 nm respectively. Both these values are smaller than the $\langle 001 \rangle$ grown quantum well critical width of 6.3 nm.

Alternatively, uniaxial stress can also tune the effective confinement masses. As representative cases, CdTe/HgTe/CdTe quantum wells were grown along $\langle 001 \rangle$, $\langle 110 \rangle$,

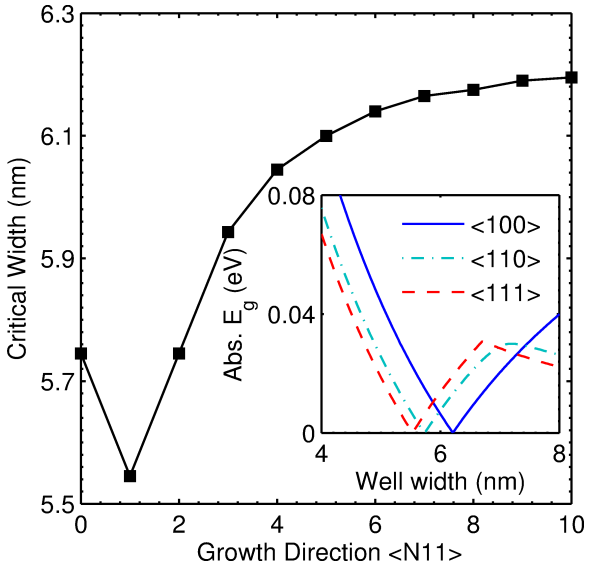

Fig. 3.9. Critical widths of CdTe/HgTe/CdTe heterostructures grown along $\langle N11\rangle$ direction as a function of N (a). The bandgap closing for $\langle 100\rangle$, $\langle 110\rangle$, and $\langle 111\rangle$ grown CdTe/HgTe/CdTe at different well widths is shown in (b). Band gap closing at different well dimensions give the corresponding critical width.

and $\langle 111\rangle$ directions. Each quantum well was then subjected to uniaxial stress along $\langle 001\rangle$, $\langle 110\rangle$, and $\langle 111\rangle$ directions. Uniaxial stress along $\langle 001\rangle$, $\langle 110\rangle$, and $\langle 111\rangle$ was employed on three sets of CdTe/HgTe/CdTe quantum wells grown along $\langle 001\rangle$, $\langle 110\rangle$, and $\langle 111\rangle$. The behaviour of the critical width for each case is shown in Fig. 3.10. The ideal stress orientation for each growth direction is summarized in Tables 3.3 and 3.4.

3.3.3 Application of an external electric field

The application of an external electric field changes the confinement and the band properties of the well states. In particular, the Rashba (structural inversion asymmetry) effect gets enhanced by electric fields in growth direction. [67] Figure 3.11 shows the critical width as function of the external electric field applied in the growth direction. The critical width decays with increasing field for all considered tem-

Table 3.3
The optimal tensile stress and growth conditions for CdTe/HgTe/CdTe quantum wells to achieve the least (L), highest (H) and intermediate (I) critical width, respectively.

	Tensile uniaxial stress		
Growth Axis	⟨001⟩	⟨110⟩	⟨111⟩
⟨001⟩	L	H	I
⟨110⟩	L	H	I
⟨111⟩	H	L	I

Table 3.4
The same list of conditions as in Table 3.3 but under compressive stress.

	Compressive uniaxial stress		
Growth Axis	⟨001⟩	⟨110⟩	⟨111⟩
⟨001⟩	H	L	I
⟨110⟩	H	L	I
⟨111⟩	L	H	I

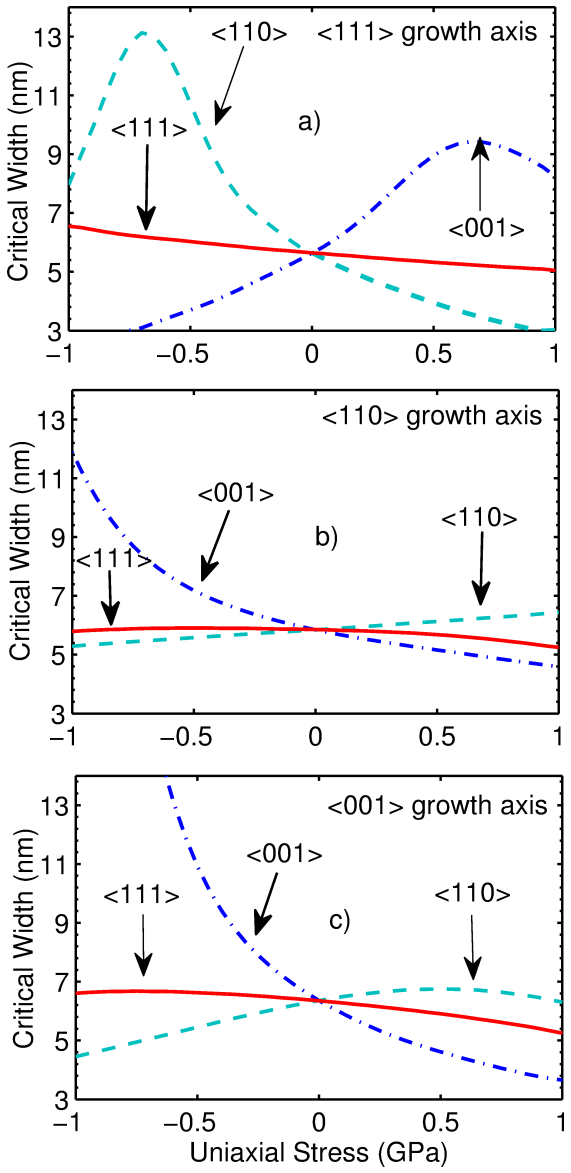

Fig. 3.10. Critical widths of CdTe/HgTe/CdTe heterostructures grown along ⟨111⟩ (a), ⟨110⟩ (b), and ⟨001⟩ (c) direction with uniaxial stress applied along ⟨111⟩ (solid), ⟨110⟩ (dashed) and ⟨001⟩ (dash-dotted) direction. Key observations are summarized in Table 3.3 and table 3.4.

peratures. The Rashba effect that supports the band inversion of HgTe gets increased by the electric field. Consequently, smaller well widths are required to invert

the CdTe/HgTe/CdTe quantum well band structure when external electric fields are present.

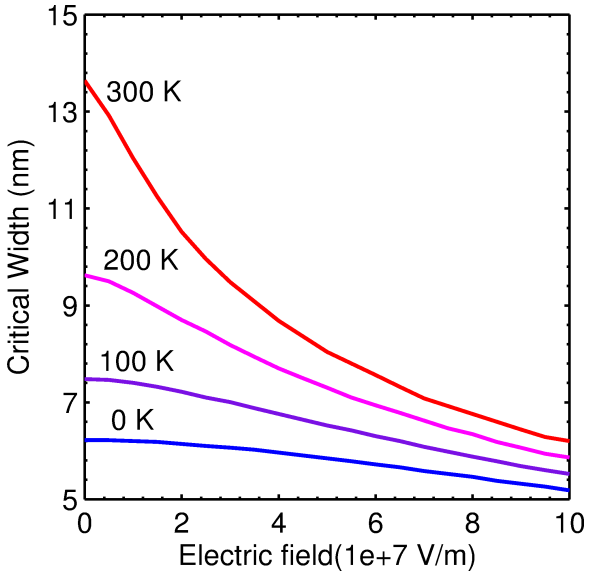

Fig. 3.11. Critical width for CdTe/HgTe/CdTe quantum wells with varying strength of external electric fields in growth direction.

Since external electric fields can tune the critical width, the concept of a TI-switch is obvious: A CdTe/HgTe/CdTe quantum well with a well width that is close, but below the critical width can be switched by electric fields between normal and inverted band order. Such a switching band structure is expected to yield significant changes in the surface conductance, due to the unique transport properties of topological insulator states.

A first prototype of such a switch can be observed in Fig. 3.12 which shows effective band gaps of CdTe/HgTe/CdTe quantum wells for various well thicknesses under externally applied electric fields. Within the plotted range of electric field magnitude, the CdTe/HgTe/CdTe quantum well with a width of 6.0 nm switches between normal and inverted band ordering. It is worth mentioning that this switching behavior can be observed in CdTe/HgTe/CdTe quantum wells grown in $\langle 001 \rangle$ and $\langle 111 \rangle$ direction.

Such topological insulator based devices under an external electric field can be employed to act as a circuit element in a fast digital environment. When the bandgap is closed and TI properties are turned on, a high Fermi velocity for the carriers, (which is an essential attribute of TIs) on surface is able to transmit an electric signal faster than a conventional inter-connect. A seamless transition from a topological insulator to normal insulator using an external electric field as demonstrated above and shown in Fig. 3.12 enables it to forbid an easy passage of charge/electric signal. A normal insulator with a finite band gap will behave as an open circuit element.

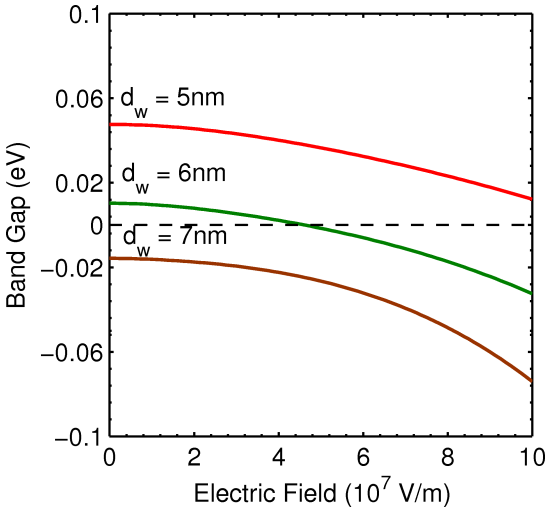

Fig. 3.12. Effective band gap of CdTe/HgTe/CdTe quantum wells of different well thicknesses as a function of applied electric field in growth direction. The dashed line depicts the delimiter between normal and inverted band structures.

3.4 Conclusion

The present work investigates the conditions under which band inversion can occur in a CdTe/HgTe/CdTe quantum well heterostructure. It is shown that this band inversion is essential for topological insulator properties. In agreement with experimental results, it is found that the HgTe quantum well has to be thicker than 6.3 nm to exhibit topological insulator properties. It is examined in detail how the

critical width depends on various device parameters such as the growth direction, alloy stoichiometry, temperature, uniaxial stress, and external electric fields. In particular the external fields allow to switch the topological insulator properties of $\langle 001 \rangle$ grown CdTe/HgTe/CdTe quantum wells. This result proposes a new class of switching devices.

4. NUMERICAL STUDY OF SURFACE STATES OF A TOPOLOGICAL INSULATOR

4.1 Introduction

Bi_2Te_3 and Bi_2Se_3 are well known 3D topological insulators. Films made of these materials exhibit metal-like surface states with a Dirac dispersion. In this chapter the influence of physical and chemical attributes of such films on the the surface-state dispersion is investigated. At low film thickness, the surface states couple to each other to form Dirac hyperbolas and a band gap is opened. Dispersion of these states is also impacted by growth conditions, particularly the substrate. Asymmetric growth conditions are simulated and a Rashba-type splitting of the Dirac cones is observed in agreement with experiment. Low film thickness and asymmetric growth conditions together lead to formation of displaced Dirac-hyperbolas. The surface states are spin-polarized with no out-of-plane component and locked perpendicular to the momentum vector. The spin-polarized components are shown to have unequal strength when asymmetry is present in the film.

4.2 Surface states of 3D topological insulator

Surface states in a 3D topological insulator are characterized by a linear dispersion and a Dirac cone on each surface. The surface states in a 3D TI film depends on the film-thickness, substrate and chemical properties of its surfaces. A film is a quantum well with in-plane periodicity and confined along z-axis. Asymmetric growth condition primarily arising because of a substrate on which the film is grown creates two non-degenerate Dirac cones at the Γ point corresponding to each surface. Further, in the low limit thickness, the surfaces of a 3D-TI couple to each other to open a finite band-

gap. The Dirac cone with massless fermions then change to massive Dirac hyperbolas. Additionally, under a combination of growth asymmetry and thin film conditions, the two Dirac cones give rise to four sets of Dirac hyperbolas.

The surface states of a 3D TI also possess a unique helical characteristics which means that the spin is perpendicularly locked to the momentum. The spin-locking at right angles give rise to fundamentally new phenomena such as the anomalous quantization of magneto-electric coupling, charge fractionalization in a Bose-Einstein condensate, states that are their own antiparticle, which are not possible with conventional Dirac fermions found in graphene-like materials. [68–70] Further, as a consequence of the symmetry of the Hamiltonian, the spin is confined to the plane in a 3D-TI. [71,72] The spin-polarization is computed for both symmetric and asymmetric 3D-TI films. It is found that the two spin components are of different strength, this difference is determined to be a function asymmetry present in the film.

Finally, a Snell's law like refraction condition is derived for transmission of Dirac electrons at the boundary of two 3D topological insulators. The transmitted electrons (equivalent to refraction in optics) suffer a change in momentum when they travel across the boundary. The change in momentum depends on the Fermi-velocities of the two topological insulators. A maximum angle of incidence is derived beyond which the electron beam does not transmit across the boundary and suffers "total internal reflection". The spin being locked to momentum, upon transmission across the boundary changes its in-plane polarization. By appropriately choosing the Fermi velocities in the two TIs, the desired amount of spin-polarization after refraction can be obtained.

4.3 Four-band k.p method for 3D topological insulators

The dispersion of Bi_2Te_3, Bi_2Se_3, and Sb_2Te_3 films are calculated using a 4-band k.p Hamiltonian. The 4-band Hamiltonian [73] is constructed (Eq. 4.1) in terms of the four lowest low-lying states $|P1_z^+ \uparrow\rangle$, $|P2_z^- \uparrow\rangle$, $|P1_z^+ \downarrow\rangle$, and $|P2_z^- \downarrow\rangle$. Additional

warping effects [53] that involve the k^3 term are omitted in this low-energy effective Hamiltonian.

$$H(k) = \epsilon(k) + \begin{pmatrix} M(k) & A_1 k_z & 0 & A_2 k_- \\ A_1 k_z & -M(k) & A_2 k_- & 0 \\ 0 & A_2 k_+ & M(k) & -A_1 k_z \\ A_2 k_+ & 0 & -A_1 k_z & -M(k) \end{pmatrix} \tag{4.1}$$

where $\epsilon(k) = C + D_1 k_z^2 + D_2 k_\perp^2$, $M(k) = M_0 + B_1 k_z^2 + B_2 k_\perp^2$ and $k_\pm = k_x \pm i k_y$. For Bi_2Te_3 and Bi_2Se_3, the relevant parameters are summarized in Table. 5.1.

Table 4.1
4-band k.p parameters [51] for Bi_2Te_3 and Bi_2Se_3.

Parameters	Bi_2Te_3	Bi_2Se_3
M (eV)	3.4	3.2
A_1 (eV Å)	5.6	5.3
A_2 (eV Å)	10.5	10.8
B_1 (eV Å^2)	24.6	22.5
B_2 (eV Å^2)	30.1	28.9
C (eV)	37.8	34.0
D_1 (eV Å^2)	0	0
D_2 (eV Å^2)	0	0

Two variants of a topological insulator film are considered. The first is a free-standing symmetric thin-film of Bi_2Se_3. Two exactly degenerate Dirac cones are formed for a symmetric film. The second thin film considered is assumed to grow on a substrate which induces an asymmetry between the two surfaces. The asymmetry can be explained by assuming that the top surface is exposed to vacuum while the bottom surface is fixed to the substrate. Inversion symmetry therefore does not hold [74, 75]

for such a TI film. This asymmetry is simulated by adding a small symmetry-breaking potential to the Hamiltonian along the confinement direction. It can also be viewed as a simple way of creating two chemically distinct surfaces. The Dirac cones, one on each surface, are therefore no longer degenerate. They are now split as a function of the applied symmetry-breaking potential and positioned at distinct energies. This splitting is similar to a Rashba-split [76] in presence of structural inversion asymmetry (SIA). The asymmetry of the surfaces causes the SIA.

The thin-films considered previously were assumed to be suitably thick to forbid the coupling of the two Dirac cones on each surface. In the limiting case of an ultra-thin film, hybridization of the two surfaces occur. The spin-resolved bands of one surface will mix up with the components of opposite spin from the other surface at a limiting thickness. Since bands with identical quantum numbers cannot cross, a gap opens up at the Dirac point.

When the conditions of ultra-thin film and asymmetry are simultaneously fulfilled, it is observed that the two surface bands offer another instance of Rashba-type splitting. To explain this phenomenon, first a low thickness film is considered. The two degenerate massless Dirac cones in this case would mix and open a finite band-gap as explained above. Each Dirac cone can now be represented as a massive spin-degenerate Dirac hyperbola. [77] If an additional asymmetry is imposed through a potential, the spin degeneracy of each Dirac hyperbola is broken and the bands split along $k_{\|}$ in opposite directions. The degeneracy is only maintained at the Γ point. The conventional Rashba-type splitting follows exactly the same pattern, for example in an asymmetric GaAs quantum well. [78]

A hallmark of the surface bands of a 3D-topological insulator is their intrinsic complete spin-polarization and locking of the spin perpendicular to the momentum. Within the framework of the 4-band k.p Hamiltonian, expectation value of the three spin-polarized vectors is computed. The operators for the three spin-polarizations are given by Eq. 4.2 and Eq. 4.3 in the Pauli representation σ_i $\{i = x, y, z\}$.

$$S_x = \begin{pmatrix} 0 & 0 & 1 & 0 \\ 0 & 0 & 0 & 1 \\ 1 & 0 & 0 & 0 \\ 0 & 1 & 0 & 0 \end{pmatrix}; \qquad S_y = \begin{pmatrix} 0 & 0 & -i & 0 \\ 0 & 0 & 0 & -i \\ i & 0 & 0 & 0 \\ 0 & i & 0 & 0 \end{pmatrix} \tag{4.2}$$

$$S_z = \begin{pmatrix} 1 & 0 & 0 & 0 \\ 0 & 1 & 0 & 1 \\ 0 & 0 & -1 & 0 \\ 0 & 0 & 0 & -1 \end{pmatrix} \tag{4.3}$$

The above matrices are written under the basis set ordered as $|P1_z^+ \uparrow\rangle$, $|P2_z^- \uparrow\rangle$, $|P1_z^+ \downarrow\rangle$, and $|P2_z^- \downarrow\rangle$. The expectation value for each spin-polarization operator is calculated in the usual way in Eq.(4.4)

$$\langle S_i \rangle = \int \psi^* S_i \psi d\tau \tag{4.4}$$

where $\{i = x, y, z\}$

The spin-polarization on the surface of a 3D-TI determined using Eq.(4.2, 4.3, 4.4) serves as the basis of a spin-polarizer. The proposed spin-polarizer is constructed by placing two 3D-TIs together. A sketch of this arrangement is shown in Fig. 4.1. This twin-material spin-polarizer must be designed with two distinct TIs. Alternatively, a single TI can be used but the two sections (Fig. 4.1) must be of different film-thickness. For results presented in this paper, Bi_2Se_3 and Sb_2Te_3 have been selected as the constituent materials. The underlying principle in choosing different materials or the same material with varying thickness is to ensure that Fermi-velocities for the Dirac fermions are different in the two separate material domains. The reason for this choice will be evident in the argument below.

A simple relationship which connects the incident momentum of the electron to that of the transmitted momentum across the junction can be calculated as follows. The electrons that occupy the topological insulator state are Dirac fermions [79] and described by the Dirac equation.

$$H = -iv_f \left[\sigma_x \partial_z - \sigma_y \partial_x\right] \tag{4.5}$$

where v_f is the Fermi-velocity. The Fermi-velocities v_{f1} and v_{f2} in each region are considered to be positive. To set up the problem, it is assumed that the k_1 vector in region I is incident at the interface at an angle θ_1. The wave vector k_1 from region I is transmitted to region II as wave vector k_2 at an angle θ_2. Conservation of energy and momentum yields: $k_1 sin\theta_1 = k_2 sin\theta_2$ and $k_1 v_{f1} = k_2 v_{f2}$. Combining both the conservation relations, the following equation relating the angle of incidence and refraction in each region to their respective Fermi-velocities can be written. The inverse of the Fermi-velocities serve as the quantum mechanical analogue of "refractive indices".

$$v_1 sin\theta_2 = v_2 sin\theta_1 \tag{4.6}$$

The Fermi-velocities are computed numerically by evaluating the expression $\frac{1}{\hbar}\frac{\partial E}{\partial k}$. The energy dispersion is obtained by diagonalizing the 4-band k.p Hamiltonian in (Eq.(4.1)).

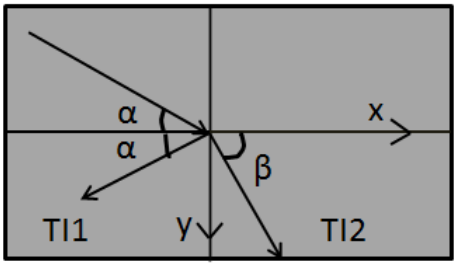

Fig. 4.1. Schematic of the spin-polarizer with two TIs, TI1 and TI2. α and β denote the angle of incidence and refraction respectively.

4.4 Results

In this section, results are derived for several possible situations arising in a topological insulator thin film. The simplest case of a sufficiently thick Bi_2Se_3 film is

first examined followed by the dispersion relationship of an ultra-thin film. Next, asymmetric growth conditions and low-limit thickness results are presented. The spin-density on the surface from the TI states are computed and their dependence on asymmetric growth conditions and an external bias is demonstrated. The optical analogues of "refraction" and "total-internal-reflection" is introduced followed by specific calculations for spin-polarization.

4.4.1 Free-standing symmetric 3D-TI thin films.

The dispersion for a 20.0 nm thick film which is approximately seven quintuple-layers is shown in Fig. 4.2a. The Dirac cone is formed at an energy equal to 0.213 eV confirming that it is indeed a mid-gap state. The bulk band-gap of Bi_2Se_3 is approximately 0.3 eV at the Γ point. In contrast to the thick-film dispersion, Fig. 4.2b shows the band profile of a 3.0 nm (approximately a single quintuple-layer) Bi_2Se_3 film. In the case of a thin-film the two surface states hybridize. The hybridization occurs because each state has a definite localization or penetration length. When the penetration length is in the order of film thickness, the two states mix-up and and a gap is opened. For a low thickness film whose surfaces hybridize, the two branches that split to open up a finite band-gap (Fig. 4.2b) are the Dirac hyperbolas.

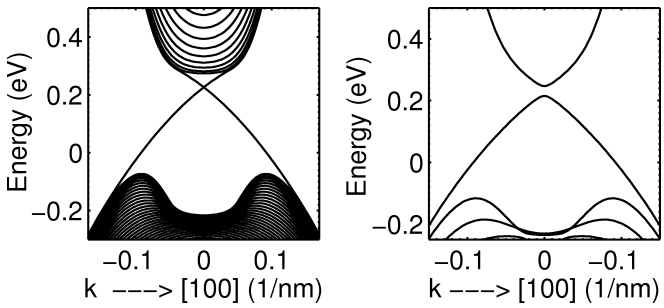

Fig. 4.2. Topological insulator surface states (Fig. 4.2a) around 0.2 eV for a 20.0 nm thick (around 7 quintuple layers) Bi_2Se_3 film. The dispersion of the thin film (Fig. 4.2b) shows two Dirac hyperbolas when the surface states hybridize.

The band-gap which opens up is not a constant but depends on film thickness. In fact the penetration depth can be written as $\xi = \hbar v_f/M$, where M is the bulk band gap and v_f is the Fermi-velocity. The finite band-gap is plotted in Fig. 4.3 for various Bi_2Se_3 film-thickness. The band gap opening is high for thinner films because the penetration of the surface states is maximized and a complete hybridization takes place. The band-gap opening can also be compared between various 3D-TIs. As a numerical example, the band gap opening in a 5.0 nm thin-film is 0.0084 eV and 0.0629 eV in Bi_2Se_3 and Sb_2Te_3 respectively. This difference in band-gap for two dimensionally-identical films can be explained by evaluating the penetration length which is inversely proportional to the bulk band-gap. Sb_2Te_3 has a smaller bulk band-gap at Γ, assuming that Fermi velocities are comparable, the surface states in Sb_2Te_3 are more delocalized than Bi_2Se_3. As a result of greater delocalization, complete hybridization occurs and gives a larger band gap opening.

This band-gap opening can also be thought of as internal magnetization. A magnetic field will destroy time reversal symmetry and create a positive band-gap at the Γ point on the surface. Since an identical effect can be seen for low-thickness thin films, hybridization due to a certain penetration length can be seen as an internal magnetic field.

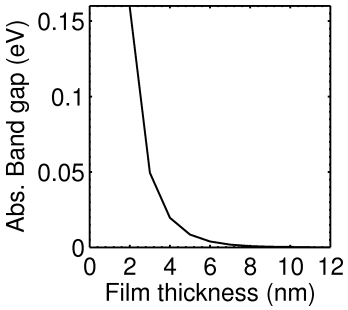

Fig. 4.3. Band-gap opening as a function of Bi_2Se_3 film thickness. Band gap opens because the two surfaces hybridize.

4.4.2 Asymmetric thin films of 3D-TIs

Asymmetry can be created in the thin film by applying an electric field along the confinement direction. This field mimics the asymmetry produced due to two different surfaces or a film grown [80] on a substrate. The substrate provides the asymmetry. An example of a real arrangement of atoms in a Bi_2Te_3 thin film with Bi and tellurium surface termination is shown in Fig. 4.4. Under ideal conditions (ignoring impurity effects), a dipole is formed between the two surfaces which then host a single Dirac cone as shown in Fig. 4.5. The separation of the Dirac cones on each surface depends on the asymmetry induced by the potential.

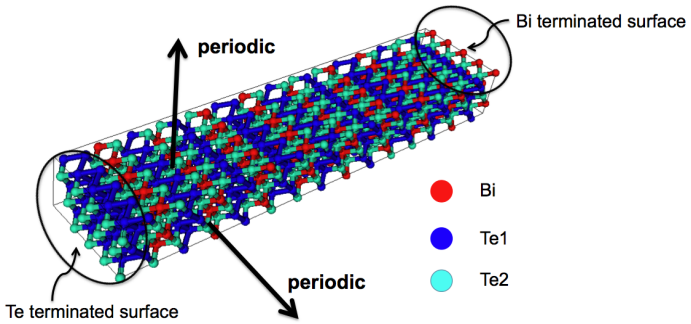

Fig. 4.4. A Bi_2Te_3 thin film with two different surfaces. The two surfaces have Bi and Te termination thus making them chemically inequivalent

A more interesting dispersion relationship arises in the presence of an asymmetric potential in an ultra-thin film. This situation can be broken in to two parts and results obtained above can then be combined. For an ultra-thin film whose surfaces have hybridized, two massive Dirac hyperbolas are created. Each hyperbola is spin-degenerate as shown in Fig. 4.5. If film asymmetry impresses an electrostatic potential breaking inversion symmetry, the two Dirac hyperbolas will now split in to four sets of Dirac hyperbolas (Fig. 4.6). The spin degeneracy of the Dirac-hyperbolas is only maintained at the Γ because it happens to be one of the time-reversal-invariant-momenta (TRIM) points. [38, 81]

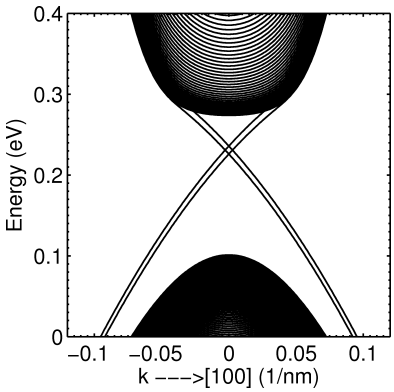

Fig. 4.5. A Bi_2Se_3 thin film with built-in asymmetry. Asymmetry in this film was artificially introduced by using a small potential along the confinement direction. The two Dirac cones are now separated in energy

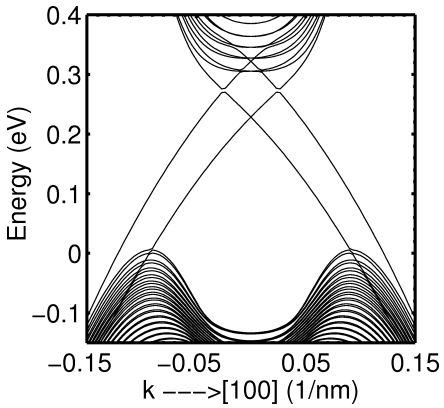

Fig. 4.6. An ultra-thin Bi_2Se_3 film with asymmetry. The two Dirac hyperbolas from the ultra-thin film in presence of asymmetry are now spin-split. They form four copies, two from conduction and valence band and maintain degeneracy only at the Γ point

4.4.3 Spin Polarization of the 3D-TI surface

The spin polarization vector on the surface of a 3D topological insulator is locked to momentum perpendicularly and is confined to the plane. There is no out-of-plane component. Simulations using Eq.(4.2, 4.3) described in Section 4.3 exactly capture this experimental observation. The spin-polarization on the surface of a 20.0 nm thick

Bi_2Se_3 film is shown in Fig. 4.7. For a symmetric free-standing film, the spin-up and spin-down components of the in-plane spin-polarization are exactly anti-parallel.

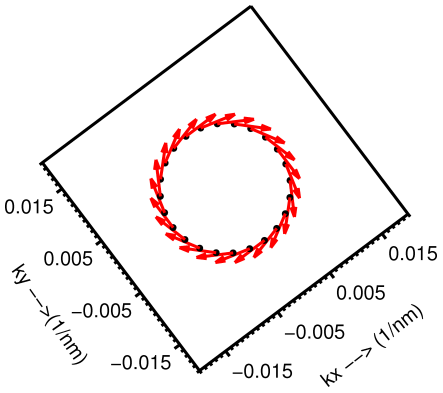

Fig. 4.7. The spin polarization confined to the place in the vicinity of the Γ point for a 3D-TI. The spin is locked to momentum (which is a radial vector on the circle) shown by the tangential lines on the plot.

The spin-polarization shown in Fig. 4.7 was computed by choosing for a k-vector of magnitude 0.01 nm at various polar angles.For each such vector, the spin-polarization obtained was perpendicular with a zero out-of-plane component. The red-arrows in Fig. 4.7 denote the direction of spin-polarization and is always tangential to the circular contour traced out by the k-vector. Interestingly, if spin-polarization is measured in an asymmetric 3D-TI film, the two anti-parallel spin components are no longer of same strength. The amplitude of each spin-component is now a function of the asymmetry expressed as an electric potential. The two surfaces of a 3D-TI therefore have unequal spin-amplitudes.

4.4.4 Spin polarization at interface of two 3D TIs

The arrangement of two 3D-TIs placed together as shown in Fig. 4.2 is considered. Results for this arrangement will draw upon the conclusions presented in the previous sub-sections. The spin was shown to be locked to momentum perpendicularly. Since $k_2 = k_1 \frac{sin\theta_1}{sin\theta_2}$ and using Eq. 4.6, the transmitted wave-vector k_2 and the "angle of re-

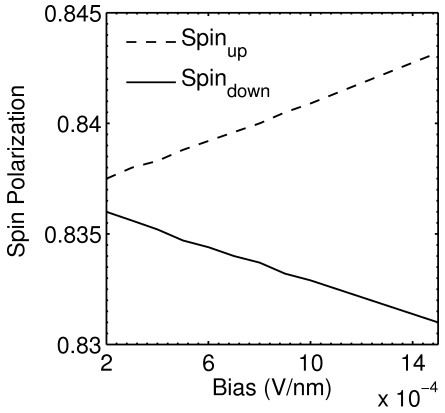

Fig. 4.8. Spin-up and spin-down components are of unequal strength in an asymmetric thin film. The difference in amplitude between the two components increase with higher field/asymmetry.

fraction" of the electron beam can be uniquely determined. For each such "refracted" beam, the spin polarization in region II will change in accord with the helical pattern. By suitably controlling the angle of incidence, the spin polarization in region II can be tuned as desired.

A concrete example is now presented that illustrates the above method. Bi_2Se_3(region I) and Sb_2Te_3 (region II) films of thickness 100.0 nm are selected as the two 3D-TIs for regions I and II respectively. Using the Hamiltonian in Eq. 4.1, the dispersion relationship is computed. The Fermi-velocities extracted from the dispersion relationships for Bi_2Se_3 and Sb_2Te_3 films yield $v_{Bi_2Se_3} = 2.721 \times 10^6$ m/s and $v_{Sb_2Te_3} = 4.081 \times 10^6$ m/s respectively. Both the films have been assumed to be symmetric and free-standing. An electron beam from region I is incident at an angle $\theta_i = \pi/6$. The magnitude of $|k_I|$ vector is set to 0.01 nm^{-1}. This beam, after suffering refraction at the interface will change magnitude and continue to region II. The new magnitude would be equal to $|k_{II}| = 0.0066$ nm^{-1} making an angle $\theta_2 = 48.6°$.

The spin polarization in region I is given by $\beta_{spin_I} = tan^{-1}(S_y/S_x)$ where the spin polarization vector $S = \begin{pmatrix} S_x \\ S_y \end{pmatrix}$. For the numbers chosen, β_{spin_I} evaluates to 118.41°. The corresponding spin polarization in region II is equal to 72.59°. Therefore by

choosing the correct $|k|$ vector and the angle of incidence, the final spin polarization in region II can be predicted. Looking at it the other way, for a desired final spin polarization, the input parameters in region I can be uniquely determined.

It is noteworthy here to point out that an effect similar to the "total internal reflection" in optics can be observed. The relation described in Eq. 4.6 suggests that the beam of electrons from TI region I can continue to TI region II only when the following condition holds.

$$0 \leq \frac{v_2}{v_1} sin\theta_1 \leq 1 \tag{4.7}$$

where v_1 and v_2 are the two Fermi-velocities. Using the pre-computed values of v_1 and v_2, an upper bound for θ_1 can be deduced. For the specific case considered here, v_1 and v_2 are equal to 2.721×10^6 m/s and 4.081×10^6 m/s respectively. The angle of incidence θ_1 therefore has an upper-limit set to 41.81°. For any angle of incidence $\theta_1 > 41.81°$, the electron beam will suffer "total internal reflection" and not pass to region II. All important "observables" and input parameters are collected in Table 5.2

Table 4.2
Observables and input-parameters for the spin-polarizer shown in Fig. 4.1

Observables	Bi_2Se_3	Sb_2Te_3
θ_1	30°	-
θ_2	-	48.6°
$\|k\|$ vector	0.01 nm^{-1}	0.0067 nm^{-1}
Spin pol.	0.8367	0.6309
Polz. angle	120°	138.59°
Tot. Internal. Refl.	41.81°	-

In constructing this table, the magnitude of the incident $|k|$ vector and the angle of incidence was set to 0.01 nm^{-1} and $\pi/6$ respectively. The table can be filled for

different $|k|$ vectors and the angle of incidences by using the momentum and energy conservation relation described in Section 4.3.

4.5 Conclusion

This work utilised thin-films of 3D-topological insulators to demonstrate the influence of thickness, growth conditions on the nature of the topologically protected surface states. Films in the limit of the low-level thickness have their surfaces hybridized and opens up a band-gap and the Dirac cone changes to a Dirac hyperbola. Further, films grown on a substrate or with chemically distinct surfaces produce two Dirac cones which are separated in energy. When conditions of substrate or surface asymmetry are combined, the Dirac cones change in to four sets of Dirac hyperbolas. The spin which is polarized and locked to momentum giving a helical character to the surface states were examined for both free-standing and asymmetric films. The spin-polarization was found to be different for the two orientations; one of the spin projection gains strength in the presence of a symmetry-breaking potential. Finally the spin polarization at the interface of two 3D-topological insulators is worked out. A Snell's like-law for Dirac electrons was derived to determine the electron momentum after it crosses the first region. The spin-polarization in the second topological insulator region can be controlled by choosing the correct angle of incidence and a choice of $|k|$-vector.

5. THE ELECTRON-CORE MODEL

5.1 Introduction

Many modern semiconductor devices and materials yield band structures that do not allow a distinction between electrons and holes. Primary examples of such devices and materials are broken-gap super-lattices and topological insulators. This work introduces the concept of a novel charge self-consistent full-band atomistic tight binding method that avoids usage of holes. The key idea of this method is to consider every eigen state as an electronic state and superimpose a positive bed of charges to maintain overall charge neutrality. The ion charge is determined by solving the Schrödinger equation of the bulk material. To demonstrate this method, the charge self-consistent band structure of a 9.0 nm thick Bi_2Te_3 layer is calculated. This method is also applicable for transport calculations in band to band tunneling structures and broken gap devices.

5.2 Why topological insulators need another model?

Standard semiconductor devices and materials are electronically represented through a dispersion relationship. The dispersion relationship assumes that the semiconductor has well-defined regions for electrons (conduction band) and holes (valence band). The conduction states are energetically higher than valence bands and separated by a finite positive energy gap. Recently, several devices and materials that have generated considerable interest due to their unique electronic properties do not possess the positive-energy separated conduction and valence bands. Primary examples of such devices and materials are the broken-gap super-lattices [82, 83], tunnel FETs [84, 85], and the newly discovered topological insulators. The GaSb-InAs heterostructure is

an example of a broken-gap device because the lowest conduction band edge in InAs falls energetically below the highest valence band edge of GaSb.Similarly, topological insulators (TIs) have a cone of states on the surface that connect the conduction and valence bands together.

The bulk bands in broken-gap devices and surface bands in TIs, therefore cannot have their conduction and valence bands unambiguously defined. Since the accurate prediction of device characteristics and material properties needs charge self-consistent calculations, it is imperative to devise electronic structure calculation models for materials where an explicit differentiation between electrons and holes is not possible. Traditional methods therefore need substantial modification to address this issue.

In this regard, several approaches to handle devices and materials where a unique distinction between electrons and holes is not possible have been put forward. These approaches primarily rely on effective-mass calculations [86] or use an eight-band k.p Hamiltonian [87]. In these models it was tacitly assumed that electrons and holes are distinguishable. A charge self-consistent k.p envelope-function method that avoids the concept of holes [88] was developed and applied to a GaSb-InAs superlattice to compute energy-gaps, effective masses, optical-transition energies etc. This work continues the concept of Ref. 88 and introduces a charge self-consistent full-band atomistic tight binding method that avoids usage of holes. This method is also applicable to transport calculations in band to band tunneling structures and broken gap devices. This method is applied to a 9.0 nm thick Bi_2Te_3 film with both identical and inequivalent surface termination.

5.3 Charge self-consistent tight binding model

In this section, a new method, needed to accurately model broken-gap devices and topological insulators within an atomistic framework is introduced. This description is based on a coupled Schrödinger-Poisson charge self-consistent scheme. The

Schrödinger equation is set-up within a twenty-band $sp^3d^5s^*$ basis set. In a traditional self-consistent calculation, the total charge density is split as a contribution from electrons and holes (Eq. 5.1). Eigenstates of the Schrödinger equation close to the Fermi-level are occupied by electrons and holes according to the Fermi-Dirac function. In the case of a heterojunction with laterally Bloch periodic boundary conditions, the total space charge at any lattice site x is given as

$$\rho_{traditional}(x) = \int_{\Omega_{BZ}} \mathrm{d}^2 k_{||} \left\{ \sum |\Psi_{n,k}|^2 \left[1 - f\left(E_{n,k}\right)\right] - \sum |\Psi_{n,k}|^2 f\left(E_{n,k}\right) \right\}, \tag{5.1}$$

In contrast to the traditional approach, in the proposed method every eigen state of the full band tight binding Schrödinger equation is considered as an electronic state, independent of its occurrence either in the valence or conduction band. In equilibrium, the states are filled by a single Fermi distribution. In addition, a positive charge (ρ_{core}) is assumed for every tight binding lattice site, i.e. for every ion core (Eq. 5.2). It is important to clarify that the positive charges do not form a continuous distribution, rather they are discretely arranged corresponding exactly to the atomic description of the device under consideration. The total space charge at a lattice site x is therefore given as

$$\rho_{electon-core}(x) = -\int_{\Omega_{BZ}} \mathrm{d}^2 k_{||} \sum |\Psi_{n,k}|^2 f\left(E_{n,k}\right) + \rho_{core}\left(x\right). \tag{5.2}$$

The first step in this method is to compute the positive charges accurately. In order to do so, every material's atom is considered a positive ion charge that depends on the specific tight-binding model and the corresponding material parametrization. The Schrödinger equation of the bulk material is solved to compute a quantum mechanical electron density on each atom. The electron density on every atom is defined as the product of the squared absolute value of the eigen state amplitude and its occupancy probability. The resulting atom-resolved electron density is assumed to agree precisely with the positive ion charge density. This guarantees that the charge self-consistent bulk band structure is in complete agreement with the empirically determined parametrization. It is tacitly assumed that the positive ion charge density

determined from a bulk Hamiltonian holds well for confined devices made out of the same material.

Table. 5.1 below shows a representative calculation for GaAs. Ga and As atoms represent the positive ion charges in this case. Two tight-binding models [89,90]($sp^3d^5s^*$ and sp^3s^*) are considered. As a further check, the results are compared to a DFT calculation. While performing the DFT calculation, it is assumed that a point within the unit cell of GaAs crystal belonged either to Ga or As depending upon their relative closeness to the atom. A point in real-space of the GaAs unit cell closer - for example - to Ga, was assumed to carry charge that contributed to the eventual electron density of Ga.

Table 5.1
Two different bulk charge calculation method is shown. Using DFT and $sp^3d^5s^*$ and sp^3s^* models the charge on cation and anion is computed. Note that the sum of charges is always equal to eight since three and five valence electrons from Ga and As respectively participate in the bonding.

Charge determination methodology	Charge on each atom		
	Gallium	Arsenic	
DFT	3.4865	4.5135	
sp^3s^*	2.765	5.234	
$sp^3d^5s^*$	3.297	4.702	

To apply this method to a confined device, the corresponding tight-binding Hamiltonian is constructed and diagonalized for eigen states. The quantum mechanical electron charge is computed using Eq.(5.3) where symbols have their usual meaning.

$$n(z) = \sum_{i=1}^{N} \frac{1}{(2\pi)^2} d^2k_{||} \sum |\Psi_{n,k}|^2 f(E_{n,k}) \tag{5.3}$$

The key point here is that in bulk the total charge density per atom is zero since it is explicitly assumed that the quantum mechanical electron density is counter-

balanced by an equal positive ion density. But each atomic node of a device (which is different from bulk configuration) which is supposed to hold positive charge density equal to bulk will not have an exact amount of electron density to counter-balance. An excess charge density will therefore accumulate. The total excess charge density on every atom node in a heterostructure is then a sum of atomically resolved electron densities and the material dependent ion charges (Eq. 5.4). The excess charge density which gives only a perturbative potential can be calculated using Eq.(5.4). Unlike a realistic device/heterostructure, in bulk all electrostatic effects are covered by the empirical tight-binding parameters. This is explained by noting that the magnitude of the quantum mechanical electron density is a direct outcome of the chosen tight-binding parameters. Further, the positive charge density assigned to each node is equal to the quantum mechanical electron density.

$$\rho_{excess} = q\left[-n(z) + \rho_{bg}(z)\right] \tag{5.4}$$

The excess space charge is used to determine the electrostatic potential via Poisson equation (Eq. **??**). Since all fully occupied electronic states of the tight binding electron representation are explicitly included in the calculation, electrostatic screening effects of even deeper lying electrons are ignored and the dielectric constant in the Poisson equation is assumed to be equal to unity. [91]

A dielectric constant, which essentially signifies the response of the electrons to an external electrostatic perturbation is therefore redundant in this method. In a traditional approach where few states around the Fermi-level are considered, the response of the core electrons is included through the dielectric constant. Any value for the dielectric constant in the current method (which considers all core and valence electrons), that is different from unity, would entail that the response/screening effects of core electrons is counted twice in the electrostatic calculations.

It is important to note that within an eight-band k.p approach as demonstrated in Ref. 88, the dielectric constant cannot be set to unity. The eight-band k.p Hamiltonian calculates the eigen spectrum using a limited basis set around a high-symmetry point.

The response of all the electrons can therefore not be accounted for in a self-consistent charge calculation. A position dependent dielectric constant is used. Tight-binding based methods, on the other hand, span the whole Brillouin zone and all eigen states are included in calculations allowing the dielectric constant to be set to unity.

In these calculations, it is assumed that the core ions are rigid and do not move from their positions. In actual microscopic world, the atomic displacements of the core ions marginally contribute to the electrostatic response of the system.

5.4 Results

The method outlined in the previous section is applied to Bi_2Te_3 quantum wells(thin film). Bi_2Te_3 is a narrow band-gap semiconductor (Fig. 5.3) with interesting surface properties.

On its surface, the bulk band-gap is closed by Dirac fermion-like states(Fig. 5.1) that are robust to non-magnetic perturbations. Such states, cannot be classified definitely as electrons or holes. The proposed method therefore seeks to model these states without attributing a particular electron or hole character to them. A thin film modeled by this method is shown in Fig. 5.2. This film has inequivalent surface terminations. The surfaces were chosen to terminate with Bi and Te1 atoms.

In Section 5.4, a positive background ion charge was calculated that helped in restoring charge neutrality. GaAs was used as a test case and such background ion charges were computed (Table. 5.1). By following the same approach, core ion charges for Bi_2Te_3, based on an $sp^3d^5s^*$ tight-binding parameter set [52] are collected in Table. 5.2. Bi_2Te_3 has three different atoms in its rhombohedral crystal structure [92]. These positive ion charges will be applied as a background charge to the atomic nodes of the thin film.

A self-consistent calculation is carried out which yields the charge profile and potential landscape for two thin films that differ in their surface termination. When a thin film has different surface atom arrangements (similar to Fig. 5.2), a spatially-

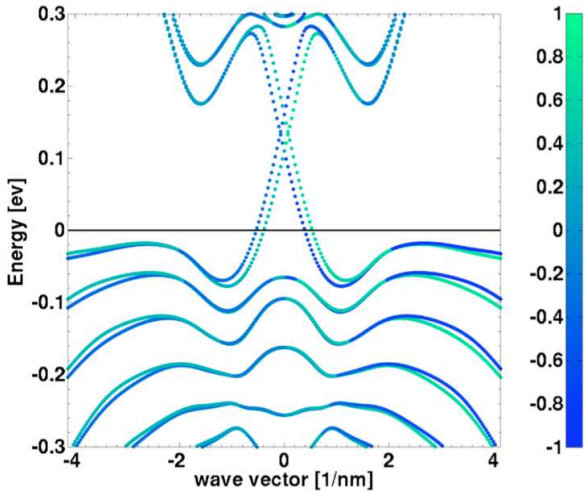

Fig. 5.1. The surface states of a topological insulator. The conduction and valence bands are connected together by a cone of states at the Γ point. The meeting of the conduction and valence bands is usually a linear dispersion also known as a Dirac cone

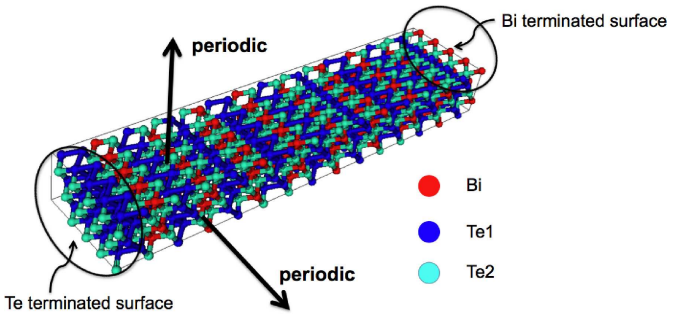

Fig. 5.2. The target structure for applying the all-electron model. It is a 9.0 nm thick Bi_2Te_3 ultra-thin body oriented along the x-axis.The two surfaces have Bi and Te termination thus making them chemically inequivalent

dependent electrostatic potential (Fig. 5.4a) is obtained and the charge on each atomic node (Fig. 5.4b) is oscillatory. This oscillatory pattern is common to tight-binding calculations. Moreover, this structure gives rise to an intrinsic dipole moment represented through a change in polarity of charge at the two surfaces. The bismuth terminated surface has a charge roughly equal to 0.25(e). Te1 surface changes polarity and the charge is computed to be -0.15(e).

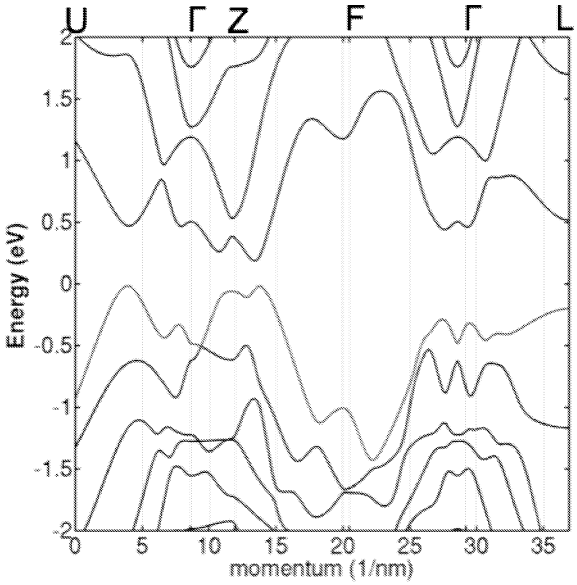

Fig. 5.3. Bulk band structure of Bi_2Te_3 according to parameterization of Ref. 52 .

Table 5.2
Background positive ion charges for Bi_2Te_3. These charges have been calculated using a $sp^3d^5s^*$ tight-binding model

Atom type	Positive ion charge(e)
Bi	3.89882
Te1	6.52157
Te2	7.15921

The thin film with identical surfaces (both surfaces are Te1 terminated) has a much smoother and symmetric potential and charge distribution about the centre of the device along x-axis (which is the direction of confinement) as shown in Fig. 5.5a and Fig. 5.5b respectively. Both the Te1 surfaces have a charge of around 0.25(e). The symmetric potential landscape corresponding to this charge ensures that there is no dipole moment unlike the thin film with Bi and Te1 termination. Nevertheless, the electrostatic potential obtained through these self-consistent calculations for both the thin films can be considered as a smooth perturbation. This perturbation is

essentially a correction to the electron-electron interaction already covered by the empirical tight-binding parameters for a bulk calculation.

An interesting feature when the termination is bismuth and tellurium compared to an all-tellurium terminated device is the charge distribution in the volume of the device. When there is inequivalent termination, a finite spatially-dependent potential is present in the structure. To maintain charge neutrality under the influence of this potential, the atomic core charges fluctuate with opposite polarity. This is the origin of the spikes in the charge distribution. Each spike with a certain polarity is the net charge on a cation or anion.

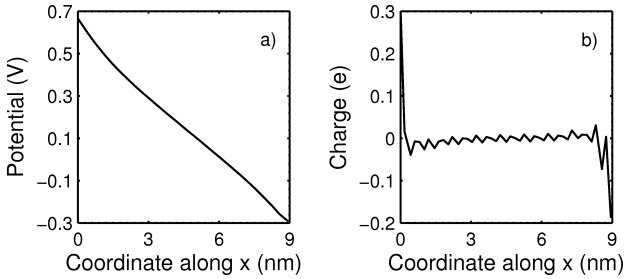

Fig. 5.4. The spatially-dependent electrostatic potential (Fig. 5.4a) and charge on each atomic node is plotted against the x coordinate of the Bi_2Te_3 thin film. This thin-film has Bi and Te termination on the surfaces. An oscillating charge pattern (Fig. 5.4b) is obtained for inequivalent surface termination.

The all-tellurium device in contrast has a smooth charge profile with no electrostatic potential in the bulk. The only finite potential is at the edge of the device. It was postulated in Sec. that the present model uses a positive charge background that completely neutralises the electron density on each atom. The all-tellurium device therefore has approximately zero charge on each cation and anion in the presence of a zero potential. The charge only accumulates at the edge in direct correspondence to the finite potential there.

When the thin film is confined along the z-axis, a constant charge is obtained throughout the film except at the boundaries (Fig. 5.6a). The potential profile is completely flat and constant (Fig. 5.6b). For the film considered, the potential was

determined to be 0.079 V. This lack of asymmetry in charge and potential profile compared to those obtained from confinement along the x-axis is an attribute of the layered structure of Bi_2Te_3. Bi_2Te_3 possesses a hexagonal symmetry in the x-y plane. Such hexagonal planes are stacked along the $< 111 >$ direction to give it the layered structure. When confinement is along the x-axis, the hexagonal symmetry is disturbed. This loss of symmetry generates an intrinsic dipole moment which manifests as an electrostatic potential which is more pronounced when the surfaces are distinct due to inequivalent atomic termination. In the other case considered, confinement along z-axis preserves the x-y in-plane symmetry. Charges of oppsoite polarity build-up at the two edges similar to a parallel plate capacitor. In a direct analogy to a parallel-plate capacitor, in the volume of the device the electrostatic potential is position-independent.

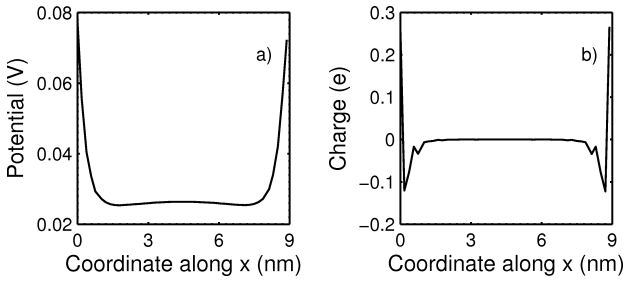

Fig. 5.5. The electrostatic potential and charge is now plotted against the x-coordinate of the device. The device is again a Bi_2Te_3 thin film but with tellurium termination on both surfaces. The potential and charge is constant in the volume of the device.

By using the potential determined in Fig. 5.4a for the thin film with different surfaces, the twenty-band tight-binding Schrödinger equation is solved to yield a spin resolved self-consistent band structure. The colours in the dispersion plot (Fig. 5.7) depict the spin polarized surface bands typical of topological insulators. The Dirac-cones correspond to the topologically protected states on the two surfaces. The Dirac-cones are shifted in energy due to the inequivalent surfaces chosen for the Bi_2Te_3 thin film. They are hence positioned at different points for each distinct surface

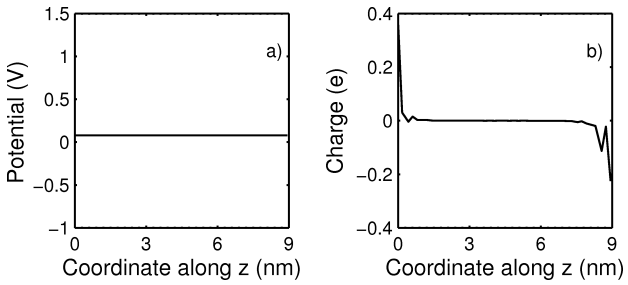

Fig. 5.6. The charge and potential profile (Fig. 5.6a) for a thin-film confined along the z-axis. The potential is of constant magnitude while the charge changes value only the edge of the device. The charge in the volume of the device is zero (Fig. 5.6b)

on the energy scale. The spin-polarization is along the x-axis which is in accord with experimentally observed result. The spin of the electrons in the vicinity of the topologically protected state has been verified to be completely in-plane with zero out of plane component. [93]. The self-consistently calculated bandstructure when compared to the simple tight-binding result (Fig. 5.1) shows that the Dirac cones have shifted down in energy. This shift in energy demonstrates that a self-consistent calculation is necessary for accurate determination of the surface bands in a Bi_2Te_3 thin film topological insulator.

This asymmetry is also reflected in the self-consistent band structure plotted for the two thin films with confinement along the x(Fig. 5.7a) and z-axis(Fig. 5.7b). The band structure for the x-axis confined film does not possess the symmetry of its z-axis counterpart. These plots are therefore in agreement with the electrostatic results discussed above. The band structures are computed by using standard 20-band $sp^3d^5s^*$ tight-binding. Two key observations can be made about the dispersion plots for two different directions of thin-film confinement. 1) The energy separation between Dirac cones get enhanced. 2)The band curvatures change which mean that the Fermi velocity of Dirac states are different. This has a direct impact on mobility of the surface states. Dirac points now also move below the Fermi level in to the bulk DOS.

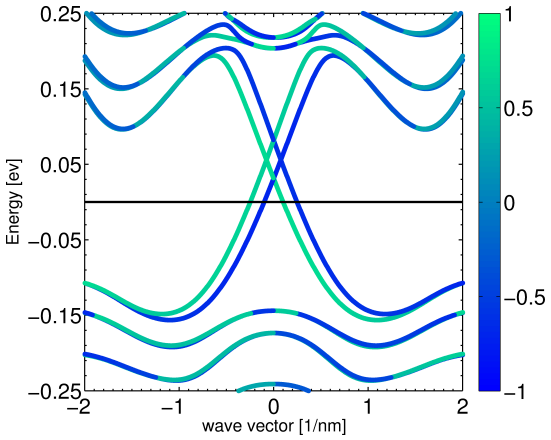

Fig. 5.7. The charge self-consistent, twenty-band tight-binding electronic dispersion for a Bi_2Te_3 thin film with Bi and Te1 surfaces is shown here. The Dirac cones are separated in momentum-space. The colour bar indicates the intensity of spin polarization of the TI surface bands.

5.5 Conclusion

A charge self-consistent tight-binding method is developed targeted towards broken-gap devices and super-lattices. Topological insulators that exhibit similar ambiguity as broken-gap devices as regards to distinction of electrons and holes are therefore ideal candidates for application of this method. Standard approaches to compute the dispersion of broken-gap devices are inadequate since they make an explicit demarcation between electrons and holes. The proposed method seeks to correct this problem by assuming that all states are filled with electrons against a positively charged background. The positively charged background is essential to fulfill the condition of charge neutrality. A self-consistent Schrödinger-Poisson is needed to obtain the accurate dispersion relation. While the method is attractive to deal with the traditional broken-gap devices and the newly discovered topological insulators, it is much more computationally demanding. In the traditional method, only a small set of states around the Fermi-level are chosen. The filled valence states are not included in the actual calculation. In contrast, the suggested tight-binding based electronic structure

calculation technique accounts for all filled states in a charge self-consistent calculation. The downside of this method is the requirement of a large number of states to fill with electrons. It is therefore, a more demanding and computationally expensive method.

6. TOPOLOGICAL INSULATOR WITH WURTZITE-BASED NITRIDES

6.1 Introduction

The surface states of a topological insulators is the direct outcome of band inversion. The inversion of band in the bulk is primarily due to spin-orbit coupling. Compounds of heavy elements such as Hg, Bi which possess significant spin-orbit coupling are well-known topological insulators. This chapter looks at another class of materials that despite nominal spin-orbit coupling also exhibits topological insulator states. In Chapter 2, the GaSb/InAs heterostructure [35] was briefly touched upon. The peculiar band alignment of the conduction and valence band edges in that heterostructure leads to band inversion. Wurtzite based nitrides which have a strong spontaneous polarization can also have inverted band states under appropriate conditions. These conditions, suitable materials, and quantum structures are discussed in this chapter. To begin, a brief description of the wurtzite crystal structure and the intrinsic spontaneous polarization is included followed by detailed electronic structure calculations that show how a TI state can be formed.

6.2 The wurtzite crystal

The wurtzite unit cell is show in Fig. 6.1. It consists of two inter-penetrating hcp lattices. The sites marked as A and B can be occupied by X or nitrogen atom. Here X denotes either Ga, Al, or In atom. The nitrogen atom at A or B is internally displaced by a distance u. The strong electro-negativity difference between X and N atoms coupled with its small size results in the electron cloud in the metal-nitrogen bond preferentially shifted towards the nitrogen atom. Each metal-nitrogen bond

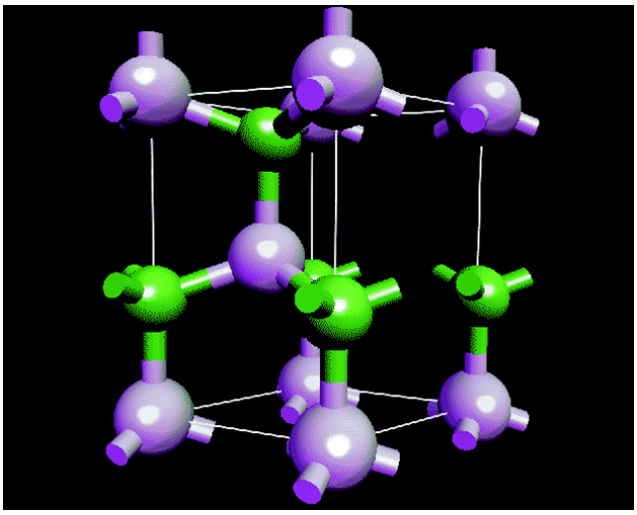

Fig. 6.1. Unit cell of the wurtzite crystal. The primitive unit cell contains four atoms.

in a tetrahedral arrangement therefore creates a dipole moment which in a perfect wurtzite crystal vectorially sums to zero. A perfect wurtzite crystal has an internal u parameter equal to $(\frac{8}{3})^{0.5}$. Almost every crystal deviates from this number and a resultant dipole moment along the c-axis which coincides with [0001] direction exists. A sketch of this uncompensated internal dipole moment is shown in Fig. 6.2.

6.3 Internal polarization and topological insulators

In addition to spontaneous polarization, piezoelectric polarization which arises in a strained system contributes to the total internal electric field. The task, therefore is to derive ways to facilitate band inversion with this internal electric field. A common trait of compounds with band inversion is a narrow band gap. In the wurtzite class of compounds discussed here, InN with an approximate band-gap of 0.68 eV can be a possible candidate for inverted band order due to internal polarization. It is important to note here that spontaneous polarization is a material parameter cannot be altered but piezoelectric polarization which is strain dependent can be tuned assuming psuedomorphic deformation. For example, an InN film grown on a GaN substrate

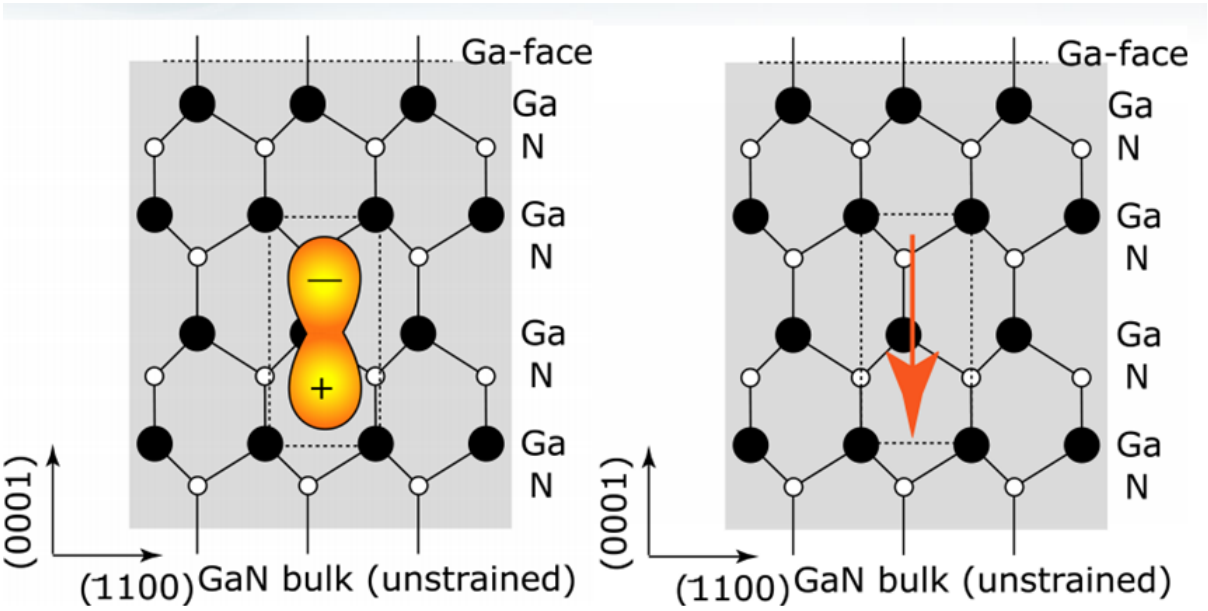

Fig. 6.2. Spontaneous polarization due to crystal asymmetry in wurtzite lattice [94].

can be biaxially strained to create piezoelectric field in InN. To quantitatively establish band inversion, the electric field must be computed. A sketch of a such a system with InN well and GaN barrier is shown in Fig. 6.3.

6.4 Calculating the spontaneous and piezoelectric fields

The quantitative calculation of the electric field in the GaN/InN/GaN heterostructure can be deduced from the following relations. The first set of equations give the internal electric field. $\overrightarrow{E}$ denotes the electric field, ϵ_i is the dielectric constant

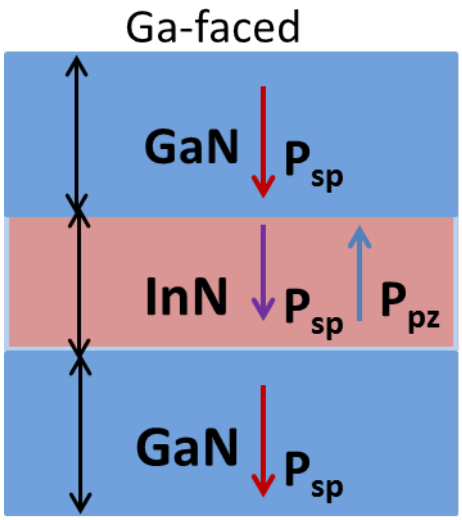

Fig. 6.3. Schematic of the GaN/InN/GaN heterostructure with dimensions of the well(InN) and barrier(GaN) regions. The direction of the arrows point to the effective piezoelectric and spontaneous polarization present in the heterostructure.

in a certain region of the heterostructure and σ_i stands for bound surface charge density(C/m^2). These equations follow directly from Gauss law.

$$\epsilon_1 E_1 = \sigma_1 \tag{6.1a}$$

$$\epsilon_2 E_2 - \epsilon_1 E_1 = \sigma_2 \tag{6.1b}$$

$$\epsilon_3 E_3 - \epsilon_2 E_2 = \sigma_3 \tag{6.1c}$$

The charge at each interface can be computed from the set of equations below

$$\sigma_1 = \sigma_{sp}(GaN) \tag{6.2a}$$

$$\sigma_2 = -\sigma_{sp}(GaN) + \sigma_{sp}(GaN) + \sigma_{pz} \tag{6.2b}$$

$$\sigma_3 = -\epsilon_2 \tag{6.2c}$$

$$\sigma_4 = -\epsilon_1 \tag{6.2d}$$

The potential drop (Fig. 6.4) over the InN 3.0 nm wide well is considerably large. This potential must now be added to the Hamiltonian to check if indeed a band

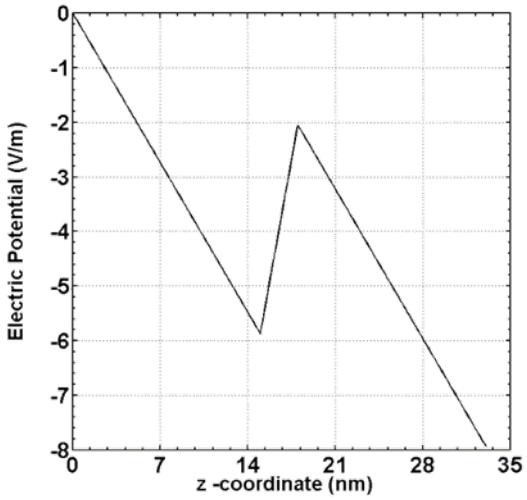

Fig. 6.4. The potential drop of 3.827 V over the quantum well. GaN and InN are lattice mis-matched by 11 % and strongly contributes to the internal field. GaN was assumed to be relaxed and InN was biaxially strained. The spontaneous polarization of both GaN (-0.034 C/m^2) and InN (-0.029 C/m^2) are evenly matched and is a weak contributor.

inversion can occur. A schematic of this polarization field aided band inversion is shown in Fig. 6.5.

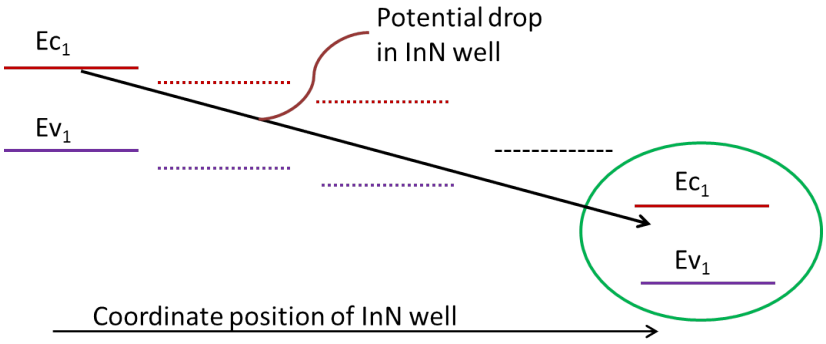

Fig. 6.5. Schematic of the GaN/InN/GaN broken-gap heterostructure. The encircled region shows the part of the InN quantum well where the conduction band edge falls below the valence band edge. The potential drop similar to a p-n junction induces the bending of the conduction and valence band edge.

6.5 Eight-band k.p Hamiltonian for wurtzite

The final Hamiltonian can then be written as:

$$H = H_{8\times8} + V_{sp+pz} + H_{strain} \tag{6.3}$$

In Eq. (6.3), the total Hamiltonian is a sum of the 8-band k.p Hamiltonian for wurtzite [95, 96], the electrostatic potential obtained using Eq. (6.1) and Eq. (6.2) and the strain Hamiltonian. The strain Hamiltonian [97] is computed using the Bir-Pikus deformation potential theory. The band profile of a GaN/InN/GaN quantum well heterostructure is first computed (Fig. 6.6. The width of the InN quantum well is set to 3.0 nm. In a normal ordered wurtzite material, the Γ_1 symmetry point is energetically placed over Γ_6. For the band structure shown in Fig. 6.6, the sequence is just reversed demonstrating the inverted band profile. Band-gap closing edge states

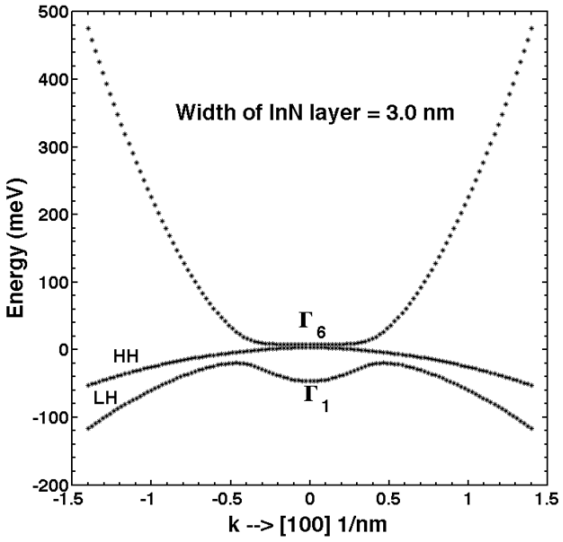

Fig. 6.6. Band structure of the GaN/InN/GaN broken-gap heterostructure. The symmetry of the orbitals at the Γ point is reversed.

which are Dirac-cones (Fig. 6.7 must therefore be found when a nano-ribbon is constructed from the inverted quantum well by quantizing one of its in-plane periodic axis. The edge states are also determined to be spin-polarized indicated by the two

different colours of bands. The nano-ribbon is chosen to be 100.0 nm wide to prevent mixing of the edge states. Additionally, the wave functions of the two edge states

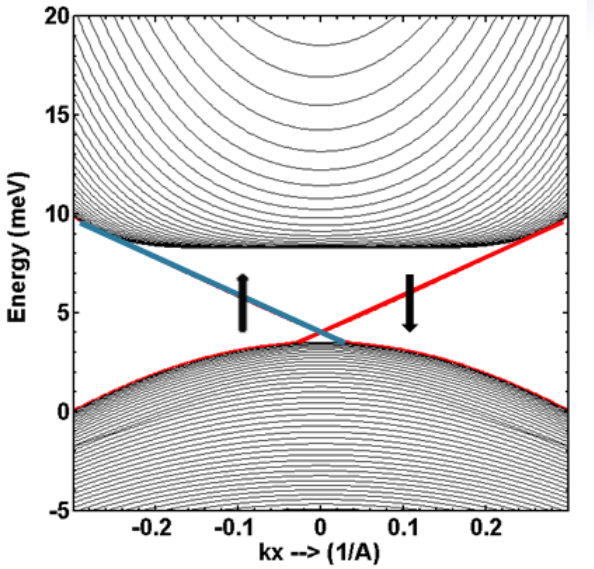

Fig. 6.7. Band structure of the GaN/InN/GaN 100.0 nm nano-ribbon. The two surface bands have opposite spin-polarization distinguished by two different colours.

were computed. The wave functions (Fig. 6.8) peak at the edges and decay rapidly in to the bulk

6.6 Edge states under influence of electric and magnetic field

The Dirac cones in a GaN/InN/GaN heterostructure are degenerate. Under the influence of an external electric field or magnetic field (Fig. 6.9), the two degenerate Dirac cones split in energy and separate along the energy axis (Fig. 6.10). Similarly when an external B field is applied along the z-axis, the two degenerate Dirac cones shift along the x-axis (Fig. 6.11). The B-field acts as a horizontal gate. From the original Γ point, the two Dirac cones are not situated at k_x = -0.013 1/nm and -0.032 1/nm.

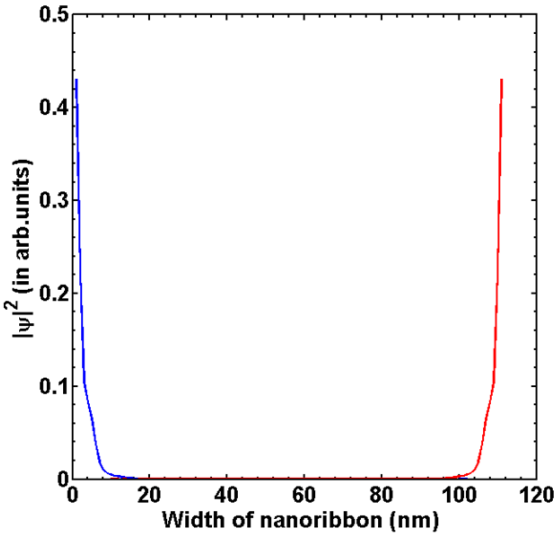

Fig. 6.8. The wave function of the edge state in GaN/InN/GaN 100.0 nm nano-ribbon shows a maximum at the boundary and decays in the bulk. A conclusive proof that the edge states are fully localized

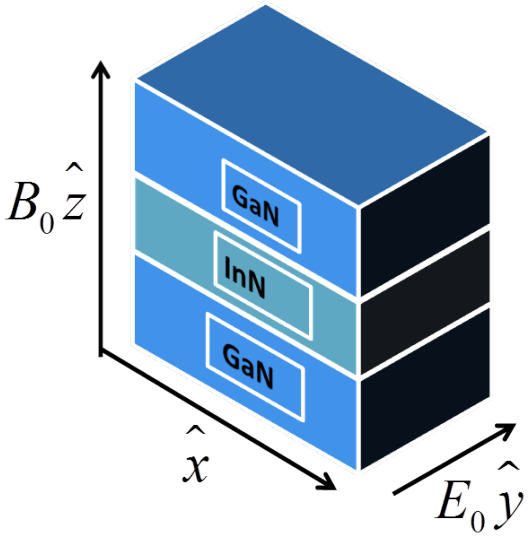

Fig. 6.9. A GaN/InN/GaN nanoribbon of 100.0 nm width is confined along y and z axes. Electric and magnetic field is applied along the y and z axes. The magnetic field is added to the Hamiltonian using a Landau gauge.

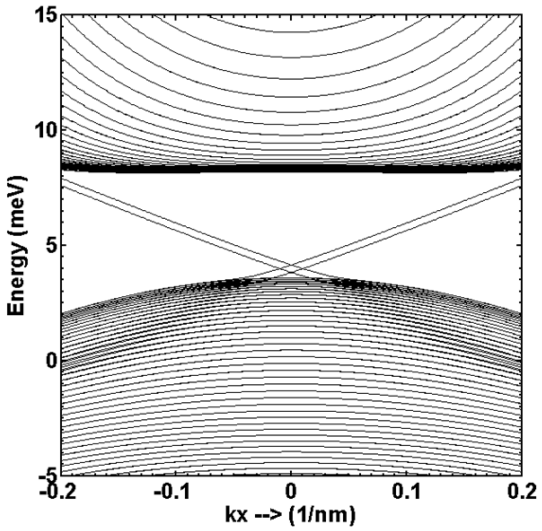

Fig. 6.10. Band structure of the GaN/InN/GaN broken-gap heterostructure under electric field = 1.5 MV/cm. The two Dirac cones are now positioned at 3.842 meV and 4.187 meV

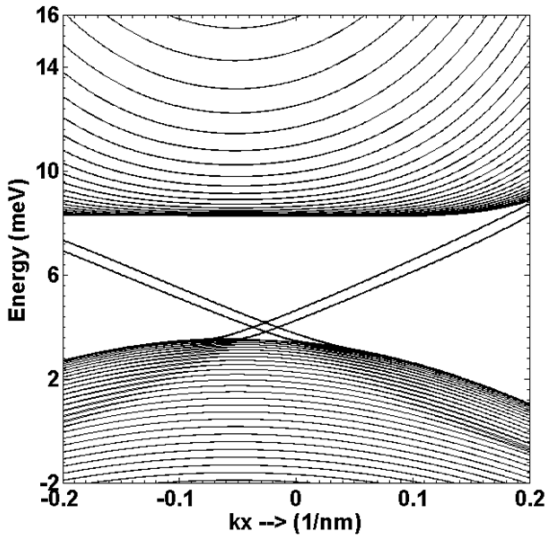

Fig. 6.11. Band structure of the GaN/InN/GaN under an external magnetic field of 10 T along the z-axis.

6.7 Conclusion

A GaN/InN/GaN heterostructure with topological insulator edge states is perhaps only a few known instances where spin-orbit coupling effects do not play a part.

GaSb/InAs broken gap heterostructure and strain-induced topological band order in cubic semiconductors [98] are the other experimentally verified cases. It is important to note here that the width of the InN quantum well is a vital number. A very thin InN quantum well will change the inverted band order to normal because of sheer geometric confinement effects while a very wide quantum well diminishes the electric potential. An optimal value of InN well must be chosen that preserves the inverted band order and also thick enough to allow strain to be considered as pseudomorphic.

7. TOPOLOGICAL INSULATOR NANOSTRUCTURES

7.1 Introduction

Topological insulator nanostructures offer significant advantages over bulk materials. The most crucial advantage of a nanostructure is the increased surface-to-volume ratio. This holds more true for TI nanostructures because the surface states are the most important feature of these materials. Research groups worldwide have synthesised TI nanostructures [99, 100]. This chapter utilizes the information presented in the preceding chapters to construct useful devices that can be applied in the semiconductor industry. As a first example, the current-voltage characteristics of a TI ultra-thin body is examined. A possible use of this could be as components of a fast-switching low-power circuit environment. It is imperative to mention that TI surface states offer electronic mobility values that far outweigh those of Silicon, the current material extensively used in industry [101, 102]. As a comparative measure, Si has mobility of 1400 $cm^2/V.s$ while a Bi_2Te_3 thin film has been experimentally determined to have around 10,200 $cm^2/V.s$. The high mobility of TI surface states arise because of the protection from back-scattering.

7.2 Current-voltage characteristics of a Bi_2Te_3 ultra-thin body

An UTB constructed out of Bi_2Te_3 is shown in Fig. 7.1. The structure is geometrically confined along the z-axis. Open boundary conditions (transport direction) is along the x-axis. The y-axis is assumed to be periodic. The temperature of operation is 300 K.

An external voltage was applied between the two contacts placed along the x-axis. These two contacts serve as source and drain. The transmission profile of this device

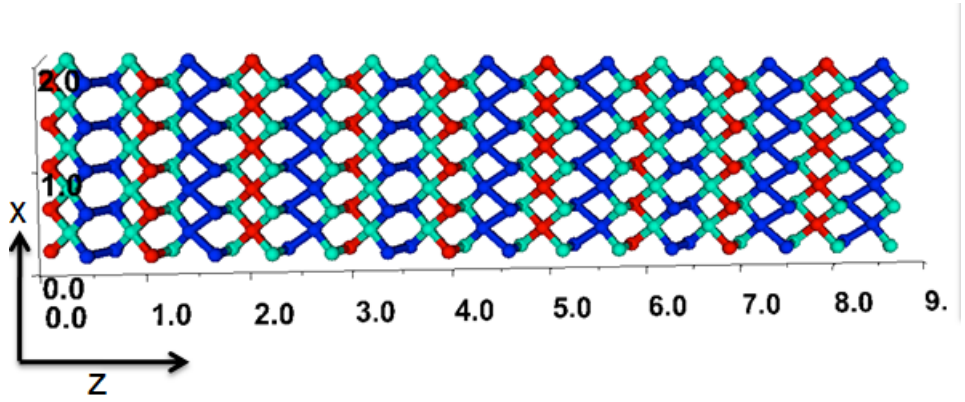

Fig. 7.1. Topological insulator ultra-thin body confined geometrically along z-direction and measures 8.942 nm. Contacts are placed along x-axis and this dimension is 1.972 nm. The y-axis is periodic

(Fig. 7.2) under the applied external voltage was computed within the non-equilibrium Green's function formalism. Using the transmission data, current in the device as a function of the external voltage Fig. 7.4) was computed by a direct application of the Landauer-Büttiker formalism. As a guide to the eye, the dispersion of the ultra-thin-body is shown in Fig. 7.3. External bias, with reference to Fig. 7.3 is applied between 0.0 and 0.2 eV to completely cover the TI surface states. Similar current-voltage plots were compared with graphene (because of identical linear dispersion) and Silicon. The current-voltage characteristics of Silicon reveal that at low values of external voltages, current is negligible. A TI ultra-thin body on the other hand delivers sufficient current (Fig. 7.5) at a low source-drain bias. A comparable graphene device also delivered current which was six-fold less than its TI counterpart.

TI surface states can deliver current at low biases because of their semi-metallic character. The transistor fabricated out of a TI, therefore, is present in a turn-on state by default. Silicon, at low biases has zero or negligible density of states since they possess a finite band-gap unlike the zero-gap metal-like states of TI.

While, the aforementioned low-power attribute of TI based transistors is attractive, it also presents a significant challenge to turn-off this device. Leakage losses in a permanently turned-on device would far offset the potential benefits of a TI transis-

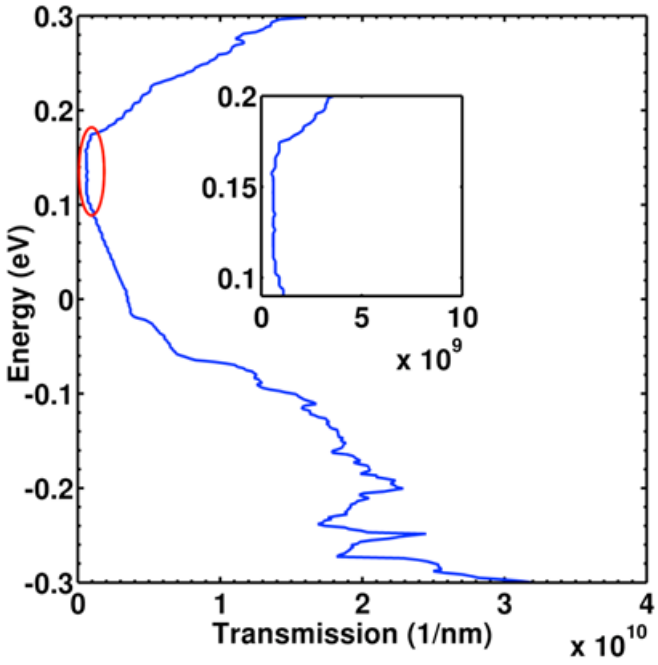

Fig. 7.2. Transmission profile of the TI ultra-thin body. The distinguishing feature of this transmission plot is the flat profile in the region of surface states.

tor. There are multiple ways, theoretically, to turn off a TI device. Under the action of an external magnetic field, the band-gap closing states would separate and form a finite gap. By placing the fermi-level within the gap, the device can be turned off. In a real miniaturized semiconductor chip, an external magnetic field would be hard to apply without impacting the performance of the neighbouring electronic circuitry. A more sophisticated way of opening a band-gap is through a TI-superconductor heterostructure. The behaviour of a topological insulator in presence of a superconductor is covered in Chapter 8.

7.3 Topological Insulator nanowires

Topological insulator nanoribbons have been studied to understand fundamental condensed matter physics with Dirac fermions. Significant studies have included

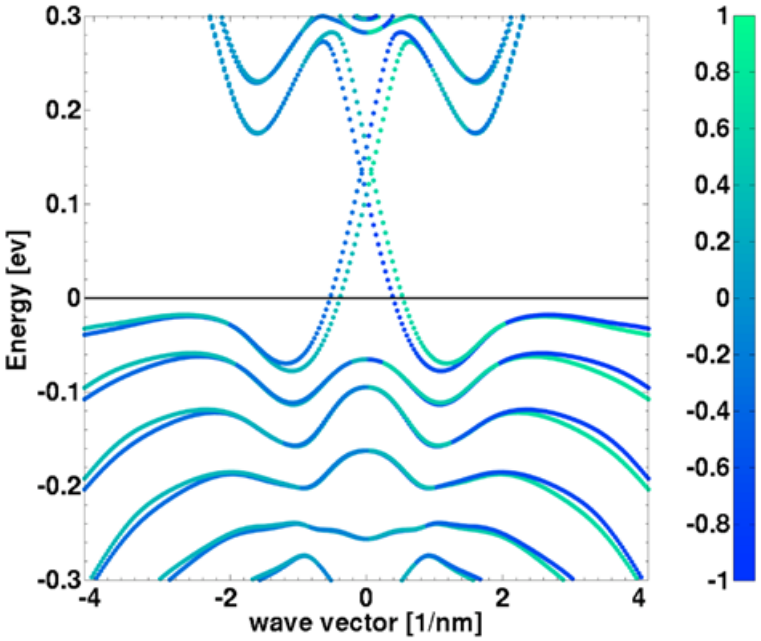

Fig. 7.3. Energy band diagram for the ultra-thin body. It is assumed that the application of a moderate electric field preserves this band structure. The energies on this plot serve as a guide to position the fermi-level. The two colours indicate spin polarization of the bands. The colour bar signifies the intensity of spin polarization. The TI surface bands are completely spin polarized as expected.

Ahronov-Bohm oscillations [103,104], weak anti-localization [105], SdH oscillations [106] etc. High-resolution TEM imaging and 2D Fourier transformed electron diffraction measurements demonstrate that the samples are single-crystalline rhombohedral phase and grow along the $[11\bar{2}0]$ direction.

7.4 Results and Discussion

Bi_2Te_3 has been reported as a strong topological insulator with a Dirac node at its surface. In this section, nanowires constructed out of this material are described and their properties analyzed with respect to geometry, dimension, and growth direction.

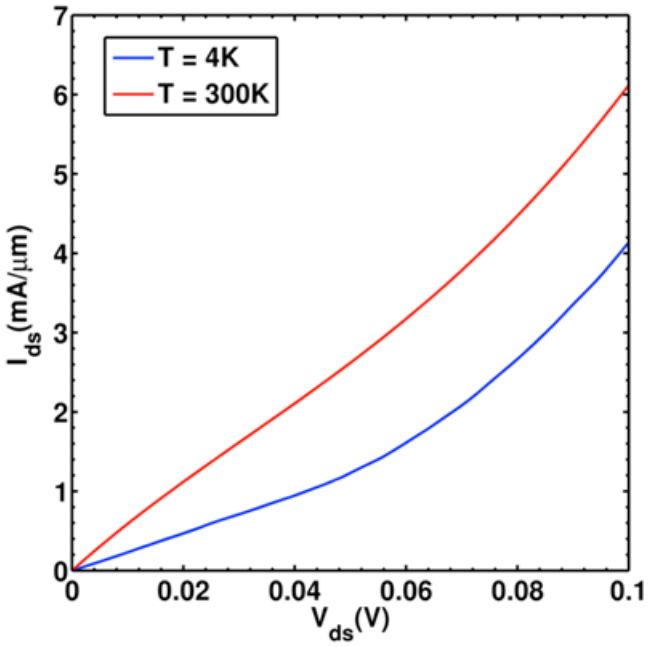

Fig. 7.4. I-V characteristics for the TI ultra-thin body shown in Fig 7.1. At low bias values, the current delivered is sufficiently large compared to traditional semiconductor materials.

Nanowires are chosen as a target application because they can act both as active devices and wire connectors.

7.4.1 Cylindrical Nanowires

The first nanowire structure considered is a 6.0 nm diameter cylinder. This device was found to have a Dirac crossing at 0.06 eV (Fig.7.6). The crossing is identified to possess topological behaviour by observing its spin-polarized nature. The two bands that cross at this energy are strongly spin-polarized as indicated by their distinct colours. The colurs of the band on the dispersion represent the spin polarization. To test for the robustness of these states at smaller dimensions, the previously simulated cylinder diameter was scaled by 50%. At 3.0 nm diameter, no topological states were observed. States in the mid-gap region did not show the characteristic band

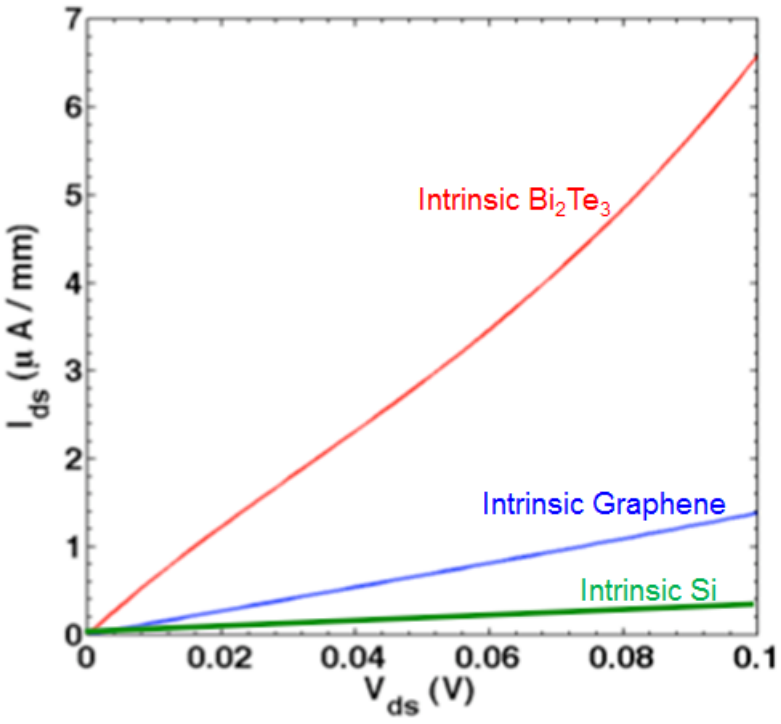

Fig. 7.5. Comparison of the I-V characteristics of ultra-thin bodies made out of Bi_2Te_3, graphene, and silicon.

gap closing Dirac cone. Instead, a clear energy difference was seen between the states denoting a normal insulator behaviour. The disappearance of topologically protected surface states is explained by examining the device structure carefully. At small dimensions, the distinction betwen surface and volume is unclear, surface states penetrate the bulk and hybridize to give an all-equivalent surface atom chain. Therefore, to obtain strong topological states, a threshold dimension for a given device geometry is a necessary requirement.

7.4.2 Squared Nanowires

Electronic transport at the nanoscale regime is widely studied on squared cross-sectional nanowire based devices. Therefore, it is important to determine whether topological insulator nanowires can be an attractive material for the semiconductor

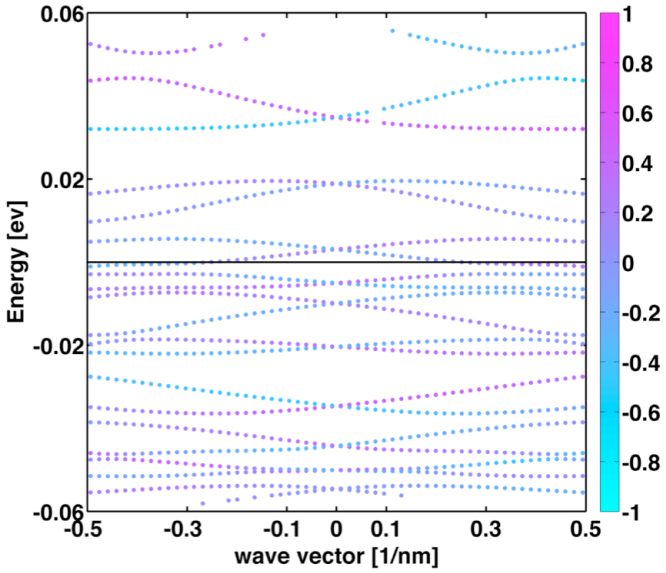

Fig. 7.6. Spin polarized dispersion of a 6.0 nm Bi_2Te_3 cylindrical nanowire. The Dirac crossing is at around 0.06 eV. The colour bar on the right indicates the strength of spin polarization.

industry. To that end, a squared nanowire with a 6.0 nm edge was simulated. The simulation structure is shown in Fig.7.7. Unlike, a cylinder, this structure possesses two very different surface atom arrangement. The two different surfaces are maked as "A" and "B" on Fig.7.7 Thus, unlike a cylinder, there are two different surfaces and a significant change in the band structure is expected. Analysis of the spin polarized bands reveal a very weak degree of polarization (Fig.7.8). Since topological insulators exhibit strongly spin-polarized bands, it is therefore safe to conclude that surface states in a squared nanowire will not have properties associated with TIs. The absence of strong spin polarized bands can be thought of as an outcome of the reduced symmetry of the squared wire. Because of reduced symmetry, surface atomic arrangement is not unique as a cylinder.

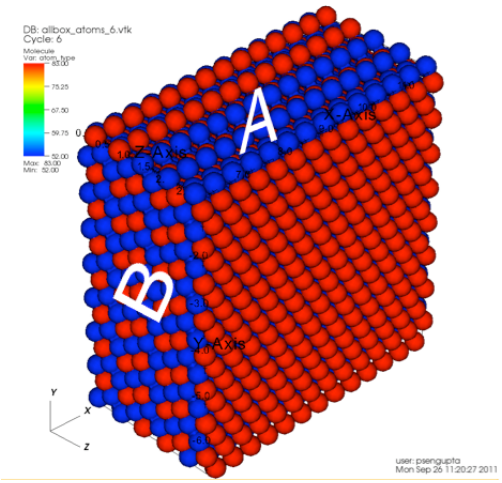

Fig. 7.7. Surface atom arrangement on a 6.0 nm squared cross-sectional nanowire. Two surfaces with distinct atom arrangement are alphabetically marked.

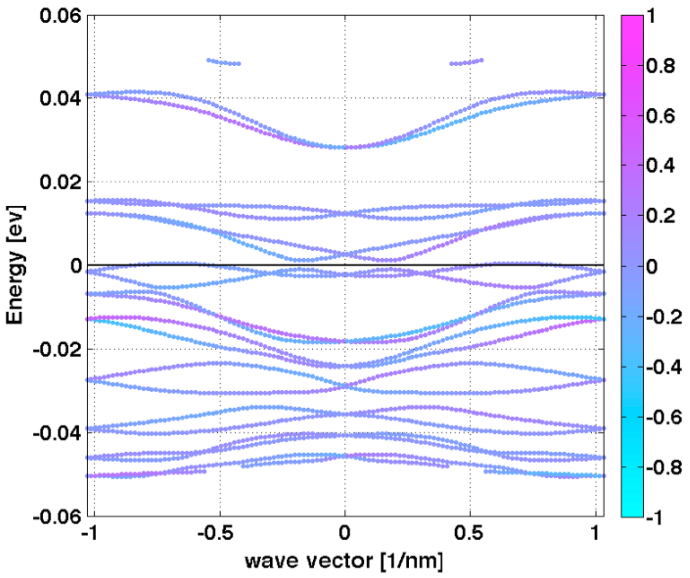

Fig. 7.8. Spin polarized dispersion for a square cross-sectional nanowire. Spin polarization is weak for this structure. The edge of this device is set to 6.0 nm.

7.4.3 Composite nanowires

In the previous two subsections, it was demonstrated how through simulation, topological insulator states were observed for cylindrical nanowires. Squared cross-

sectional nanowires were determined to be unsuitable for topological insulator based devices. It is therefore interesting to find the behaviour of a device that has both cylindrical and square cross sections. Two cases are considered: 1). Rectangular nanowire with a cylindrical face (Fig.7.9a) and 2). Cylindrical nanowire with a rectangular bottom surface (Fig.7.9b). For case 2), topological surface states were identified and were

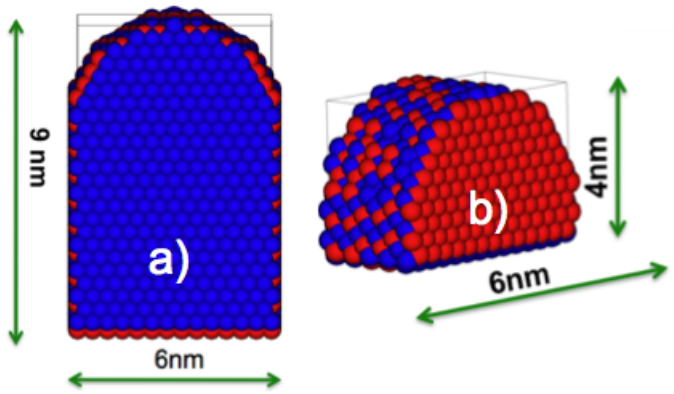

Fig. 7.9. Fig.6a is the cross-sectional view of a rectangular nanowire with a cylindrical face. Fig.6b shows a cylindrical nanowire with rectangular bottom surface. The dimensions for both the structures are mentioned on the plot.

strongly spin polarized (Fig.7.10). Case 1) with a predominantly square cross-section (Fig.7.9b) does not show a strongly polarized surface band dispersion. These observations are consistent with earlier predictions about the lack of topological surface states in squared wires.

7.5 Growth Direction of nanowires

Growth direction for nanowires significantly affect their electronic properties. The cases studied so far have been on wires that were grown along the c-axis. Further simulation runs were conducted on 6.0 nm diameter cylindrical nanowires grown along <110> and <111>. <110> wires are not topological insulators. <111> wires

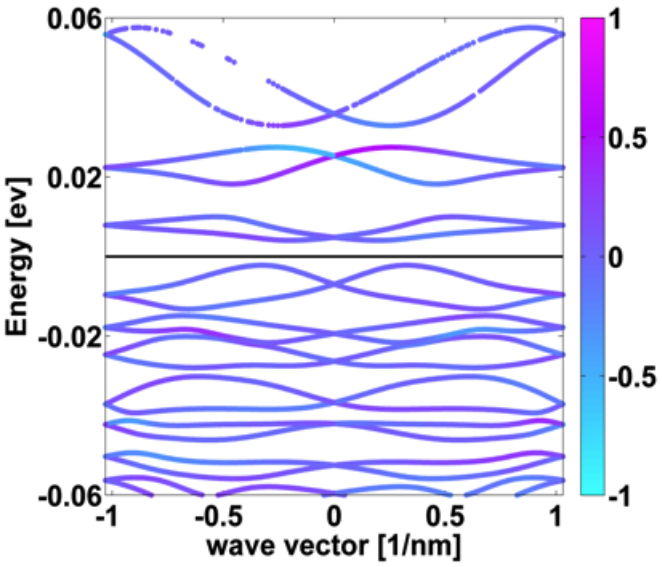

Fig. 7.10. Spin polarized dispersion for the structure of Fig.6b.

have highly spin polarized dispersion confirming them as strong topological insulators (Fig.7.11). The spin axis is taken to be the growth direction <111>.

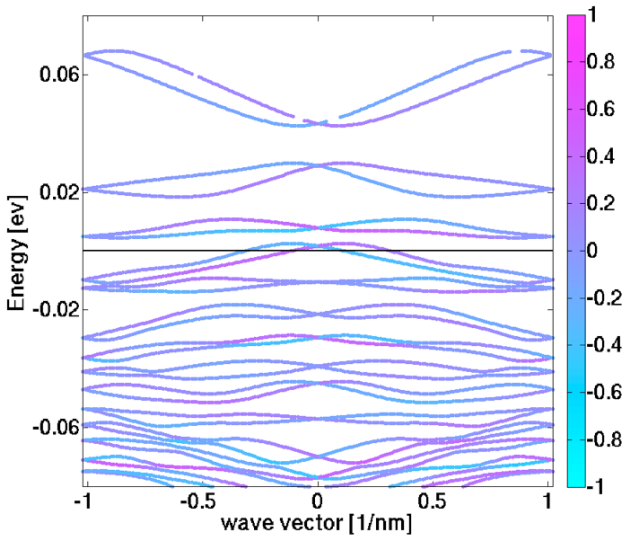

Fig. 7.11. Spin polarized dispersion for a 6.0 nm diameter cylindrical wire grown along <111> axis. Dirac cones are present around 0.01 eV.

7.6 Conclusion

The present work investigates geometric conditions under which Bi_2Te_3 cylindrical nanowire can be grown to maximise the benefits afforded by topological insulators. Nanowires demonstrate topological insulator behaviour when dimensions are above a certain threshold. This threshold value is approximately 5.0 nm in diameter for a cylindrical nanowire. Wires which do not satisfy this criterion cannot be used as TI materials. Further, the shape of wire plays a significant role in ascertaining if a certain device is a TI. It was found that cylindrical wires are strong TIs while squared nanowires have weak spin polarized bands and hence unsuitable for TI applications. Composite nanowires continue the trend; strong TI behaviour is observed when the device is primarily cylindrical. Lastly, the direction of growth axis was another parameter that can be manipulated to create topological surface states. Calculations reveal wires grown along <001> and <111> directions demonstrate TI features. <110> grown wires do not have spin-polarized surface bands.

8. SUPERCONDUCTORS AND TOPOLOGICAL INSULATORS

8.1 Introduction

It is now well established that doping of Cu or Pb can add superconducting states to Bi_2Se_3. The proximity effect at the interface between a superconductor and topological insulator has attracted considerable attention [107, 108]. Because of proximity effect, when a TI surface state is closely placed with a superconductor (Fig. 8.1), the superconductor's wave functions can penetrate into the topological surface states (Fig. 8.2) and turn them in to superconducting states. A superconductor has an intrinsic energy gap between the Fermi-level and the superconducting ground state. As noted before in Chapter 7, this could be a possible way to open a band-gap in a topological insulator. In this chapter, a modified version of the BdG Hamiltonian for a 3D-TI and s-wave superconductor is presented.

8.2 Hamiltonian for 3D TI and s-wave superconductor heterostructure

Before a complete Hamiltonian for a TI-superconductor heterostructure can be written, the conventional BCS description [110,111] of an s-wave superconductor must

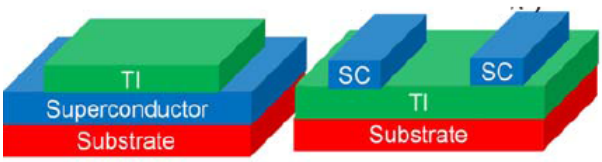

Fig. 8.1. Schematic of a TI grown epitaxially on a superconductor (left) and a superconductor film layered on a TI film [109].

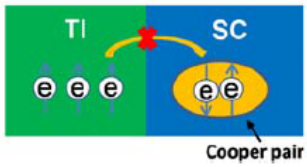

Fig. 8.2. Cartoon of Cooper pair transfer from the superconductor to topological insulator [109].

be examined. The BCS Hamiltonian in its simplest form can be written by starting with a Hamiltonian (Eq. 8.1) that describes a many-Fermion system interacting via a spin-independent interaction potential.

$$H = \sum_{\sigma} \int d^3x \psi_{\sigma}^{+}(x) \left(\frac{-\hbar^2 \nabla^2}{2m} - \mu \right) \psi_{\sigma}(x) + \frac{1}{2} \sum_{\sigma\sigma'} \int d^3x d^3x' V(x,x') \psi_{\sigma}^{+}(x) \psi_{\sigma}^{+}(x') \psi_{\sigma}(x) \psi_{\sigma}(x') \tag{8.1}$$

In momentum space and finite volume, the following substitutions can be made

$$\psi(x) = \frac{1}{\sqrt{\Omega}} \sum_{q} e^{ik\cdot x}, V(x) = \frac{1}{\Omega} \sum_{q} e^{ik\cdot x} \overline{V_q} \tag{8.2}$$

The Hamiltonian in Eq. 8.1 can therefore be now written as

$$H = \sum_{k\sigma} \varepsilon_k a_{k\sigma}^{+} a_{k\sigma} + \frac{1}{2\Omega} \sum_{\sigma\sigma'} \sum_{kk'q} \overline{V_q} a_{k+q,\sigma}^{+} a_{k'-q,\sigma'}^{+} a_{k\sigma} a_{k'\sigma'} \tag{8.3}$$

By restricting to paired fermions with zero total momentum and opposite spin, the BCS Hamiltonian can be written as

$$H = \sum_{k\sigma} \varepsilon_k a_{k\sigma}^{+} a_{k\sigma} + \frac{1}{\Omega} \sum_{kk'} V_{k-k'} a_{k'\uparrow}^{+} a_{-k'\downarrow}^{+} a_{k\uparrow} a_{-k\downarrow} \tag{8.4}$$

The spectrum of this Hamiltonian when solved using the Bogoliubov transformation [112] yields a band structure [113] with a gap (Fig. 8.3) in the spectrum. For studying proximity effect between a superconductor [114, 115] and a topological insulator, the 4-band k.p model (introduced in Chapter 2) and the BCS Hamiltonian is used in conjunction. The fundamental assumption (experimentally verified) of the

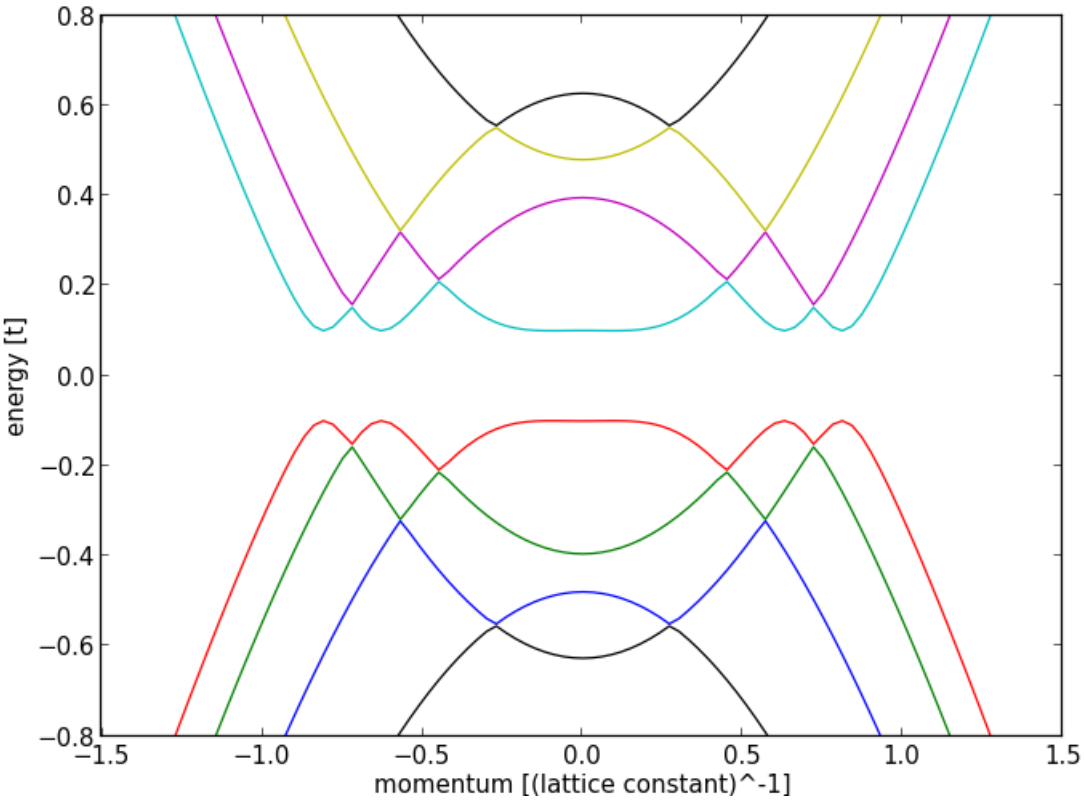

Fig. 8.3. Band structure of a simple s-wave superconductor calculated with the BdG Hamiltonian. In calculating this spectrum the Fermi-level was set to 0.7 eV and the pair potential is equal to 0.1 eV. The superconducting gap in the spectrum is clearly visible.

BCS Hamiltonian is the formation of Cooper pairs which are electrons with zero total momentum and spin. Superconductivity which is induced on the TI side of the TI-SC heterostructure must therefore agree to this principle. At this point it is worth mentioning again that the four orbitals participating in the electronic bonding process are $|P1_z^+ \uparrow\rangle$, $|P2_z^- \uparrow\rangle$, $|P1_z^+ \downarrow\rangle$, and $|P2_z^- \downarrow\rangle$. The composite Hamiltonian for the TI-SC structure similar to the BdG Hamiltonian can now be written as

$$H_{TS} = \begin{pmatrix} H_T - \mu & \Delta \\ \Delta^* & \mu - TH_TT^{-1} \end{pmatrix} \tag{8.5}$$

In Eq. 8.5, μ denotes the Fermi-level and T is the time reversal operator. H_{TS} is the composite Hamiltonian and H_T represents the 4-band k.p Hamiltonian. Δ is the pair potential given in the BCS formulation. For the s-wave superconductor considered here, the pair-potential is just a number. The analytic representation of pair-potential changes to a $\overrightarrow{k}$ dependent quantity if p or d-type superconductors are considered. The pair potential Δ connects the two electrons with opposite momentum and spin. For the case of a TI, which is turned in to a superconductor, the orbitals with opposite spin and momentum are paired. The two sets of orbitals in the 4-band TI Hamiltonian are therefore coupled by two pair potentials. The full TI-SC Hamiltonian H_{TS} in the basis set $|P1_z^+ \uparrow\rangle$, $|P2_z^- \uparrow\rangle$, $|P1_z^+ \downarrow\rangle$, $|P2_z^- \downarrow\rangle$, $-|P1_z^+ \uparrow\rangle$, $-|P2_z^- \uparrow\rangle$, $-|P1_z^+ \downarrow\rangle$, and $-|P2_z^- \downarrow\rangle$ can be now written as

$$H_{TS} = \begin{pmatrix} \epsilon + M & A_1k_z & 0 & A_2k_- & 0 & 0 & \Delta_1 & 0 \\ A_1k_z & \epsilon - M & A_2k_- & 0 & 0 & 0 & 0 & \Delta_2 \\ 0 & A_2k_+ & \epsilon + M & -A_1k_z & -\Delta_1 & 0 & 0 & 0 \\ A_2k_+ & 0 & -A_1k_z & \epsilon - M & 0 & -\Delta_2 & 0 & 0 \\ 0 & 0 & -\Delta_1^* & 0 & -\epsilon - M & A_1k_z & 0 & A_2k_- \\ 0 & 0 & 0 & -\Delta 2^* & A_1k_z & -\epsilon + M & A_2k_- & 0 \\ \Delta_1^* & 0 & 0 & 0 & 0 & A_2k_+ & -\epsilon - M & -A_1k_z \\ 0 & \Delta_2^* & 0 & 0 & A_2k_+ & 0 & -A_1k_z & -\epsilon + M \end{pmatrix} \tag{8.6}$$

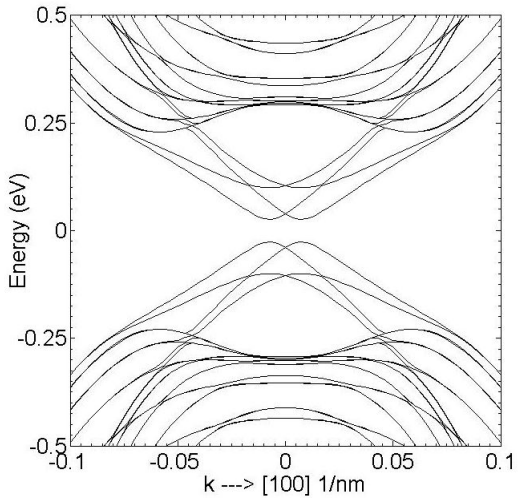

Fig. 8.4. Band structure of a TI and s-wave superconductor heterostructure calculated with the modified BdG Hamiltonian. In calculating this spectrum the Fermi-level was set to 0 and the pair potential Δ_1 and Δ_2 was assumed to be to 0.1 eV. The TI chosen is a 8.0 nm thick Bi_2Se_3 film.

where where $\epsilon(k) = C + D_1 k_z^2 + D_2 k_\perp^2$, $M(k) = M_0 + B_1 k_z^2 + B_2 k_\perp^2$ and $k_\pm = k_x \pm i k_y$. In the above Hamiltonian, the Fermi-level μ has been set to zero. The dispersion for the TI obtained in the presence of a superconductor is shown in Fig. 8.4. The pair potentials were assumed to be zero beyond two layers. A more accurate calculation presented in the next section does not require this empirical assumption.

8.3 Self-consistent calculation of the order parameter

A more rigorous calculation of the pair potential or order parameter can now be set-up through a self-consistent calculation. The pair potential Δ_1, for instance is given as

$$\Delta_1 = f(z) \int dk_\parallel \langle \psi_{1\uparrow}(k_\parallel, z) \psi_{1\downarrow}(-k_\parallel, z) \tag{8.7}$$

In eq. 8.7, $\psi_{1\uparrow}$ and $\psi_{1\downarrow}$ refer to the wave function components in the 8×1 column vector that correspond to $|P1_z^+ \uparrow\rangle$ and $-|P1_z^+ \downarrow\rangle$.

The order parameter when computed as a function of the confined direction shows a rapidly decaying behaviour. This is expected as the penetration of the superconductor wave function is limited to a few layers on the surface.

8.4 Conclusion

The proximity effect between an s-wave superconductor and topological insulator has been investigated. In setting up the Hamiltonian for the TI-SC heterostructure, strong coupling between the superconductor and TI has been assumed. While this coupling has modified the TI surface states by opening a band gap, a similar pattern can also be observed on the superconductor side. Modification of superconducting properties in the presence of a TI has not been considered in this thesis.

9. FUTURE WORK

9.1 Current trends in topological insulators

The discovery of topological insulators has opened up extensive experimental and theoretical research by several groups across the world. Potential future applications that include areas as diverse as thermoelectrics, spintronics, and quantum computing are being explored. It is beyond the scope of this thesis to include several topics that themselves on their own stand merit as a complete body of work. This chapter summarizes a few such key items that have been not been covered here. A short description of the problem and a possible approach has been outlined.

9.2 Electron-phonon scattering on topological insulator nanowires and ultra-thin bodies

All the terminal characteristics of the topological insulator ultra-thin bodies calculated so far have been under ballistic conditions. An electron on the surface is assumed to zip across the two contacts of the device without suffering any scattering. Simulation of realistic electron transport require that scattering on the surface be accounted for to better match experimental results. The next few sections would outline a plan to set-up electron scattering on the surface of topological insulators [116].

Modeling the electron-phonon scattering depends on choosing a correct form of the Hamiltonian. To compute the scattering rates, a 4x4 k.p model can be used to accurately reproduce the Dirac surface states. A 4x4 k.p model (eqn 9.1) is more numerically tractable than a twenty-band tight binding Hamiltonian. In carrying out a detailed temperature dependent resistivity, it is assumed that electron-phonon scattering is the dominant source of quasi-particle decay and back scattering. Electron-

electron interactions are indeed expected to give sub-leading order corrections at finite temperatures. The model Hamiltonian given in Chapter 2 is repeated here again for convenience.

$$H(k) = \epsilon(k) + \begin{pmatrix} M & iA_1k_z & 0 & A_2k_- \\ 0 & -M & A_2k_- & 0 \\ 0 & A_2k_+ & M & -iA_1k_z \\ A_2k_+ & 0 & -iA_1k_z & -M \end{pmatrix} \tag{9.1}$$

where

$$\begin{aligned} \epsilon(k) &= (C + D_1k_z^2 + D_2\left(k_x^2 + k_y^2\right))I_{4\times4} \\ M &= M_0 - B_1k_z^2 - B_2\left(k_x^2 + k_y^2\right) \\ k_\pm &= k_x \pm ik_y \end{aligned} \tag{9.2}$$

The next part in setting up the program of electron-phonon scattering is to model the phonons using elastic continuum theory. Previous work on related materials have shown that isotropic elastic continuum theory provides a reasonable approximation.

Using a low-energy electronic Hamiltonian and an isotropic elastic continuum approach for the phonons, with the deformation coupling providing the dominant interaction, the electron-phonon coupling can be computed. In short, three different Hamiltonian have to be modeled to address the scattering problem (eq. **??**).

$$H_{tot} = H_{electronic} + H_{phonon} + H_{el-ph} \tag{9.3}$$

9.3 Spin transport in topological insulators

Topological insulators are strongly driven by a high measure of spin-orbit coupling. The existence of metallic Dirac-fermion surface states char- acterized by an intrinsic spin helicity: the wave vector of the electron determines its spin state. A net spin density is thus produced upon driving a charge current at the surface of a TI.

Considerable effort has been devoted recently to possible applications of this property in constructing spin-based devices.

The striking feature of the surface states of topological insulators is the helicity of the spin polarization vector. The spin polarization vector, along the constant energy contours is defined in eqn(9.4).

$$\vec{P}\left(\vec{k}\right) = 2/\hbar\left[\langle S\left(\vec{k_x}\right)\rangle, \langle S\left(\vec{k_y}\right)\rangle, \langle S\left(\vec{k_z}\right)\rangle\right] \tag{9.4}$$

The expectation values of spin operators is given by

$$\langle S_{\alpha i}\left(\vec{k_x}\right)\rangle = \hbar/2\langle\psi_i\left(\vec{k}\right)|\sigma_i|\psi_i\left(\vec{k}\right)\rangle \tag{9.5}$$

are the two-component spinor wave functions. σ_{i} denotes the Pauli matrices. The recent spin- and angle-resolved photo-emission spectroscopy (spin-ARPES) experiments have indeed indicated a one-to-one locking of the momentum and the direction of spin polarization vector pointing along $\left(\vec{k}\times\vec{z}\right)$

From the point of view of technological applications, an attractive feature of the TI materials is the intrinsic spin polarization of the current carried by the topological surface states. To model the spin transport in the simplest form, a drift-diffusion type equation is considered. The equations(9.6, 9.7) assumes that the two spin projections serve as the electrons and holes.

$$J_\uparrow = n_\uparrow e\mu_\uparrow E + eD_\uparrow\frac{dn_\uparrow}{dx} \tag{9.6}$$

$$J_\downarrow = n_\downarrow e\mu_\downarrow E + eD_\downarrow\frac{dn_\downarrow}{dx} \tag{9.7}$$

The related continuity equations for the up-spin and down-spin electron densities are given by eqn(9.8, 9.9)

$$\frac{dn_\uparrow}{dt} = \frac{-n_\uparrow}{\tau_{\uparrow\downarrow}} + \frac{n_\downarrow}{\tau_{\downarrow\uparrow}} + \frac{1}{e}\frac{d}{dx}J_\uparrow \tag{9.8}$$

$$\frac{dn_\downarrow}{dt} = \frac{-n_\downarrow}{\tau_{\downarrow\uparrow}} + \frac{n_\uparrow}{\tau_{\uparrow\downarrow}} + \frac{1}{e}\frac{d}{dx}J_\downarrow \tag{9.9}$$

The driving electric field is $\vec{E}$, the electron charge is e and the mobilities of up-spin and down-spin electrons are given by $\mu_\uparrow$ and $\mu_\downarrow$ respectively.

$\tau_{\uparrow\downarrow}$ and $\tau_{\downarrow\uparrow}$ denote the in-out scattering rates for the spin population. For a topological insulator, the correct spin-flipping mechanism to accurately determine the scattering rates have to be investigated.

9.4 Ferromagnetic materials: An efficient way of controlling the TI surface states

For real device applications, an efficient way of controlling the surface states is of utmost importance. It has been proven theoretically that TIs can have many exotic physical properties related to the breaking of time reversal symmetry. Of the many possibilities explored, introduction of a ferromagnetic material is considered particularly promising. The exchange interaction with a proximate magnetic field can affect the TI surface states more effectively than an external magnetic field.

A thin strip of ferro-magnetic layer is deposited on the top surface of a TI. The electron transmission through a single ferro-magnetic barrier can be made significantly dependent on the mutual orientation of the current $\vec{J}$ and the magnetization. For instance, in-plane magnetization of the ferromagnetic layer induces a shift in the Dirac cone of the surface states in contact away from the Brillouin zone centre. When the displacement is in the direction of $\vec{J}$, the introduced magnetic barrier is not expected to affect electron transmission substantially. Moreover, orientating the magnetization vector perpendicular to the TI surface leads to a finite band gap. Thus, a single ferromagnetic barrier with variable magnetization appears to be sufficient to modulate the electrical current on the surface of a TI.

9.5 Andreev reflection at a topological insulator superconductor interface

A metal/superconductor interface reflects an incident electron from the metal as a positively charged hole with opposite spin. In the process a Cooper pair is formed

in the superconductor. This electron-hole conversion is known as Andreev reflection. Andreev reflection coefficient [117] for different classes of topological insulator in presence of disorder, both magnetic and non-magnetic can be computed. Further, experiments have already been reported that show suppression of Andreev reflection within the superconducting gap. This experimental result is explained by noting that the surface state of a TI is spin-polarized and spin is locked to momentum perpendicularly. This spin-momentum locking allows only one spin polarization of electrons (which does not satisfy the Cooper pair requirement) thus eliminating Andreev reflection.

LIST OF REFERENCES

LIST OF REFERENCES

[1] M. Z. Hasan and C. L. Kane, "*Colloquium*: Topological insulators," *Rev. Mod. Phys.*, vol. 82, pp. 3045–3067, Nov 2010.

[2] X.-L. Qi and S.-C. Zhang, "Topological insulators and superconductors," *Reviews of Modern Physics*, vol. 83, no. 4, p. 1057, 2011.

[3] D. R. Cooper, B. DAnjou, N. Ghattamaneni, B. Harack, M. Hilke, A. Horth, N. Majlis, M. Massicotte, L. Vandsburger, E. Whiteway, *et al.*, "Experimental review of graphene," *ISRN Condensed Matter Physics*, vol. 2012, 2012.

[4] T. L. Hughes, E. Prodan, and B. A. Bernevig, "Inversion-symmetric topological insulators," *Physical Review B*, vol. 83, no. 24, p. 245132, 2011.

[5] J. Moore and L. Balents, "Topological invariants of time-reversal-invariant band structures," *Physical Review B*, vol. 75, no. 12, p. 121306, 2007.

[6] M. Stone, *Quantum Hall Effect*. World Scientific, 1981.

[7] D. Arovas, J. R. Schrieffer, and F. Wilczek, "Fractional statistics and the quantum hall effect," *Physical review letters*, vol. 53, pp. 722–723, 1984.

[8] S. M. Girvin and R. Prange, "The quantum hall effect," *Les Houches Lecture Notes (Springer-Verlag, New York, 1998)*, 1987.

[9] T. Chakraborty and P. Pietiläinen, *The quantum hall effects: Integral and fractional*. Springer-Verlag, 1995.

[10] F. Wilczek and A. Shapere, *Geometric phases in physics*, vol. 5. World Scientific, 1989.

[11] Z. F. Ezawa, *Quantum Hall Effects: Field Theorectical Approach and Related Topics*. World Scientific, 2008.

[12] R. B. Laughlin, "Quantized hall conductivity in two dimensions," *Physical Review B*, vol. 23, no. 10, p. 5632, 1981.

[13] J. K. Jain, "Composite-fermion approach for the fractional quantum hall effect," *Physical review letters*, vol. 63, no. 2, p. 199, 1989.

[14] N. Nagaosa, "A new state of quantum matter," *Science*, vol. 318, no. 5851, pp. 758–759, 2007.

[15] C. Kane and E. Mele, "Quantum spin hall effect in graphene," *Physical Review Letters*, vol. 95, no. 22, p. 226801, 2005.

[16] C. L. Kane and E. J. Mele, "Z_ {2} topological order and the quantum spin hall effect," *Physical review letters*, vol. 95, no. 14, p. 146802, 2005.

[17] B. A. Bernevig and S.-C. Zhang, "Quantum spin hall effect," *Physical review letters*, vol. 96, no. 10, p. 106802, 2006.

[18] F. Haldane, "Model for a quantum hall effect without landau levels: Condensed-matter realization of theparity anomaly," *Physical Review Letters*, vol. 61, no. 18, pp. 2015–2018, 1988.

[19] M. König, S. Wiedmann, C. Brüne, A. Roth, H. Buhmann, L. Molenkamp, X. Qi, and S. Zhang, "Quantum spin hall insulator state in hgte quantum wells," *Science*, vol. 318, no. 5851, pp. 766–770, 2007.

[20] X.-L. Qi and S.-C. Zhang, "The quantum spin hall effect and topological insulators," *Physics Today*, vol. 63, no. 1, pp. 33–38, 2010.

[21] D. Hsieh, D. Qian, L. Wray, Y. Xia, Y. S. Hor, R. Cava, and M. Z. Hasan, "A topological dirac insulator in a quantum spin hall phase," *Nature*, vol. 452, no. 7190, pp. 970–974, 2008.

[22] L. Fu, C. L. Kane, and E. J. Mele, "Topological insulators in three dimensions," *Physical review letters*, vol. 98, no. 10, p. 106803, 2007.

[23] L. Fu and C. L. Kane, "Topological insulators with inversion symmetry," *Physical Review B*, vol. 76, no. 4, p. 045302, 2007.

[24] Y. Chen, J. Analytis, J.-H. Chu, Z. Liu, S.-K. Mo, X.-L. Qi, H. Zhang, D. Lu, X. Dai, Z. Fang, *et al.*, "Experimental realization of a three-dimensional topological insulator, bi2te3," *Science*, vol. 325, no. 5937, pp. 178–181, 2009.

[25] H. Zhang, C.-X. Liu, X.-L. Qi, X. Dai, Z. Fang, and S.-C. Zhang, "Topological insulators in bi2se3, bi2te3 and sb2te3 with a single dirac cone on the surface," *Nature Physics*, vol. 5, no. 6, pp. 438–442, 2009.

[26] I. M. TSidilkovskii, *Band structure of semiconductors*. Oxford New York: Pergamon Press, 1982.

[27] L. Müchler, H. Zhang, S. Chadov, B. Yan, F. Casper, J. Kübler, S.-C. Zhang, and C. Felser, "Topological insulators from a chemists perspective," *Angewandte Chemie*, vol. 124, no. 29, pp. 7333–7337, 2012.

[28] L. Müchler, F. Casper, B. Yan, S. Chadov, and C. Felser, "Topological insulators and thermoelectric materials," *physica status solidi (RRL)-Rapid Research Letters*, 2012.

[29] W. Demtroder, *Atoms, molecules and photons : an introduction to atomic-, molecular- and quantum-physics*. Heidelberg London: Springer, 2010.

[30] M. Rivas, *Kinematical theory of spinning particles : classical and quantum mechanical formalism of elementary particles*. Dordrecht u.a: Kluwer Academic Publishers, 2001.

[31] N. Berchenko and M. Pashkovski, "Mercury telluride: a zero-gap semiconductor," *Soviet Physics Uspekhi*, vol. 19, no. 6, p. 462, 1976.

[32] R. Piotrzkowski, S. Porowski, Z. Dziuba, J. Ginter, W. Giriat, and L. Sosnowski, "Band structure of hgte," *physica status solidi (b)*, vol. 8, no. 3, pp. K135–K139, 1965.

[33] C.-X. Liu, H. Zhang, B. Yan, X.-L. Qi, T. Frauenheim, X. Dai, Z. Fang, and S.-C. Zhang, "Oscillatory crossover from two dimensional to three dimensional topological insulators," *arXiv preprint arXiv:0908.3654*, 2009.

[34] D. Rothe, R. Reinthaler, C. Liu, L. Molenkamp, S. Zhang, and E. Hankiewicz, "Fingerprint of different spin–orbit terms for spin transport in hgte quantum wells," *New Journal of Physics*, vol. 12, no. 6, p. 065012, 2010.

[35] C. Liu, T. L. Hughes, X.-L. Qi, K. Wang, and S.-C. Zhang, "Quantum spin hall effect in inverted type-ii semiconductors," *Physical review letters*, vol. 100, no. 23, p. 236601, 2008.

[36] I. Knez, R. Du, and G. Sullivan, "Finite conductivity in mesoscopic hall bars of inverted inas/gasb quantum wells," *Physical Review B*, vol. 81, no. 20, p. 201301, 2010.

[37] I. Knez, R.-R. Du, and G. Sullivan, "Evidence for helical edge modes in inverted inas/gasb quantum wells," *Physical review letters*, vol. 107, no. 13, p. 136603, 2011.

[38] J. C. Teo, L. Fu, and C. Kane, "Surface states and topological invariants in three-dimensional topological insulators: Application to bi$_{-}$ {1- x} sb$_{-}$ {x}," *Physical Review B*, vol. 78, no. 4, p. 045426, 2008.

[39] Z. Wang, X.-L. Qi, and S.-C. Zhang, "Equivalent topological invariants of topological insulators," *New Journal of Physics*, vol. 12, no. 6, p. 065007, 2010.

[40] D. Hsieh, Y. Xia, D. Qian, L. Wray, F. Meier, J. Dil, J. Osterwalder, L. Patthey, A. Fedorov, H. Lin, *et al.*, "Observation of time-reversal-protected single-dirac-cone topological-insulator states in bi$_{-}$ {2} te$_{-}$ {3} and sb$_{-}$ {2} te$_{-}$ {3}," *Physical review letters*, vol. 103, no. 14, p. 146401, 2009.

[41] D. Hsieh, L. Wray, D. Qian, Y. Xia, J. Dil, F. Meier, L. Patthey, J. Osterwalder, G. Bihlmayer, Y. Hor, *et al.*, "Direct observation of spin-polarized surface states in the parent compound of a topological insulator using spin-and angle-resolved photoemission spectroscopy in a mott-polarimetry mode," *New Journal of Physics*, vol. 12, no. 12, p. 125001, 2010.

[42] L. Fu and C. L. Kane, "Topological insulators with inversion symmetry," *Phys. Rev. B*, vol. 76, p. 045302, Jul 2007.

[43] L. Basit, C. Wang, C. A. Jenkins, B. Balke, V. Ksenofontov, G. H. Fecher, C. Felser, E. Mugnaioli, U. Kolb, S. A. Nepijko, *et al.*, "Heusler compounds as ternary intermetallic nanoparticles: Co2fega," *Journal of Physics D: Applied Physics*, vol. 42, no. 8, p. 084018, 2009.

[44] T. Graf, F. Casper, J. Winterlik, B. Balke, G. H. Fecher, and C. Felser, "Crystal structure of new heusler compounds," *Zeitschrift für anorganische und allgemeine Chemie*, vol. 635, no. 6-7, pp. 976–981, 2009.

[45] D. Xiao, Y. Yao, W. Feng, J. Wen, W. Zhu, X.-Q. Chen, G. M. Stocks, and Z. Zhang, "Half-heusler compounds as a new class of three-dimensional topological insulators," *Physical review letters*, vol. 105, no. 9, p. 096404, 2010.

[46] H. Lin, L. A. Wray, Y. Xia, S. Xu, S. Jia, R. J. Cava, A. Bansil, and M. Z. Hasan, "Half-heusler ternary compounds as new multifunctional experimental platforms for topological quantum phenomena," *Nature Materials*, vol. 9, no. 7, pp. 546–549, 2010.

[47] H.-J. Zhang, S. Chadov, L. Müchler, B. Yan, X.-L. Qi, J. Kübler, S.-C. Zhang, and C. Felser, "Topological insulators in ternary compounds with a honeycomb lattice," *Phys. Rev. Lett.*, vol. 106, p. 156402, Apr 2011.

[48] B. Yan, L. Müchler, and C. Felser, "Prediction of weak topological insulators in layered semiconductors," *Phys. Rev. Lett.*, vol. 109, p. 116406, Sep 2012.

[49] Z. Wang, Y. Sun, X.-Q. Chen, C. Franchini, G. Xu, H. Weng, X. Dai, and Z. Fang, "Dirac semimetal and topological phase transitions," *Physical Review B*, vol. 85, no. 19, p. 195320, 2012.

[50] K. Yang, W. Setyawan, S. Wang, M. B. Nardelli, and S. Curtarolo, "A search model for topological insulators with high-throughput robustness descriptors," *Nature materials*, vol. 11, no. 7, pp. 614–619, 2012.

[51] C.-X. Liu, X.-L. Qi, H. Zhang, X. Dai, Z. Fang, and S.-C. Zhang, "Model hamiltonian for topological insulators," *Physical Review B*, vol. 82, no. 4, p. 045122, 2010.

[52] S. Lee and P. von Allmen, "Tight-binding modeling of thermoelectric properties of bismuth telluride," *Applied physics letters*, vol. 88, no. 2, pp. 022107–022107, 2006.

[53] L. Fu, "Hexagonal warping effects in the surface states of the topological insulator bi_ {2} te_ {3}," *Physical review letters*, vol. 103, no. 26, p. 266801, 2009.

[54] A. Taskin and Y. Ando, "Berry phase of nonideal dirac fermions in topological insulators," *Physical Review B*, vol. 84, no. 3, p. 035301, 2011.

[55] Z. Alpichshev, J. Analytis, J.-H. Chu, I. R. Fisher, Y. Chen, Z.-X. Shen, A. Fang, and A. Kapitulnik, "Stm imaging of electronic waves on the surface of bi_ {2} te_ {3}: Topologically protected surface states and hexagonal warping effects," *Physical review letters*, vol. 104, no. 1, p. 016401, 2010.

[56] N. Cade and P. Lee, "Self consistent energy band structures for hgte and cdte," *Solid state communications*, vol. 56, no. 7, pp. 637–641, 1985.

[57] M. Franz, *Topological Insulators*. Elsevier Science, 2013.

[58] L. Molenkamp. (Private Communication).

[59] J. Maciejko, T. Hughes, and S. Zhang, "The quantum spin hall effect," *Annu. Rev. Condens. Matter Phys.*, vol. 2, no. 1, pp. 31–53, 2011.

[60] P. Sengupta, S. Lee, S. Steiger, H. Ryu, and G. Klimeck, "Multiscale modeling of a quantum dot heterostructure," in *MRS Proceedings*, vol. 1370, Cambridge Univ Press, 2011.

[61] J. Schulman and Y. Chang, "Hgte-cdte superlattice subband dispersion," *Physical Review B*, vol. 33, no. 4, p. 2594, 1986.

[62] G. Wu and T. McGill, "Strain effects in hgte-cdte superlattices grown on cdte substrates," *Applied Physics Letters*, vol. 47, no. 6, pp. 634–636, 1985.

[63] J. Lu, W. Shan, H. Lu, and S. Shen, "Non-magnetic impurities and in-gap bound states in topological insulators," *New Journal of Physics*, vol. 13, p. 103016, 2011.

[64] C. Brüne, A. Roth, H. Buhmann, E. Hankiewicz, L. Molenkamp, J. Maciejko, X. Qi, and S. Zhang, "Spin polarization of the quantum spin hall edge states," *Arxiv preprint arXiv:1107.0585*, 2011.

[65] M. König, H. Buhmann, L. Molenkamp, T. Hughes, C. Liu, X. Qi, and S. Zhang, "The quantum spin hall effect: theory and experiment," *Arxiv preprint arXiv:0801.0901*, 2008.

[66] S. Krishnamurthy, A. Chen, A. Sher, and M. Van Schilfgaarde, "Temperature dependence of band gaps in hgcdte and other semiconductors," *Journal of electronic materials*, vol. 24, no. 9, pp. 1121–1125, 1995.

[67] X. Zhang, A. Pfeuffer-Jeschke, K. Ortner, V. Hock, H. Buhmann, C. Becker, and G. Landwehr, "Rashba splitting in n-type modulation-doped hgte quantum wells with an inverted band structure," *Physical Review B*, vol. 63, no. 24, p. 245305, 2001.

[68] D. Hsieh, Y. Xia, D. Qian, L. Wray, J. Dil, F. Meier, J. Osterwalder, L. Patthey, J. Checkelsky, N. Ong, *et al.*, "A tunable topological insulator in the spin helical dirac transport regime," *Nature*, vol. 460, no. 7259, pp. 1101–1105, 2009.

[69] S. S. Hong, Y. Zhang, J. J. Cha, X.-L. Qi, and Y. Cui, "Observation of helical surface transport in topological insulator nanowire interferometer," *arXiv preprint arXiv:1303.1601*, 2013.

[70] J. G. Checkelsky, J. Ye, Y. Onose, Y. Iwasa, and Y. Tokura, "Dirac-fermion-mediated ferromagnetism in a topological insulator," *Nature Physics*, vol. 8, no. 10, pp. 729–733, 2012.

[71] Y. Wang, D. Hsieh, D. Pilon, L. Fu, D. Gardner, Y. Lee, and N. Gedik, "Observation of a warped helical spin texture in bi_ {2} se_ {3} from circular dichroism angle-resolved photoemission spectroscopy," *Physical Review Letters*, vol. 107, no. 20, p. 207602, 2011.

[72] W.-Y. Shan, H.-Z. Lu, and S.-Q. Shen, "Effective continuous model for surface states and thin films of three-dimensional topological insulators," *New Journal of Physics*, vol. 12, no. 4, p. 043048, 2010.

[73] H. Zhang, C. Liu, X. Qi, X. Dai, Z. Fang, and S. Zhang, "Topological insulators in bi2se3, bi2te3 and sb2te3 with a single dirac cone on the surface," *Nature Physics*, vol. 5, no. 6, pp. 438–442, 2009.

[74] Y. Sakamoto, T. Hirahara, H. Miyazaki, S.-i. Kimura, and S. Hasegawa, "Spectroscopic evidence of a topological quantum phase transition in ultrathin bi_ {2} se_ {3} films," *Physical Review B*, vol. 81, no. 16, p. 165432, 2010.

[75] C.-Z. Chang, K. He, M.-H. Liu, Z.-C. Zhang, X. Chen, L.-L. Wang, X.-C. Ma, Y.-Y. Wang, and Q.-K. Xue, "Growth of quantum well films of topological insulator bi2se3 on insulating substrate," *arXiv preprint arXiv:1012.5716*, 2010.

[76] Y. A. Bychkov and E. Rashba, "Properties of a 2d electron gas with lifted spectral degeneracy," *JETP lett*, vol. 39, no. 2, p. 78, 1984.

[77] F. Kuemmeth and E. I. Rashba, "Giant spin rotation under quasiparticle-photoelectron conversion: Joint effect of sublattice interference and spin-orbit coupling," *Physical Review B*, vol. 80, no. 24, p. 241409, 2009.

[78] E. d. A. e Silva, G. La Rocca, and F. Bassani, "Spin-orbit splitting of electronic states in semiconductor asymmetric quantum wells," *Physical Review B*, vol. 55, no. 24, p. 16293, 1997.

[79] P. Phillips, *Advanced Solid State Physics*. Cambridge University Press, 2012.

[80] S. S. Hong, W. Kundhikanjana, J. J. Cha, K. Lai, D. Kong, S. Meister, M. A. Kelly, Z.-X. Shen, and Y. Cui, "Ultrathin topological insulator bi2se3 nanoribbons exfoliated by atomic force microscopy," *Nano letters*, vol. 10, no. 8, pp. 3118–3122, 2010.

[81] A. M. Essin and J. Moore, "Topological insulators beyond the brillouin zone via chern parity," *Physical Review B*, vol. 76, no. 16, p. 165307, 2007.

[82] H. Kroemer, "The 6.1 a family (inas, gasb, alsb) and its heterostructures: a selective review," *Physica E: Low-dimensional Systems and Nanostructures*, vol. 20, no. 3, pp. 196–203, 2004.

[83] H. Kroemer, "Heterostructure devices: A device physicist looks at interfaces," *Surface Science*, vol. 132, no. 1-3, pp. 543–576, 1983.

[84] T. Krishnamohan, D. Kim, S. Raghunathan, and K. Saraswat, "Double-gate strained-ge heterostructure tunneling fet (tfet) with record high drive currents and 60mv/dec subthreshold slope," in *Electron Devices Meeting, 2008. IEDM 2008. IEEE International*, pp. 1–3, IEEE, 2008.

[85] K. Boucart and A. Ionescu, "A new definition of threshold voltage in tunnel fets," *Solid-State Electronics*, vol. 52, no. 9, pp. 1318–1323, 2008.

[86] M. Altarelli, "Electronic structure and semiconductor-semimetal transition in inas-gasb superlattices," *Phys. Rev. B*, vol. 28, pp. 842–845, Jul 1983.

[87] I. Lapushkin, A. Zakharova, S. Yen, and K. Chao, "A self-consistent investigation of the semimetal–semiconductor transition in inas/gasb quantum wells under external electric fields," *Journal of Physics: Condensed Matter*, vol. 16, p. 4677, 2004.

[88] T. Andlauer and P. Vogl, "Full-band envelope-function approach for type-ii broken-gap superlattices," *Physical Review B*, vol. 80, no. 3, p. 035304, 2009.

[89] G. Klimeck, R. Bowen, T. Boykin, C. Salazar-Lazaro, T. Cwik, and A. Stoica, "Si tight-binding parameters from genetic algorithm fitting," *Superlattices and Microstructures*, vol. 27, no. 2, pp. 77–88, 2000.

[90] T. Boykin, G. Klimeck, and F. Oyafuso, "Valence band effective-mass expressions in the sp^{3} d^{5} s^{*} empirical tight-binding model applied to a si and ge parametrization," *Physical Review B*, vol. 69, no. 11, p. 115201, 2004.

[91] Y.-M. Niquet. (Private Communication).

[92] T. Tritt, *Recent Trends in Thermoelectric Materials Research*. Boston: Academic Press, 2001.

[93] H. Zhang, C.-X. Liu, and S.-C. Zhang, "Spin-orbital texture in topological insulators," *arXiv preprint arXiv:1211.0762*, 2012.

[94] D. Jena, *Polarization induced electron populations in III-V nitride semiconductors: Transport, growth, and device applications*. PhD thesis, University of California, Santa Barbara, 2003.

[95] M. Suzuki and T. Uenoyama, "Theoretical study of momentum matrix elements of gan," *Japanese journal of applied physics*, vol. 35, no. part 1, pp. 543–545, 1996.

[96] Y. Yeo, T. Chong, and M. Li, "Electronic band structures and effective-mass parameters of wurtzite gan and inn," *Journal of applied physics*, vol. 83, no. 3, pp. 1429–1436, 1998.

[97] S. Chuang and C. Chang, "k p method for strained wurtzite semiconductors," *Physical Review B*, vol. 54, no. 4, p. 2491, 1996.

[98] W. Feng, W. Zhu, H. H. Weitering, G. M. Stocks, Y. Yao, and D. Xiao, "Strain tuning of topological band order in cubic semiconductors," *Physical Review B*, vol. 85, no. 19, p. 195114, 2012.

[99] D. Teweldebrhan, V. Goyal, and A. A. Balandin, "Exfoliation and characterization of bismuth telluride atomic quintuples and quasi-two-dimensional crystals," *Nano letters*, vol. 10, no. 4, pp. 1209–1218, 2010.

[100] D. Kong, J. C. Randel, H. Peng, J. J. Cha, S. Meister, K. Lai, Y. Chen, Z.-X. Shen, H. C. Manoharan, and Y. Cui, "Topological insulator nanowires and nanoribbons," *Nano letters*, vol. 10, no. 1, pp. 329–333, 2009.

[101] D.-X. Qu, Y. Hor, J. Xiong, R. Cava, and N. Ong, "Quantum oscillations and hall anomaly of surface states in the topological insulator bi2te3," *Science*, vol. 329, no. 5993, pp. 821–824, 2010.

[102] L. He, F. Xiu, X. Yu, M. Teague, W. Jiang, Y. Fan, X. Kou, M. Lang, Y. Wang, G. Huang, *et al.*, "Surface-dominated conduction in a 6 nm thick bi2se3 thin film," *Nano letters*, vol. 12, no. 3, pp. 1486–1490, 2012.

[103] H. Peng, K. Lai, D. Kong, S. Meister, Y. Chen, X.-L. Qi, S.-C. Zhang, Z.-X. Shen, and Y. Cui, "Aharonov-bohm interference in topological insulator nanoribbons," *Nature materials*, vol. 9, no. 3, pp. 225–229, 2009.

[104] Y. Zhang and A. Vishwanath, "Anomalous aharonov-bohm conductance oscillations from topological insulator surface states," *Physical review letters*, vol. 105, no. 20, p. 206601, 2010.

[105] D. Kong, W. Dang, J. J. Cha, H. Li, S. Meister, H. Peng, Z. Liu, and Y. Cui, "Few-layer nanoplates of bi2se3 and bi2te3 with highly tunable chemical potential," *Nano letters*, vol. 10, no. 6, pp. 2245–2250, 2010.

[106] H. Cao, J. Tian, I. Miotkowski, T. Shen, J. Hu, S. Qiao, and Y. P. Chen, "Quantized hall effect and shubnikov–de haas oscillations in highly doped bi_{2} se_{3}: Evidence for layered transport of bulk carriers," *Physical Review Letters*, vol. 108, no. 21, p. 216803, 2012.

[107] M.-X. Wang, C. Liu, J.-P. Xu, F. Yang, L. Miao, M.-Y. Yao, C. Gao, C. Shen, X. Ma, X. Chen, *et al.*, "The coexistence of superconductivity and topological order in the bi2se3 thin films," *Science*, vol. 336, no. 6077, pp. 52–55, 2012.

[108] D. Zhang, J. Wang, A. M. DaSilva, J. S. Lee, H. R. Gutierrez, M. H. Chan, J. Jain, and N. Samarth, "Superconducting proximity effect and possible evidence for pearl vortices in a candidate topological insulator," *Physical Review B*, vol. 84, no. 16, p. 165120, 2011.

[109] L. He, X. Kou, and K. L. Wang, "Review of 3d topological insulator thin-film growth by molecular beam epitaxy and potential applications," *physica status solidi (RRL)-Rapid Research Letters*, 2013.

[110] M. Tinkham, "Introduction to superconductivity: (dover books on physics)(vol i)," 2004.

[111] P. d. Gennes, *Superconductivity of metals and alloys*. Addison-Wesley New York, 1989.

[112] C. Kittel and C.-y. Fong, *Quantum theory of solids*, vol. 24. Wiley New York, 1963.

[113] C. W. Groth, M. Wimmer, A. R. Akhmerov, and X. Waintal, "Kwant: a software package for quantum transport," *arXiv preprint arXiv:1309.2926*, 2013.

[114] W. McMillan, "Tunneling model of the superconducting proximity effect," *Physical Review*, vol. 175, no. 2, p. 537, 1968.

[115] H. Takayanagi and T. Kawakami, "Superconducting proximity effect in the native inversion layer on inas," *Physical review letters*, vol. 54, no. 22, p. 2449, 1985.

[116] Z. Zhang, X. Feng, M. Guo, Y. Ou, J. Zhang, K. Li, L. Wang, X. Chen, Q. Xue, X. Ma, *et al.*, "Transport properties of sb2te3/bi2te3 topological insulator heterostructures," *physica status solidi (RRL)-Rapid Research Letters*, 2010.

[117] M. Veldhorst, M. Snelder, M. Hoek, T. Gang, V. Guduru, X. Wang, U. Zeitler, W. van der Wiel, A. Golubov, H. Hilgenkamp, *et al.*, "Josephson supercurrent through a topological insulator surface state," *Nature materials*, vol. 11, no. 5, pp. 417–421, 2012.

[118] S. Steiger, M. Povolotskyi, H. Park, T. Kubis, G. Klimeck, *et al.*, "Nemo5: A parallel multiscale nanoelectronics modeling tool," *Nanotechnology, IEEE Transactions on*, vol. 10, no. 6, pp. 1464–1474, 2011.

APPENDIX

A. MATLAB SCRIPT FOR EVALUATING SPIN POLARIZATION

This appendix contains the MATLAB script for evaluating spin polarization of TI surface states. Please note that this script only works with the output files produced by the NEMO5 simulator [118].

```
clear all
name = 'TI_ex1';
k= load([name,'_k_distance.dat']);
kmax = max(k);
kmin = min(k);
k = k - (kmax+kmin)/2;
e = load([name,'_energies.dat']);
s = dlmread([name,'_spin_projection.dat']);
sigma_Pauli_x = [0, 1; 1, 0];
sigma_Pauli_y = [0, -i; i, 0];
sigma_Pauli_z = [1, 0; 0, -1];
n = [1, 0, 0]; % spin quantization axis (input)
% a3 = [1 1 1]/sqrt(3);
% a2 = [1 -1 0 ]/sqrt(2);
% a1 = [1 1 -2]/sqrt(6);
% n =a1*n0(1)+a2*n0(2)+a3*n0(3);
n = n/norm(n);
sigma = n(1) * sigma_Pauli_x + n(2)*sigma_Pauli_y + n(3)*sigma_Pauli_z;
n = size(e);
n_bands = n(2);
```

```
k_points = n(1);
figure; hold on;
set(gca, 'FontSize', 16)
for band = [1:n_bands]
    s1 = s(:,(band-1)*3+1:band*3);
    spin = s1(:,1) - s1(:,3);
    for kind = [1:k_points]
        s_matrix = [s1(kind,1), s1(kind,2); s1(kind,2)', s1(kind,3)];
        sp = trace(sigma * s_matrix);
        spin(kind) = sp;
    end
    Emin = min(e(:,band));
    Emax = max(e(:,band));
    if ((Emin > -3) && (Emax<3))
        scatter(k, e(:,band),20, spin,'filled');
    end
end
xlabel('wave vector [1/nm]');
ylabel('Energy [ev]');
hcb = colorbar;
set(hcb, 'FontSize', 16);
box on;
caxis([-1,1]);
colormap cool;
xlim([min(k) max(k)]);
hl = line([min(k) max(k)],[0, 0]);
set(hl,'LineWidth', 2);
set(hl,'color', [0 0 0]);
```

VITA

VITA

Parijat Sengupta received his Bachelor's Degree in Electrical Engineering from REC,Jaipur, India. In his masters he worked in the Computational Electronics Group of Dr.Marco Saraniti and was involved in simulation of electron transport using the Monte Carlo technique. He also performed EPM based band structure calculations. Subsequently he joined the NVM division of Impinj,Inc, Seattle,WA and was last employed with the device group at Nvidia,Corp, Santa Clara, CA.He joined the Klimeck research group in August 2008